**Enabling a Screw Fastener System for Orthopedic Implants Made by
Additive Manufacturing**

by

Ralf Daniel Fischer

A thesis submitted to the Graduate Faculty of
Auburn University
in partial fulfillment of the
requirements for the Degree of
Master of Science

Auburn, Alabama
May 04, 2019

Keywords: Additive Manufacturing, Laser-Powder Bed Fusion, Orthopedic Implants

Approved by

Barton C. Prorok, Chair, Professor of Materials Engineering
Xiaoyuan Lou, Associate Professor of Materials Engineering
Dong-Joo Kim, Alumni Professor of Materials Engineering

Abstract

This research study explores the feasibility of an additively manufactured screw locking system that allows for the fixation of patient-specific orthopedic implants without applying pressure onto the bone. This is beneficial for the prevention of porosis underneath the implant. Grade 23 Titanium and 316L Stainless Steel, two commonly used biocompatible metals, are chosen as the materials for this research. A parameter study was conducted to produce high-density 3D-printed parts. Heat treatment was performed to get different microstructures and hardness. A PAX advanced locking system was reverse engineered using a high power X-Ray CT and sample specimen were produced. The strength of the system was evaluated by measuring the force needed to push the screw out of the locking plate. Annealed 316L stainless steel locking plate was found to have a high strength while the push-out force is not dependent on the build orientation.

Acknowledgments

The research presented in this study would not have been possible without the help and guidance of many individuals. For this, I would like to express my dearest gratitude to everyone who supported me during my research and preparation of my research.

First, I would like to thank my advisor, Dr. Barton Charles Prorok, for his support and guidance throughout the time I was part of his excellent research group. Thank you for always being there to help and give advice and allowing me to acquire my graduate degree at this excellent facility. Furthermore, I would like to thank Pu Deng, Dr. Sharneice Holland, Mollie Osborn, and Addison Reagan for giving advice and lending a hand whenever needed.

In addition, I would like to express special gratitude to the committee members Dr. Xiaoyuan Lou and Dr. Dong-Joo Kim for their advice and helpfulness. Thank you, Dr. Jeffrey Fergus, for bringing me to Auburn University for my Bachelor's Thesis and Mr. Steven Moore who was always there when help was needed.

Thank you to Dr. Jan Klasen, whose vision and entrepreneurial mindset was a great asset to this interesting research topic.

Lastly, I would like to express my deepest appreciation to my family and my friends. Because of you and your steady support, I had a wonderful experience abroad and Auburn became my second home.

Table of Contents

List of Tables

List of Abbreviations

3D	Three Dimensional
AM	Additive Manufacturing
ALPS	Advanced Locking Plate System
AO	*Arbeitsgemeinschaft fuer Osteosynthesenfragen* (Association of Osteosynthesis)
CAD	Computer Aided Design
CAM	Computer Aided Manufacturing
DED	Direct Energy Deposition
DCP	Dynamic Compression Plate
EB-PBF	Electron-Beam Powder Bed Fusion
EDS	Energy Dispersive Spectroscopy
e.g.	*exempli gratia* or "for the sake of example"
FC	Furnace Cooling
FDA	Food and Drug Administration
GA	Gas Atomization
HIP	High Isostatic Pressing
ICP	Inductively Coupled Plasma Mass Spectroscopy
LC-DCP	Low-Contact Dynamic Compression Plate
LCP	Locking Compression Plate
LoF	Lack of Fusion
L-PBF	Laser Powder Bed Fusion
NIST	National Institute for Standards and Technology

OM	Optical Microscopy
PAX	Polyaxial Advanced Locking System
PC-Fix	Point Contact Fixator
PREP	Plasma Rotating Electrode Process
PSD	Powder Size Distribution
RA	Rotary Atomization
RP	Rapid Prototyping
SEM	Scanning Electron Microscope
SRμT	Synchrotron Radiation micro-Tomography
XCT	X-Ray Computed Tomography
XRD	X-Ray Diffractometer

Chapter 1:   Introduction

Additive Manufacturing (AM) has grown within the last 30 years from a rapid prototyping technology purely used for the creation of non-structural parts to one of the key technologies of the 21st century [1]. Unlike conventional manufacturing processes that are based on subtractive manufacturing technologies (e.g. milling, grinding, cutting), additive manufacturing (AM) can clearly be distinguished by its nature of adding material to a workpiece. Initially, a three-dimensional (3D) solid model is created using a 3D-scan or CAD program. The digital file is then sliced into hundreds or thousands of layers depending on the resolution. The AM machine then creates a solid part in a layer by layer fashion. The result is a near net shape primitive of the 3D solid model [2-5].

Conventional manufacturing methods are limited in freedom of design by requirements of diverse tooling, fixtures or just unreachability caused by collisions of the tool e.g. deep holes, internal features. Furthermore, for other manufacturing processes like casting or forming subtractive manufacturing imposes additional constraints for patterns and tools. Due to the nature of "growing" a part, design constraints can be freed up early on in the manufacturing process. Designers can precisely place material to achieve the desired functionality. Combined with the digitalization of production, AM allows for topologically optimized parts that reduce the mass of a part as well as material use [1, 2].

Since AM is a generative production process, there is little to no additional fabrication time, tooling, fixturing or improved operator expertise needed. In contrast cost per part can directly be related to geometric complexity for traditional manufacturing methods, as those need specialized

1

tools, refixturing and an experienced CAM user [2, 6]. Furthermore, a personalized, low-volume production can be profitable, especially for high-end products in aerospace, automotive and biomedical. [2]

While tolerances and resolution were not much of concern in AMs early rapid prototyping (RP) phase, the current expectations are set much higher to allow the fabrication of functional parts. Specific and general tolerances are declared by the machine manufacturer with the necessary International Standard Organizations (ISO and US standards for quality assurance. Dimensional accuracy is the deviation of a finished model to its digital file. The first efforts by the National Institute of Standards and Technology (NIST) have shown, that AM enables the manufacturing of parts with a dimensional accuracy higher than a few millimeters [2, 7, 8].

AM enables a reduction in the number of parts for complete assemblies down to "single-part assemblies". Particularly in assemblies featuring integrated mechanisms, an assembly of multiple parts is necessary for the conventional manufacturing process. AM technologies not only reduce the number of parts but also cuts down on assembly time [2].

AM is perfectly feasible for lower volume parts, even though the production speed is slower. Conventional manufacturing methods like injection molding are already very quick and with a high enough throughput cost effective. However, their start-up costs are high and the time-to-part are fairly long. Furthermore, AM can reduce expenses for inventory and delivery by utilizing on-demand and on-location part production. AM also uses less material when compared to the conventional process, thus reducing the overall cost of the part. AM is actually very economical with the combined benefits of improved design and reduced efforts in the supply chain and delivery which can outweigh the disadvantages in terms of slower production speed and higher machine

cost. A summary of benefits for AM and conventional manufacturing has also been reported in Table 1 [2, 5, 9, 10].

Table 1: Factors in favor of AM vs. conventional production [5]

Favor AM	Favor conventional manufacturing
Low production volumes	Large production volumes
High material cost	Low material costs
High machining cost	Easily processes/machined materials
Capital investment	Centralized manufacturing
Logistics costs	
Transportation costs	
Prototyping	

Figure 1 clearly shows that the cost of a conventionally manufactured product increases as lot size and complexity decrease. However, in AM this relation is not applicable. As more parts are printed, the price stays the same hence the production cost/time is heavily reliant on the build-up volume. Additionally, adding a layer of complexity may decrease the cost even further due to topological optimization or the use of lattice structures. In order for AM to become a disruptive technology, it must decrease manufacturing cost by either innovative product optimization or novel business concept, as seen in. [3]
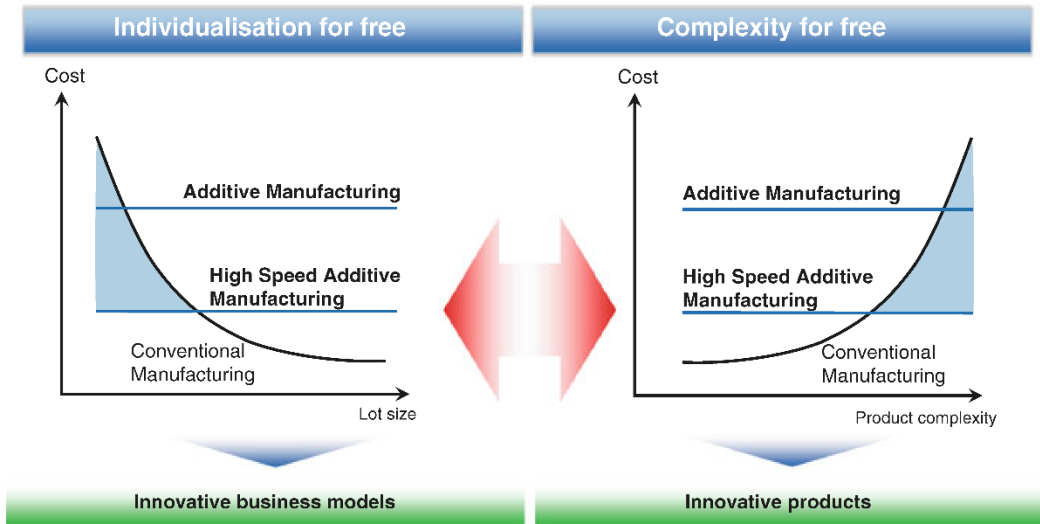
Figure 1: Drive towards innovative business models and innovative products [3].

1.1 Additive Manufacturing Technologies

Metal AM processes fuse feedstock materials like powder or wire to a dense metal part. The energy source for the melting of the material can be a laser, an electron beam or an electric arc. Table 2 shows the individual characteristics of AM technologies and compares them to each other. ASTM Standard F2792 [11] differentiates between powder bed fusion (PBF), binder jetting and direct energy deposition (DED) technologies. Further differentiation can be done by including the energy source, i.e. laser (L), electron beam (EB), or plasma arc. Although this document focusses on L-PBF, other technologies are briefly described in this chapter.

Table 2: Comparison of different AM technologies to each other [1].

Process Feedstock	DED Powder	Wire		PBF Powder	
Heat source	Laser	E-beam	Electric arc	Laser	E-beam
Nomenclature	DED-L	DED-EB	DED-PA/DED-GMA	PBF-L	PBF-EB
Power [W]	100- 300	500- 2000	1000- 3000	50- 1000	
Speed [mm/s]	5- 20	1- 10	5- 15	10- 1000	
Max. feed rate [g/s]	0.1- 1.0	0.1- 2.0	0.2- 2.8	-	
Max. build size [mm^3]	2000 x 1500 x 750	200 x 1500 x 750	5000 x 3000 x 1000	500 x 280 x 320	
Production time	High	Medium	Low	High	
Dimensional accuracy [mm]	0.5– 1.0	1.0- 1.5	Intricate features are not possible	0.04- 0.2	
Surface roughness [µm]	4– 10	8- 15	Needs Machining	7- 20	
Post processing	HP and surface grinding are seldom required	Surface grinding and machining is required to achieve better finish	Machining is essential for final part	HIP is rarely required to reduce porosity	

1.1.1 Laser Powder Bed Fusion

A schematic of one of the most popular AM technologies, L-PBF is shown in Figure 2 (a). First, a surface or solid CAD model is oriented in the build volume. Support structures are added for heat absorption and fixation of the part to the build plate. A software slices the part into planar layers and defines the scan path of the laser. The scan path is defined by a pre-specified set or parameters that are unique to the material and machine in use. Lastly, the part is formed by spreading a thin layer of powder (the layer thickness is equal to the slice settings used before) and then selectively melting parts of the powder bed. The laser beam is directed with two galvanometric driven mirrors in the X- and Y-direction. To account for the focus offset when the laser is moved from one side of the planar powder bed to the other, either an F-Theta lens for small systems or a dynamic

focusing unit is used. After every layer exposure, the powder bed is incrementally lowered in the Z-direction and a new powder layer is applied. The whole process takes place inside an inert chamber [12]. L-PBF offers very high-resolution parts with good surface finish due to its small size of powder particles and small focal spot. However, the process is slow and limited in size. Because of the high cooling rates of the material, post heat treatment is usually necessary to release residual stress [13, 14].

1.1.2 Electron Beam Powder Bed Fusion

EB-PBF works similar to L-PBF with the difference of utilizing an electron beam as a heat source inside a vacuum chamber. The electron beam is rastered and focused across the powder bed using two electromagnetic coils. Commonly, the layer is exposed to the electron beam in two steps. The first exposure lightly sinters the particles together. This prevents electrostatic charging and repulsion. In the second step, the particles are fused together. The powder bed is commonly kept at a higher temperature compared to L-PBF, which leads to lower cooling rates. This and the faster scanning speed of the electron beam allow for quicker build time. However, this process is limited to electrically conductive materials and larger feedstock powder and thicker layers result in a rougher surface finish [14, 15].

1.1.3 Direct Energy Deposition

Direct Energy Deposition (DED) utilizes a variety of heat sources. For L-DED as shown in Figure 2 (b), a nozzle sprays a feedstock material/inert gas mixture into the laser beam. The energy of the laser melts the feedstock powder. The shielding gas then carries the melt to the build plate or substrate part, where it cools off until solid under inert conditions to protect it from oxidation. EB-DED displayed in Figure 2 (c) feeds a feedstock wire into an electron beam. The wire is melted and deposited onto the build plate/substrate. EB-DED requires a large vacuum chamber for a high

purity-processing environment, as ambient conditions would not allow for a generation of an electron beam. Another DED-process illustrated in Figure 2 (d) uses an electric arc as a heat source. This process is comparable to conventional fusion welding processes with a power source and a wire feeding system. All of these DED setups are installed on a multi-axis controller. The controller is used to move the setup relative to the build plate or substrate and maintain a constant distance to the focus spot. An overhanging feature may require supporting structures to prevent overheating or distortions. Processing conditions are either preset or can be adjusted during the process by utilizing appropriate sensors. DED methods have a very high deposition rate and are typically used for big parts >10 kg. However, they require post-processing as their surface finish is rough, only close to net shape, and support structures need to be removed [1, 2].

1.1.4 Binder Jet Fusion

Binder Jet Fusion, shown in Figure 2 (e), is still nascent and has not found many commercial applications yet. Its fast and high accuracy are major benefits of this technology, which may lead to a shift in the industry towards this technology. Essentially, Binder Jet Fusion is a sintering process. Layers of feedstock powder are deposited on a substrate. An inkjet printing head deposits a liquid binder on the metal powder for each layer. The completed part is then heated in an oven to cure the binder. Subsequently, the metal part is sintered and/or high isostatic pressurized (HIP) at a higher temperature to achieve full density. During the final steps, the specimen loses some of its volume, which needs to be adjusted for in advance [2, 14, 16].

7
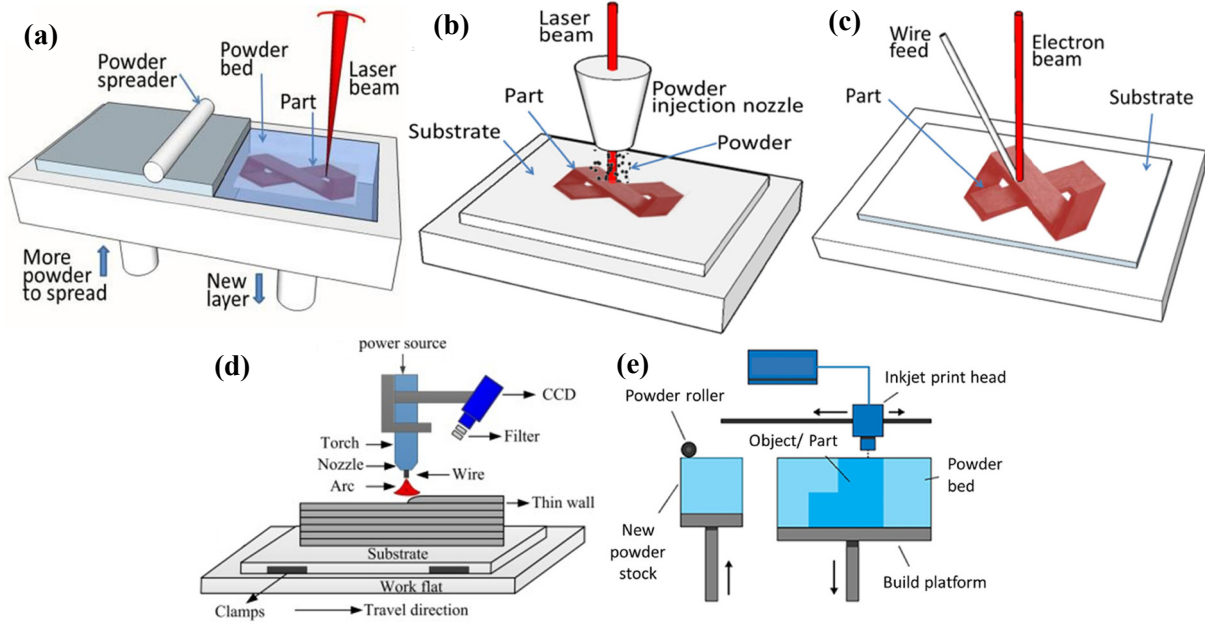
Figure 2: Schematic of different AM technologies (a) L-PBF (b) L-DED (c) EB-DED (d) Electric-Arc DED and (e) Binder Jet Fusion [1].

1.2   Challenges in L-PBF

AM is a fairly new technology and has not been qualified for many critical applications. One main issue is the assurance of good part quality. This, however, can be influenced by many factors, as the process is susceptible to external influence due to its nature of building up parts in a layer by layer fashion [1]. This chapter will name and analyze some of the most common challenges, one has to account for when considering AM for the production of parts.

1.2.1   Process Parameters

The influence of process parameters on the mechanical properties is still under investigation and has not been clearly understood yet because of the vast number of influencing factors. Figure 3 summarizes, how input parameters and underlying physics of the metal AM process affect the outcome of a print job. It can be seen, that a change in one of the parameters can influence multiple other parameters as well as outcomes [17].

8

Processing Map for Metal Additive Manufacturing
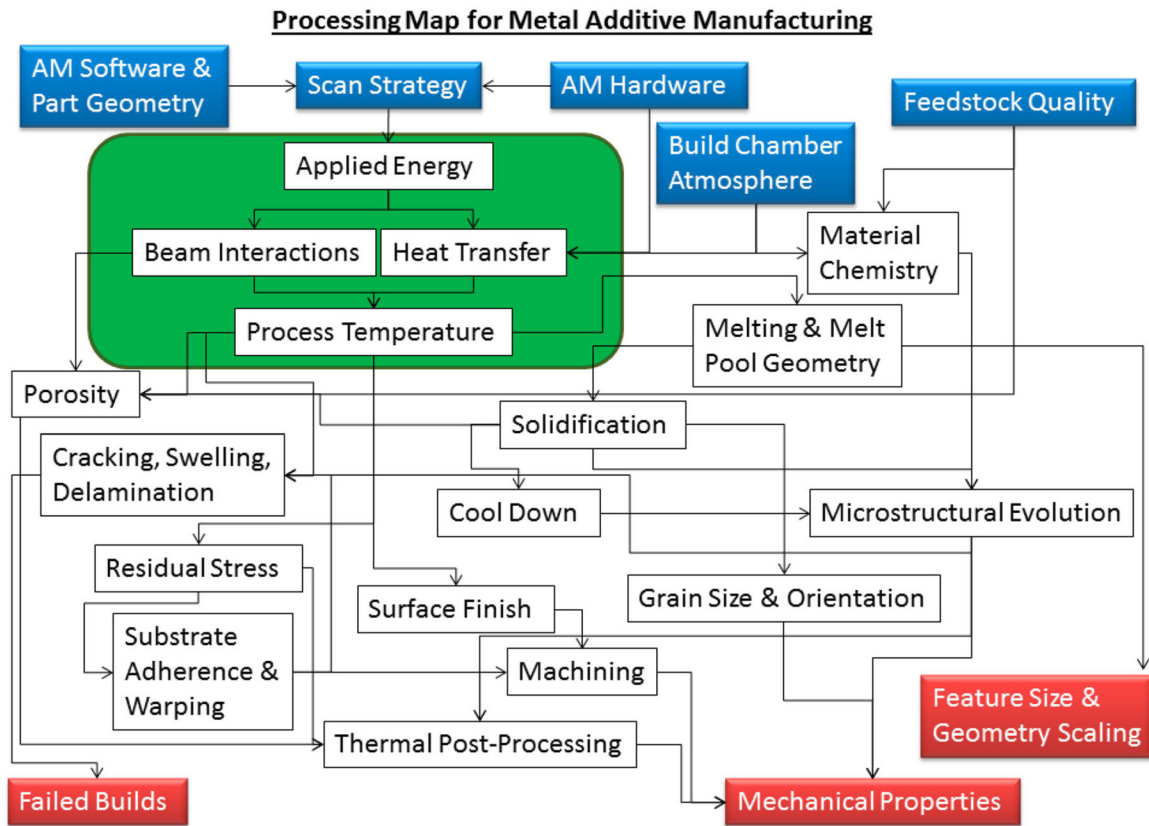
Figure 3: Outline of the relations between input parameters and underlying physics on the outcome of metal AM part [17].

The main input variables for L-PBF are layer thickness, laser power, scan velocity and hatching distance, which is the distance between the single laser scans paths. These process variables can easily be changed and mainly define the size and shape of the melt pool. An example is shown in Figure 4, where an increase in scan speed causes the melt pool to change its shape from almost spherical to heavily elongated. Not only has this, but the increase in scan speed also generates heavy undercooling, which in turn creates a discrepancy in the grain growth direction from normal to the curved surface of the liquidus isotherm. The microstructure undergoes further changes when exposed to successive layer as they are able to reheat and partially melt underlying deposition layers. This may lead to grain growth, aging thermal deformation or increased residual stress. Furthermore varies depending on the location due to different amounts of thermal cycles a

temperature increase during the build job which decreases the temperature gradient during solidification.[1, 17]
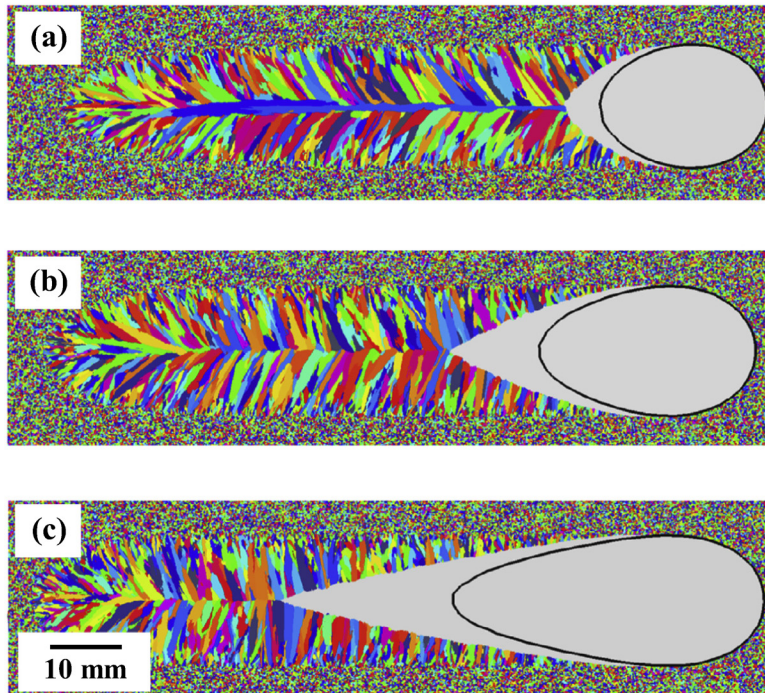
Figure 4: Dependency of the grain structure on different undercooling rates caused by different scan speeds. (a) 1 mm/s; (b) 2 mm/s; (c) 5 mm/s [1].

The printability of material is mostly studied in trial and error experiments. As one parameter can have multiple effects on the material deposition the complexity between these relationships must be reduced. All but a few parameters are kept constant while the rest are changed. This allows for the acquisition of a parameter window, in which material can successfully be deposited. Based on the experience and knowledge gained during these experiments research can be tailored to narrow down on a suitable parameter space. This decreases the number of necessary experiments and reduces the high cost and time demand which hinders this approach from wide adoption [1].

For an evaluation of process parameters the energy input E_v [J/mm^3] is often used [18-20]:

$$E_v = \frac{P_L}{v_s * h * d}$$

10

where P_L is the Laser Power, v_s is the scanning velocity, h is the hatching distance and d is the layer thickness. Unfortunately, it is not always possible to calculate E_v because some of the parameters needed are not reported [21].

1.2.2   Feedstock powder

The quality of an AM part is highly dependent on the feedstock material. Figure 5 (f) and (g) illustrates parts manufactured with powders of different quality but the same processing parameters. The powder for L-PBF usually comes pre-alloyed due to ease of feeding and controlled melting. However, because of their high surface area and tendency towards oxidization, it is critical to understand the challenges that come with it. The quality of a powder can be characterized by the shape, Powder Size Distribution (PSD), composition, morphology, and flowability [14]. The surface morphology and shape can be examined with X-ray Computed Tomography (XCT) and Scanning Electron Microscopy (SEM). The PSD can be determined using Laser Diffraction or a sieving method. A Hall flow meter can measure the flowability of the powder. Typical sizes for L-PBF feedstock material is between 10 µm and 60 µm. The preferred powder is also uniform in size distribution, spherical and has smooth surfaces, as this benefits a homogeneous melting, good interlayer bonding, superior mechanical properties, and excellent structure and surface finish [14]. The quality of the powder is directly dependent on the manufacturing process. There are four main manufacturing processes for the production of metal powder. Gas atomization (GA) is the process of atomizing a molten alloy with the help of a high-pressure flow of argon or nitrogen. GA powder is mostly spherical as seen in Figure 5 (c) and (d).

However, there are issues with dimpled surface textures and agglomeration of satellites. Furthermore, it has been reported that GA powder often includes entrapped gas bubbles, which can lead to porosity in the part. [22] Powder created by rotary atomization (RA) is created by pouring

the molten alloy onto a rotating disk. The centrifugal force flings the material off the disk. Those fine droplets then solidify as shown in Figure 5 (b). The resulting powder has a smooth surface but varies in shape. In the plasma rotating electrode process (PREP) an electric or plasma arc is used to melt the tip of a metal bar. The metal bar is then spun around its longitudinal axis, resulting in the ejection of fine droplets from the tip, which can be collected as a metal powder. PREP powders have a perfectly spherically shape with a smooth surface and have the most uniform size distribution. PREP is a very expensive process with little yield. Water atomization (WA) uses a high-pressure water jet to atomize and solidify molten metal droplets. WA powders have a rough shape and coarse surface structure. This makes it hard to spread them evenly across the powder bed. As a result, the layers tend to be thinner compared to powders from other processes [4, 14].
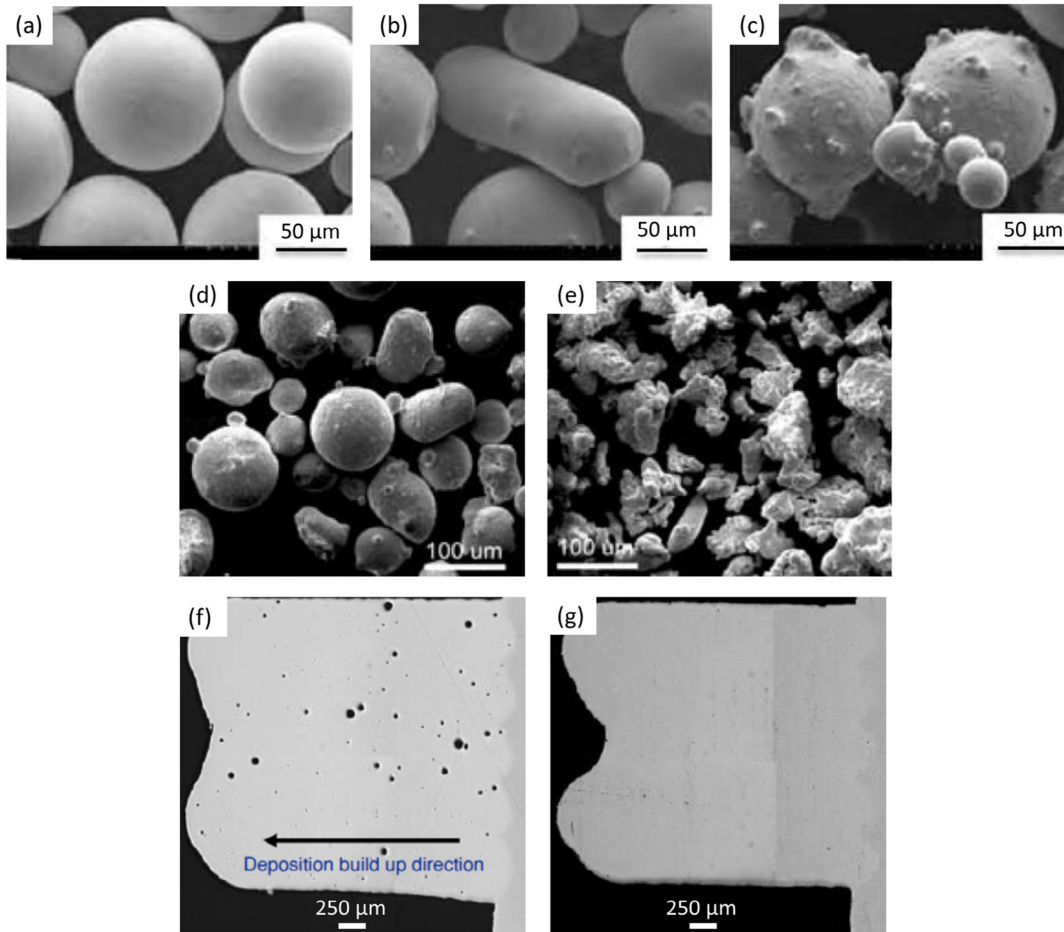
Figure 5: SEM image showing alloyed materials prepared by different manufacturing methods: (a) PREP;(b) RA; (c) and (d) GA; and (e) WA. AM part fabricated using (f) GA and (g) PREP powder [1].

1.2.3 Defects

AM is prone to the establishment of defects in the materials due to its nature of fusing only a small amount of material at a time. Defects can depreciate the mechanical properties of a part significantly. For AM, several different types of defects are known to be present recurrently. While some of these can be avoided easily, it's harder to avoid others.

Melt pool temperatures during AM can become very high, thus leading to vaporization of low alloying elements with a low vapor pressure [23]. This changes the overall composition and can

lead to a deviation in corrosion resistance, solidification microstructure and mechanical properties, which makes the production of critical high-quality components inapplicable. In-situ measurements are almost impossible because of high scanning speeds and complexity of the equipment. Thus, methods that capture the composition and/or mass of the metal powder and final part are most commonly used. Due to the microstructural inhomogeneity of AM parts, non-destructive methods, e.g. energy dispersive spectroscopy (EDS) or electron probe microanalysis, rely on sufficient statistical background. Destructive methods like inductively coupled plasma (ICP) mass spectroscopy, on the other hand, can give very accurate readings of the composition [1].

Lack of fusion (LoF) and porosity are known defects in AM [24]. There are three major mechanisms [1] that pores originate from: (1) entrapped gas, (2) keyhole effect [25], and (3) insufficient layer bonding [26]. The first reason for pores in L-PBF is the occurrence of entrapped gas (1) inside the feedstock material. Figure 5 (f) and (g) show, how a powder produced by a process more susceptible to entrapped gas leads to more gas pores inside the manufactured material [27]. Furthermore, during the melting process, the material can also trap material vapor from the melt pool or shielding gas [1]. High laser-light intensities can evaporate enough material in the melt pool. The vapor pressure excerpts a force on the molten material thus creating a deep vapor cavity as seen in Figure 6 (a) and (d). This cavity is called a keyhole (2) and acts like a light-trap. The light inside the keyhole is further absorbed in high rates due to multiple reflections and plasma-enhanced coupling [28]. When these keyholes become unstable, they can collapse and leave voids with entrapped vapor in the material. The voids are commonly spherical in shape [25]. While the previously mentioned pores usually appear at micro-scale, LoF-pores (3) as seen in Figure 6 (b) are much bigger and reach into the macro-scale with typical sizes of >10 μm. Furthermore, LoF

pores are elongated in shape with sharp edges that act as stress concentrators under load. The defects originate from not enough penetration into the underlying layer. Thus, the process is more comparable to the conduction-limited laser welding with a shallow, but wide melt pool as seen in Figure 6 (c). To transport the heat inside the melt-pool, this mechanism relies on heat conduction and convection. To reduce the appearance of LoF defects, the melt pool depth should be increased by either decreasing the scan speed or increasing the laser power [23]. There are multiple techniques for the detection of pores available. Archimedes method is an easy to use non-destructive method to determine the porosity of a sample. However, it only gives information about the overall porosity by comparing the density of the specimen with a reference. Details about the size, distribution, or shape of the pores cannot be revealed with this method. Optical Microscopy (OM) is a widely used, inexpensive tool for porosity detection. However, it is a destructive testing technique, small pores <10 μm cannot be detected accurately, and it only reveals information of the 2D plane rather than the 3D volume of the pores. On the other hand, utilizing an SEM can increase the detectable range for pores, and XCT has already been used to determine pores as small as 10 μm. For in-situ formation of pores, a Synchrotron Radiation micro-Tomography (SRμT) can be utilized. Even though SEM, XCT, and SRμT give very good results, they are very expensive due to their initial cost. HIP is a post-treatment of the parts, which can close internal pores, but it is expensive and cannot close surface defects. Producing parts with minimal defects is desirable [1].
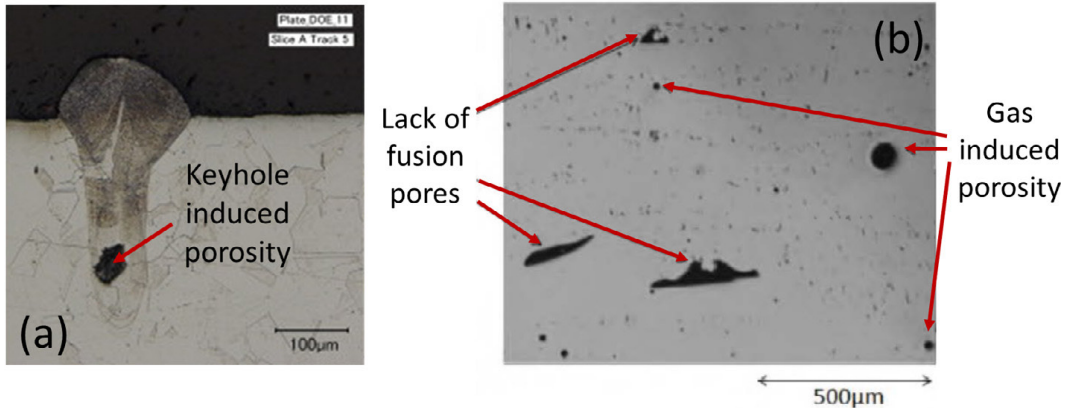
Figure 6: (a) Generation of keyhole pore due to the keyhole effect [25]; (b) cross-section of a specimen showing LoF and gas induced pores [1]; (c) conduction limited laser welding [28]; (d) keyhole laser welding [28].

High-performance AM components often require exceptional surface roughness of <1 µm [29], but AM processes cannot achieve these qualifications yet. A common solution to this problem is post-processing like HIP, shot peening, machining, grinding, or chemical polishing to acquire the desired surface roughness. However, these processes are time and cost intensive, and thus methods to improve the surface finish of as-fabricated AM parts are under investigation. [1].

1.3   Materials used in AM

The choice of the right material for a specific application is important. Whether a material can be processed in L-PBF or not is dependent on its printability. Printability is the capability of feedstock

materials to be deposited on a substrate successfully while meeting or exceeding the metallurgical, mechanical or functional requirements for a specific application. Because of many different influence factors like the melting and solidification process, limited availability of well tested numerical models, reliable thermo-mechanical material properties over a wide temperature range, and computational cost of modeling the AM process with satisfactory spatial and temporal resolution, qualifying a material based on modeling alone are rather challenging [1]. This chapter displays current findings for 316L stainless steel and titanium grade 5/23, which are two materials that have been widely adopted by AM and are under high interest for medical applications due to their good biocompatibility [30].

1.3.1   Stainless Steel

One of the most common AM feedstock materials is 304L and 316L stainless steel. Both are low cost and highly available, however only 316L is biocompatible, making it a perfect candidate for the medical industry [30]. The chemical composition of 316L is illustrated in Table 3. This conventional material is readily weldable if the compositions are controlled, prequalifying it for AM. Conventionally processes 316L stainless steel is generally fully austenitic as seen in the phase diagram in Figure 7. When processed with AM the stainless steel consists of δ-ferrite and λ-austenite due to its rapid cooling. Even though 316L undergoes a phase transformation from bcc to fcc, a strengthening effect of the material other than cold work is little. Conversely, AM 316L exhibits higher yield strength, ultimate tensile strength, and hardness as well as lower ductility as its conventional counterpart [31]. The cause for this strengthening increase and elongation decrease is the rapid solidification, which leads to a refined microstructure, dendritic and cellular growth, and higher dislocation densities with dislocation pileups at the finer grain boundaries[1]. Internal

defects such as LoF also contribute to the lower elongation rate as well as earlier failure due to fracture [32].

Table 3: Chemical composition in wt% of 316L according to AISI 316L [33].

Fe	C	Cr	Mn	Mo	Ni	P	S	Si
Bal.	0.030 max.	16.00-18.00	2.00 max.	2.00-3.00	10.00-14.00	0.045 max.	0.030 max.	1.00 max
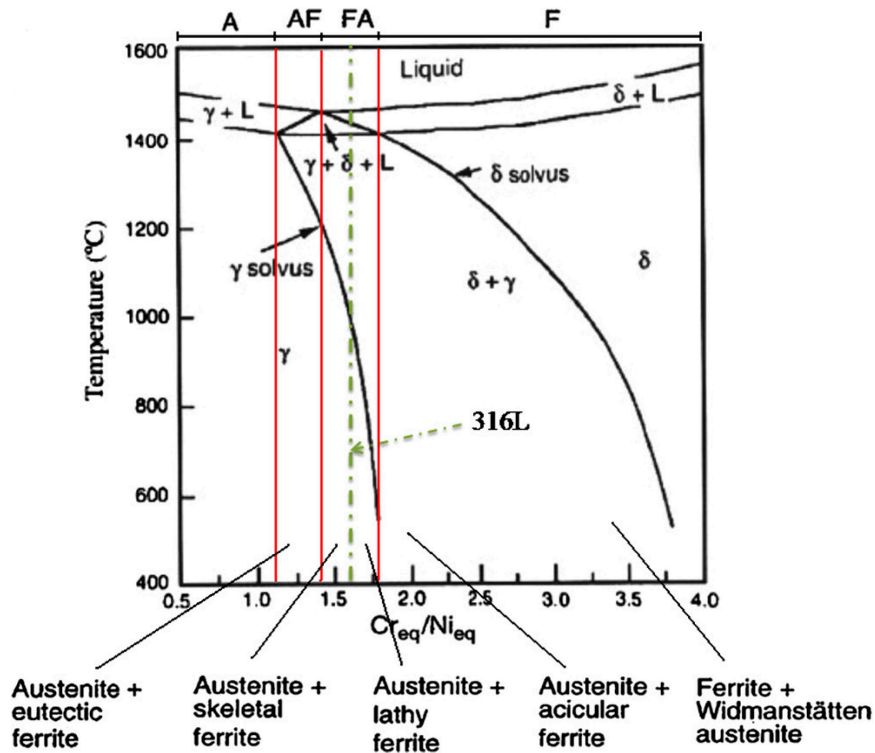
Figure 7: Pseudo-binary phase diagram of 316L Stainless Steel [34].

1.3.2   Titanium

Titanium and its alloys are high-performance materials with an exceptional strength-to-weight ratio, corrosion resistance, and biocompatibility. Studies [35] have shown that titanium implants have a much lower risk for infections than stainless steel implants. Titanium implants need 10 times of bacteria to cause a 50 % infection rate [35]. This makes them the go-to material for aerospace and medical applications [1].

The two crystal phases in titanium are called alpha titanium and beta titanium. While alpha titanium has a close-packed hexagonal structure occurs in the lower temperature range up to the β-transus temperature of 885 °C, beta titanium with a bcc phase is present past the β-transus temperature until the melting point. Alloying titanium with alpha stabilizing elements such as aluminum, carbon, nitrogen or oxygen will raise the β-transus temperature because of their higher solubility in the hcp-crystal structure. On the other hand, beta stabilizing elements can be classified into two different types. Manganese, iron, nickel, chromium, copper or silicon create a β-eutectoid type system. These elements are preferably soluble in the β-phase thus lowering the β-transus temperature. However, upon cooling the materials decompose into an α-solid solution and an intermetallic compound rich in the alloying element. The second group of beta stabilizing elements consists of molybdenum, tantalum, vanadium, and columbium. When titanium alloyed with these elements, it creates a beta isomorphous type system because of the high tendency towards dissolving in the β-phase. Thus α/ (α-β) and β/ (α-β) boundaries are pushed towards lower temperatures with an increase in β-concentration. For complete retention of metastable beta on quenching from the β-phase, a minimum amount of β-stabilizing elements is needed [36].

The titanium alloy most widely used in AM is Ti6Al4V because of its high strength-to-weight ratio, low Young's modulus, good biocompatibility in a physiological environment and high corrosion resistance [37]. Ti6Al4V belongs to the group of α-β alloys because it contains α- and β-stabilizing elements as seen in Table 4 that retain both alpha as well as beta phases upon cooling to room temperature. Depending on the solution temperature Ti6Al4V is thermally treated at, the phase relations between α and β can be engineered to inherit specific properties. Figure 8 shows the schematic vertical section of the ternary phase diagram of Ti6Al4V. Typical annealing temperatures are displayed as Point A and range from 650 °C to 750 °C. The resulting

microstructure is mainly α-phase due to the high concentration of α-stabilizing aluminum and the high solubility of vanadium in α. Beta is retained in the grain boundaries. When the solution annealing temperature is increased to point B and C and the specimen is water quenched, more β-phase in the structure and a change in the alloy content of the β-phase with increasing temperature lead to a strengthening effect during subsequent aging. Solution annealing in the β-phase shown as Point D gives the strongest response to heat treatment. However, this response usually comes with a loss in ductility and is therefore usually carried out [36].

Table 4: Chemical composition in wt% of Ti6Al4V Grade 5 and 23 according to ASTM B 265 and AMS 4996 [38].

Name	Ti	Al	C	Fe	H	N	O	V	OT
Grade 5	Bal.	5.5- 6.75	0.1	0.4	0.015	0.05	0.2	3.5- 4.5	0.4 max
Grade 23 (ELI)	Bal.	5.5- 6.75	0.1 max.	0.3 max.	0.0125 max.	0.04 max.	0.13- 0.18	3.5- 4.5	0.2 max.

Another effect on the transformation rate during cooling is the cooling rate as seen on the CCT diagram in Figure 9. While in conventional processes the β-phase has enough time to rearrange to an α phase due to moderate cooling rates, the high cooling rates observed in AM lead to the creation of the acicular α' martensite. The α' phase is usually unwanted due to its high yield strength but low ductility. Heat treatment is commonly utilized to convert the α' martensite into α phase to reach improved mechanical properties [20]. Furthermore, the α' martensite can also decompose to the α phase during the progressive thermal cycles due to the deposition of succeeding layers in AM. Wrapping up, small changes in the cooling rate can have a significant effect on the mechanical properties of Ti6Al4V [1].
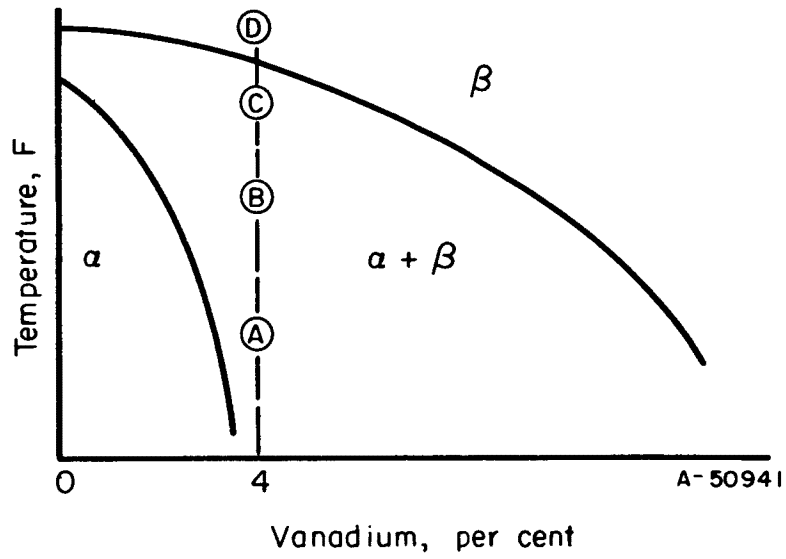
Figure 8: Phase relationships for Ti6Al4V [36].
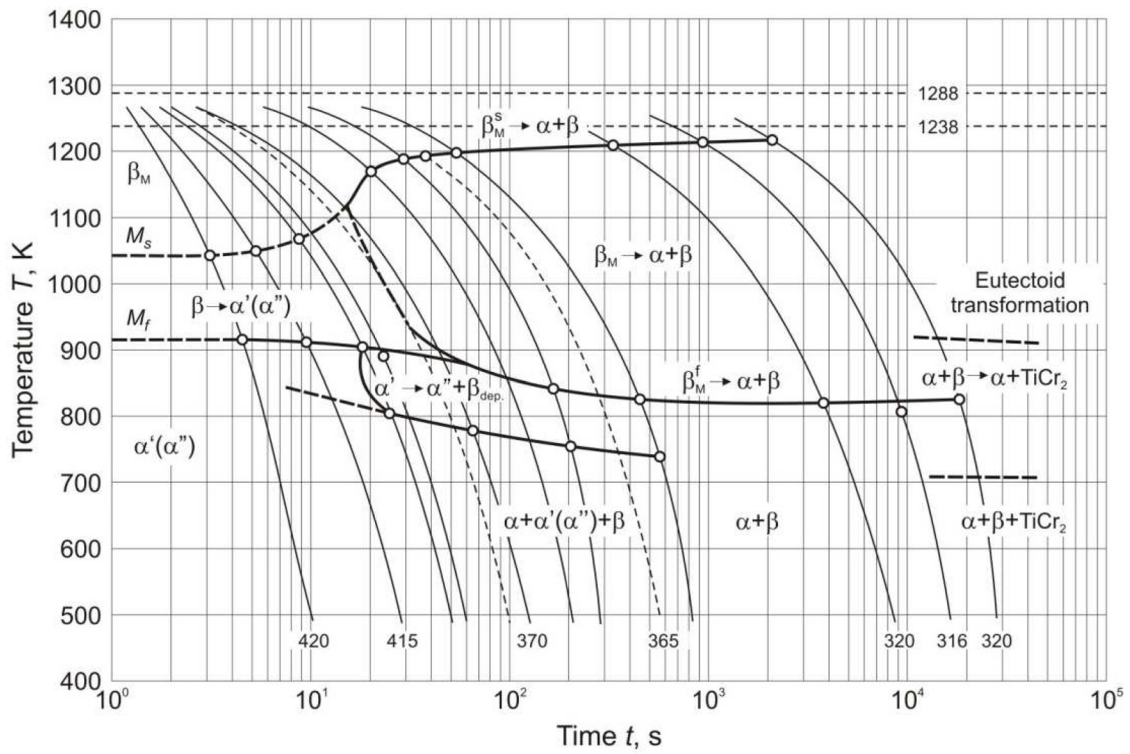
Figure 9: CCT diagram for Ti6Al4V [39].

1.4 AM in Veterinary Medicine

For medical applications, the advancement of AM techniques and materials is especially interesting for orthopedic implants. Key benefits are the relaxation of design constraints of conventional manufacturing methods, allowing for complex and conventionally impossible orthopedic implants, a decrease in manufacturing time, which allows for time-critical surgeries, and significantly lower manufacturing costs for customization [30]. However, the question about what fixation system to use remains and is still under investigation, since some fixations bring benefits in terms of tissue healing or infection rate [40]. This chapter will provide an insight into the possibilities, AM offers for the veterinary medicine and different fixation systems, their benefits as well as drawbacks.

1.4.1 Orthopedic Implants

AM is changing the implant industry by going from standard off the shelf implants to the manufacture of patient-specific implants. The complete development of patient-specific implants can be achieved by utilizing CAD software and comprises of image acquisition, i.e. by using an XCT, its elaboration, design of the implant and manufacture. AM enables the implant to be manufactured quickly, reliably and cost-effective [41] and thus has already found applications in clinical trials with explicit authorization by the patient [13, 42]. One such case is the restoration of an extensive zygomatic defect performed by Rotaru et al. [43]. The digitally designed implant has the correct geometry to fill the defect without having to adjust the implant during surgery. Furthermore, the patient-specific implant improved the final cosmetic and functional results, and there were no complications with the implant after a year [43].

Next to its benefits in turnaround time and customization, AM also allows for the implementation of complex geometries. One such geometry is lattice structures which have low stiffness and low weight while providing high strength. Furthermore, AM allows the creation of graded lattice

structures to locally adjust the mechanical properties. The implants can be tailored to have a high strength core to sustain high loads while having a low high porosity lattice on the surface to help bone ingrowth, osseointegration, or transport of nutrients, antibiotics and waste [13, 30]. Harryson et al. [44] reported a study on the reduction of stress shielding using different design configurations of a hip stem, one with a lattice mesh, one with hole configuration and one as a solid. The hip stems exhibit different bending stiffnesses while maintaining the same mechanical strength. A more even stress distribution in the lattice structured hip stem was found to reduce bone remodeling and exhibited the least amount of stress shielding [44].

Even though the future of AM for biomedical applications is promising, there are some challenges involved with introducing new technology into critical applications. New biomedical products require approval from the Food and Drug Administration (FDA). The FDA classifies devices based on the risks to the health of a patient and the level of control necessary to ensure safety and effectiveness [45]. This is why the majority of current research in the biomedical field is focused on Class I devices, which require less effort for approval [13]. However, case studies [46] have been published for Class II devices as well. In these Cases, justifications for approval can be made through the FDA CDRH's Premarket Notification (510 (k)) Program. This program evaluates the safety and effectiveness of a device by comparing it to legally marketed devices. If the legally marketed device is substantially equivalent to the devices intended use, the FDA can provide clearance for the individual device for a specific use, not to the material itself. However, new materials can only be cleared if they do not raise new concerns about their safety and effectiveness and the submission demonstrates that the new material is either safer or more effective than the legally marketed [45].

Current mounting systems for AM implants use compression based screws, i.e. the lag-screw principle as seen in [43]. However, it has been shown that conventional compression plates are not the optimal choice in order to preserve existing healthy bone as described in Chapter 1.4.2. Thus, implementing a better fixation system for quicker and more complete bone restoration can benefit the patient [40]. These mounting systems are subject of this paper and will be discussed in the following chapters.

1.4.2   Evolution of Locking Plates

Dynamic compression plates (DCP) as seen in Figure 11 (bottom) were introduced by the *Arbeitsgemeinschaft fuer Osteosynthesenfragen* (Association of Osteosynthesis, AO) in 1969. Since its introduction, it has become the most iconic plate and is still used today. However, extensive research in this area identified some shortcomings of the DCP. Within a few weeks after implantation, extensive zones of bone porosis can develop [47]. Healthy bone is able to replace the porotic bone, however, this process can take a long time during which a refracture of long bones after implant removal can occur. Commonly it is assumed that porosis appears due to stress protection caused by the implant due to increased stiffness. Using plastic instead of stainless steel causes a similar pattern of bone resorption and remodeling. This suggests that the porotic bone is caused by surgical and vascular trauma caused by the implant rather than stress shielding [40].
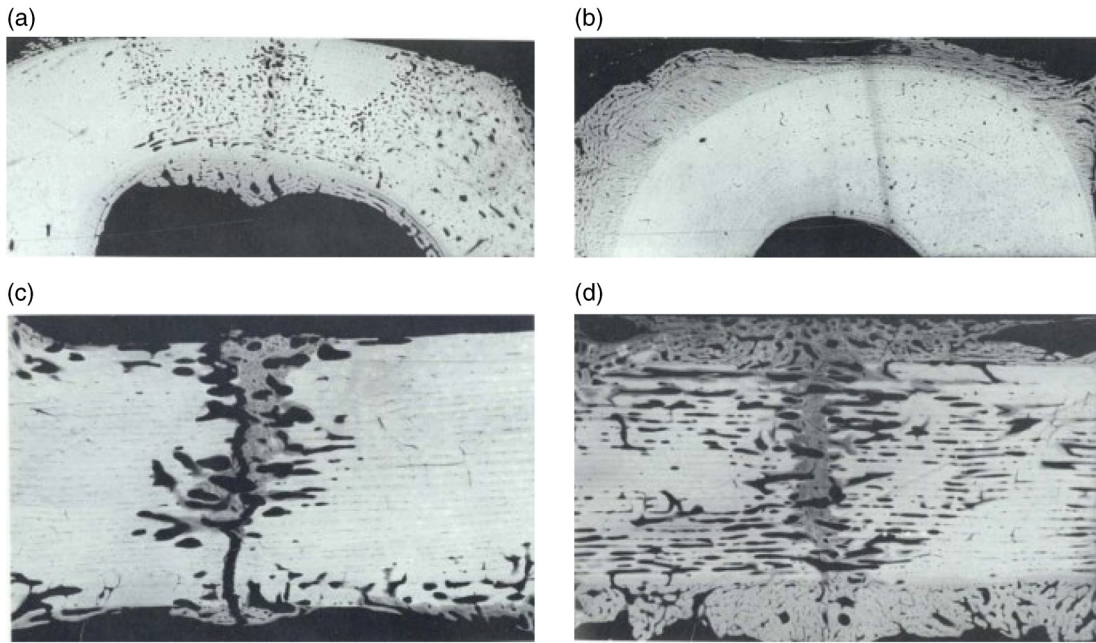
Figure 10: Histological section of a tibia (a)(b) and the cortex (c)(d) in a sheep after 12 weeks of stabilization with a plate. (a) Use of a DCP. The bone shows extensive areas of porosis. (b) Use of PC-Fix. The bone shows minimal porosis of the cortex underneath the plate. (c) Use of a DCP. The bone shows minimal callus production and lack of bridging. (d) Use of PC-Fix. The bone is successfully bridged and shows new callus. Furthermore, periosteal callus is present immediately underneath the plate (top of image) [47].

Gautier et al. [48] were able to directly correlate the disturbance of blood supply underneath an implant to the extent of bone necrosis. This was a game-changing paradigm that showed the importance of preserving the bone-vascular supply and viability instead of focusing mainly on the preservation of soft tissue, also called "biological plating". Because of this, the AO group redesigned the underside of the DCP to be scalloped, reducing its contact area to the bone by more than 50 % as seen in Figure 11 (middle). This new plate design is called the limited-contact DCP (LC-DCP) and is supposed to reduce the implants' negative effects on the bone beneath. A further evolution of the LC-DCP is the point-contact fixator (PC-Fix), which reduces the contact area to a

negligible amount. However, the PC-Fix was discontinued for undisclosed reasons and locking compression plates (LCP) were introduced in 2005 in the veterinary field. As shown in Figure 11 (top), LCP has the same design as DCP but use a locking screw to join the plate to the bone. This allows the LCP to be placed completely away from the bone. Caution has to be taken when fixating the LCP to the bone because it frequently comes in contact with the bone, although not compressed to it [40].
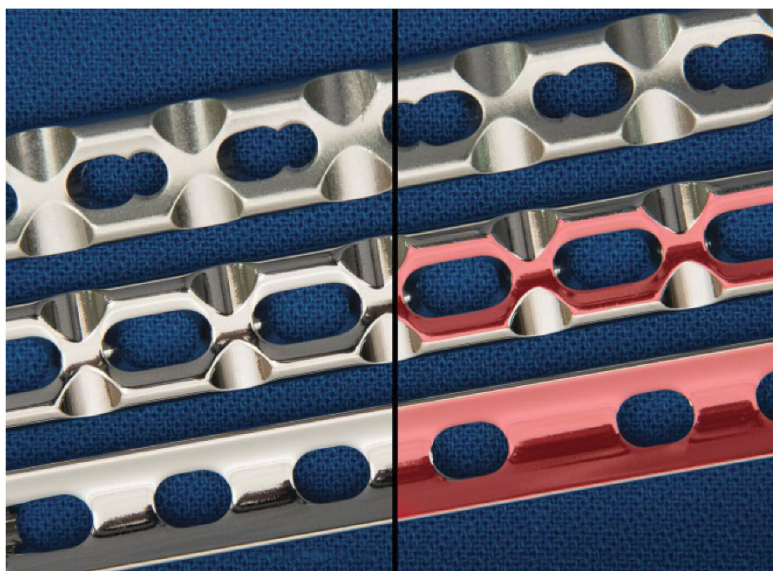
Figure 11: Underside of the LCP (top), LC-DCP (middle) and DCP (bottom). Marked in red is the theoretical contact area between implant and bone. The geometry of the LC-DCP and the LCP is similar, however, the locking hole allows for a gap between the implant and the bone [40].

LCP is rather new to the field of veterinary medicine and has not been fully investigated yet. A common misconception is that locking plates provide more strength to the implant than DCP. However, locking plates were rather designed to enhance the biological osteosynthesis for better healing and minimization of infections. Most of the literature is a result of experience with the LC-DCP and PC-Fix. However, it is reasonable to assume that the influence on the necrosis of locking

plates is less than either of those. Clinically, the importance of blood supply to the bone and its beneficial effect on healing has been well studied [49]. Thus, the decrease of the footprint on the bone and less impact on the vascular system of the bone can be associated with better healing and a lower risk of fracture after removal of the plate. However, some fractures may still benefit from the use of conventional plates, because compression of the fracture surface, rigid stability, and anatomical reconstruction benefit simple fractures and the contact area is influenced by the ability of the surgeon to properly contour the implant to the shape of the bone [40].

Healthy bone is naturally resistant to infections. However, this resistance can be destabilized rapidly if devascularized, unstable, ischemic or in the contact with an extraneous body leading to infections. Especially the pressure that conventional plates excerpt onto the bone, have shown to increase soft tissue infection rates and promote ischemia along the footprint of the implant. The bacteria often colonize on the implant or necrotic bone, developing a biofilm that makes them resistant to natural defenses and antibiotics. Locking plates, however, do not influence the vascular system of the bone in that extend and were already used to treat complicated and infected fractures that resulted from the use of traditional plates. These bones are not strong enough to support a compression screw and sufficiently stabilize the plate. However, due to lack of studies, a conclusion cannot be made about a beneficial effect of locking plates on infection rates, because they are heavily influenced by the design, composition, material, surface topography and biocompatibility of the implant [40].

1.4.3   Locking Systems

The evolution of implants fixation mechanisms as described in chapter 1.4.1 has led to a variety of different locking plate designs. Even though all of them lock the screw into the implant, their different designs give some systems an advantage when it comes to stability, variability or

modifications [50, 51]. This chapter will describe and compare different locking systems. Table 5 gives a summary of features for five different locking systems.

Table 5: Comparison of different veterinary locking systems for pelvic fracture repair [40].

	Locking or nonlocking screws	Axial compression	Variable or fixed-angle screws	Three-dimensional contour
Synthes LCP	Both same hole	Yes	Fixed	Yes, reconstruction only
Orthomed SOP	Locking only	No	Fixed	Yes
Veterinary instrumentation	Both	Variable	Fixed	Yes, reconstruction only
Securos PAX	Locking only	No	Variable	Variable
Kyon ALPS	Both same hole	Yes	Variable for regular screws and fixed for locking screws	Yes
Traumavet Fixin	Locking only	No	Fixed	No

The Advanced Locking Plate System (ALPS) made by the Kyon AG as seen in Figure 12 (a) is developed for the preservation of the vascular system of the bone in veterinary use. The side facing the bone is shaped to minimize bone contact. The system only utilizes monocortical screws to prevent a reduction in endosteal blood supply. Locking as well as a non-locking screw can be used, however, the locking screws must be inserted perpendicular to the plate while the non-locking screws can be inserted up to the angle of 30° longitudinally and 5° transversely. Non-locking screws can be used to fixate the fracture surfaces in compression or neutral mode and can be replaced by locking screws after insertion. The plate has a Sherman-shape, which allows it to be bend to fit the natural shape of the bone in all planes [40].

Figure 12: Different locking plate designs: (a) ALPS [52]; (b) Fixin [40]; (c) PAX [40]; (d) SOP [40]; (e) Synthes LCP [40, 53].

The Fixin system by Traumavet is shown in Figure 12 (b) is different from the other locking systems because it utilizes a screw-insert (bushing)-plate construct. It has a conical shaped screw hole, in which a titanium bushing is inserted. The screw is then inserted into the bushing. When the bushing is screwed into the screw hole it couples with the screwhead and establishes firm joint, that is held in place by friction, elastic deformation, and micro-welding between the bushing and the screwhead. Because the screw-bushing-plate construct of the Fixin system does not undergo deformation it is easier to remove after implantation. Stripping of the screwhead may occur in other systems, the Fixin system, however, has a bushing extractor, which makes removal easy and safe. Furthermore, having the bushing inside the implant, even without a screw inserted, helps increase the resistance to shear forces and allows for thinner locking plates as compares to other systems. This increases the elasticity of the implant and promotes earlier callus formation, less irritation, and impingement on soft tissue structures and clinical and radiographic union [51].

A rather new system is the Liberty Lock System by Scil Animal Care Company, which is a polyaxial system, meaning that the screw can be inserted at a variety of angles. In contrast to other polyaxial systems, the Liberty Lock System does not require the screw to cut threads into the screw hole. Rather, the screw hole has cutouts manufactured into its threads, allowing the screw to be inserted in four different ways. Thus, a maximum angle of 15° in any direction can be achieved and cross threading of the screws can be eliminated. The polyaxial design is beneficial for the insertion and removal of the screw, where insufficient screw locking may be problematic. In addition, certain clinical situations require the screws to be inserted at an angle other than 0° to the implant because of fracture sites, growth plates and joints [40].

Another multidirectional locking plate mechanism is the Polyaxial (PAX) Advanced Locking System by Securos is shown in Figure 12 (c). Screw and plate are made of two different titanium alloys, where the hardness of the screw is about twice the hardness of the plate. This allows the sharp cutting threads of the screw plastically deform the vertical ridges of the screw hole and lock the screw to the plate. While the PAX system is designed to have adequate strength up to an insertion angle of 15°, the push-out strength progressively decreases beyond 5°. A critical factor for the use of the PAX system is the generation enough torque because the push-out strength of the PAX system is dependent on the depth of screw engagement [51, 54]. The recommended insertion torque is 3.5 Nm, while the minimum torque is 2.5 Nm. Overtightening is not an issue because cold welding does not prohibit the threads to cut their way out. After application, the screw head should be about flush with the surrounding plate [40].

The String Of Pearls (SOP) by Orthomed was used in over 100,000 clinical cases and was reported on in many peer-reviewed papers and clinical research presentations [55]. The plates are available in 316 LVM and Ti6Al4V. The screw holes of the system are placed in spherical pearls, which are

connected by cylindrical internodes. They have a threaded bottom part that accepts standard cortical bone screws as seen in Figure 12 (d). The top part of the screw hole has an aperture for the screw head, which produces a secondary interference fit between plate and screw. Due to this design, the screws cannot be inserted at an angle. However, the SOP can be bend into nearly any shape with tools provided by the manufacturer and can be cut to the correct length. The SOP is stronger and stiffer then the self-compressing plates and the screw holes are not the weak points of the system, allowing them to be left empty and placed over a fracture, However, the utilization of conventional screws may have an impact on fatigue life hence their core diameters is rather thin. The SOP can't compress the fracture surfaces to each other and it has a comparatively thick profile [40].

Locking and non-locking screws can be used with the Locking Compression Plate (LCP) by Synthes. It has a combi-hole, which features a threaded and conical part on one side for locking screws and a smooth conical part on the other side as seen in Figure 12 (e), where conventional screws can apply axial compression of the plate to the bone. The locking mechanism in the LCO system is uniaxial thus angle-stable. The locking screw has the same thread leads of 1 mm in the shaft and the head. Conversely, the pitch in the head and shaft is different. The pitch in the head is 0.5 mm and is also known as a 2-start thread, where two sets of threads start on opposite sites of the screw. While the shaft and head spin at the same rate during insertion, the threads in the head move twice as much as the shaft threads. Because the threads get out of phase at around 0.25 mm insertion, the screw locks into place without stripping the threads in the bone [40].

Chapter 2:   Materials and Methods

This chapter focuses on the materials and methods used in this study to implement a locking system into additively manufactured orthopedic implants. The feedstock material is characterized and machine specific process parameters are developed. Different types of heat treatment are conducted to change the mechanical properties of the test specimen. A variety of tools are used to characterize the test specimen. The geometry of a locking system is reverse engineered and manufactured utilizing metal AM technology. A test method is developed to compare the strength of the AM locking system to the conventionally manufactured locking system.

2.1   L-PBF Machine

A Concept Laser MLab Cusing 100R as shown in Figure 13 is used for the production of AM specimen. Its small footprint of only 705 mm x 1848 mm x 1220 mm makes it a suitable machine for small laboratories. Furthermore, a small build volume of only 90 mm x 90 mm x 80 mm enables successful prints of the specimen with minimal powder consumption. The metal laser melting system has a 100 W continuous wave fiber laser with a wavelength of 1070 nm and a spot diameter of approximately 50 µm. In this study, all specimen are produced within a high purity argon gas atmosphere to prevent oxidation of the melt pool [56].

A unique feature about the Concept Laser MLab Cusing 100R is the drawer style technology module, in which the powder feedstock chamber, the build chamber and the powder overflow is installed. This allows for easy cleaning between build jobs during powder change. The technology module can easily be moved from the printer and transferred to a glovebox [56]. The glovebox

should especially be used to safely handle reactive feedstock material such as titanium or aluminum powder because of their increased risk of fire and explosion [57].

Figure 13: Concept Laser MLab Cusing 100R [56].

2.2 Feedstock Materials

Virgin Titanium Ti6Al4V and stainless steel 316L powder are used as the feedstock material as both are commercially available materials. Both materials are provided by Concept Laser and have a particle size of 15 – 45 μm. Their test reports can be found in Appendix A and Appendix B, however additional characterizations also performed in house. The PSD of the Ti6Al4V powder is verified to be between D10 of 22.8 μm and D90 of 54.94 μm and the PSD of 316L powder is confirmed to be between D10 of 18.64 μm and D90 of 42.52 μm using a Microtrac S3500 Particle

Analyzer in dry mode. The PSD for both powders is Gaussian as seen in Figure 14 and Figure 15.

The mean particle size D50 of Ti6Al4V is 35.35 µm, while the D50 of 316L is 26.98 µm.

%-tile	Size [µm]
10	22.80
20	25.32
30	27.39
40	29.32
50	31.35
60	33.64
70	36.39
80	40.21
90	47.1
95	54.94
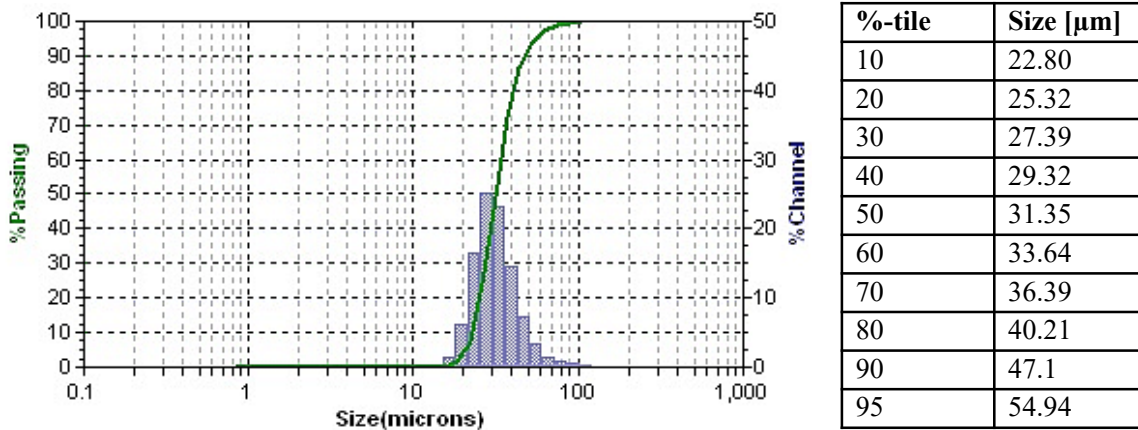
Figure 14: PSD of virgin Ti6Al4V powder used for L-PBF.

%-tile	Size [µm]
10	18.64
20	21.12
30	23.12
40	25.00
50	16.98
60	29.20
70	31.90
80	35.68
90	42.52
95	50.44
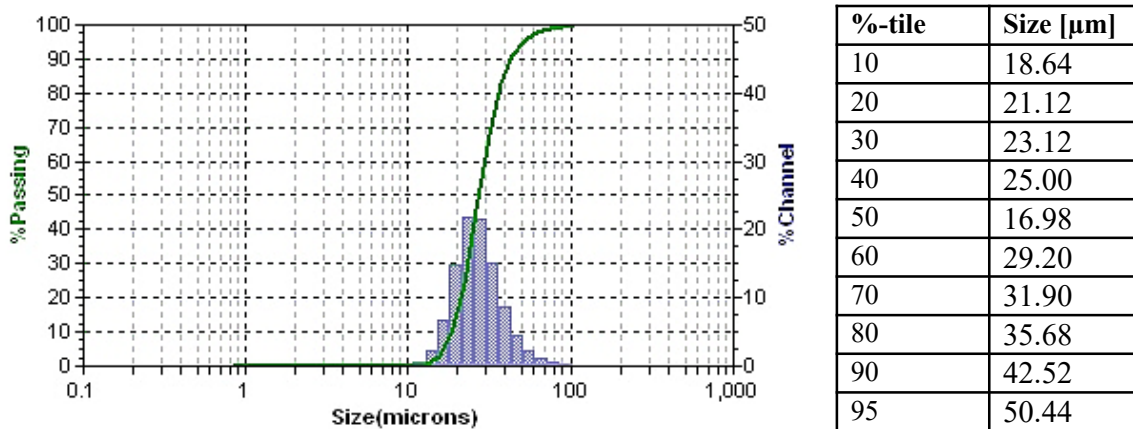
Figure 15: PSD of virgin 316L powder used for L-PBF.

A cylindrical tube with a diameter of 29.37 mm and a height of 25.68 mm is chosen to determine the apparent and tapping density of the virgin powder. The samples are weighed and the densities are calculated from an average of three sample sets. Ti6Al4V powder has an apparent density of 2.65 g/mm^3 and a tapping density of 2.79 g/mm^3, while 316L powder has an apparent density of 4.69 g/mm^3 and a tapping density of 5.02 g/mm^3.
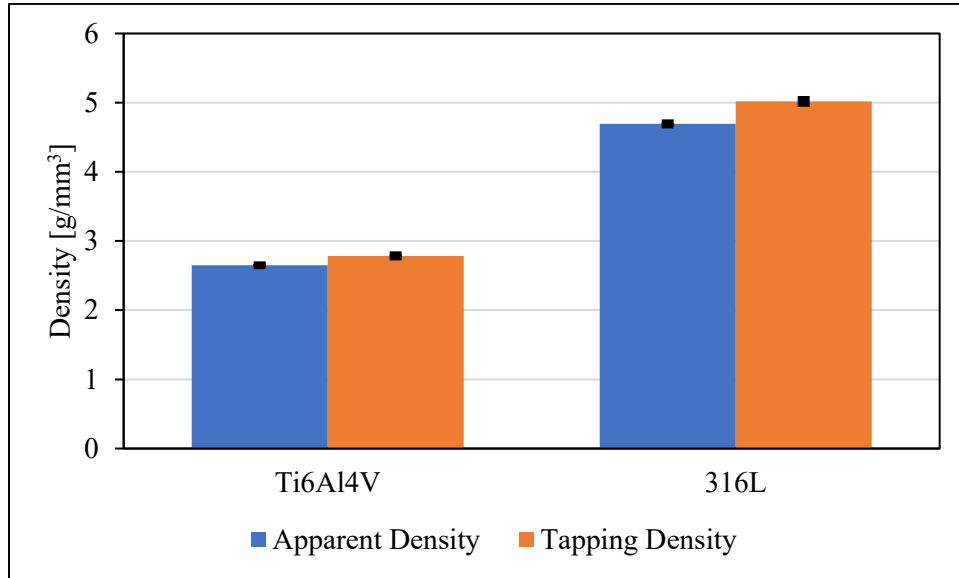
Figure 16: Apparent and tapping density of virgin Ti6Al4V and 316L powder.

A JEOL JSM-7000F Scanning Electron Microscope (SEM) equipped with Energy Dispersive X-Ray Spectroscopy (EDS) is used to analyze the geometry of the feedstock powder. The powder particles for the Ti6Al4V powder are primarily spherical in shape as seen in Figure 17 (left). It shows only a few satellites. The surface of the particles is smooth. The 316L powder is mainly spherical as seen in Figure 17 (right). However, elongated and irregular shaped particles are also present. Furthermore, the particles show bigger satellites with some of the particles showing major agglomeration of smaller particles.

The microstructure of the feedstock powder is analyzed as shown in Figure 30 and Figure 28 using a Bruker D8 Diffractometer (XRD) with a Cu X-ray source set at a working current of 40 mA and a voltage of 40 kV. The XRD peaks present are compared XRD diffractograms reported in the literature [15, 20, 58-60] and found to be fully austenitic for the 316L stainless steel powder and fully α-phase in the Ti6Al4V powder.
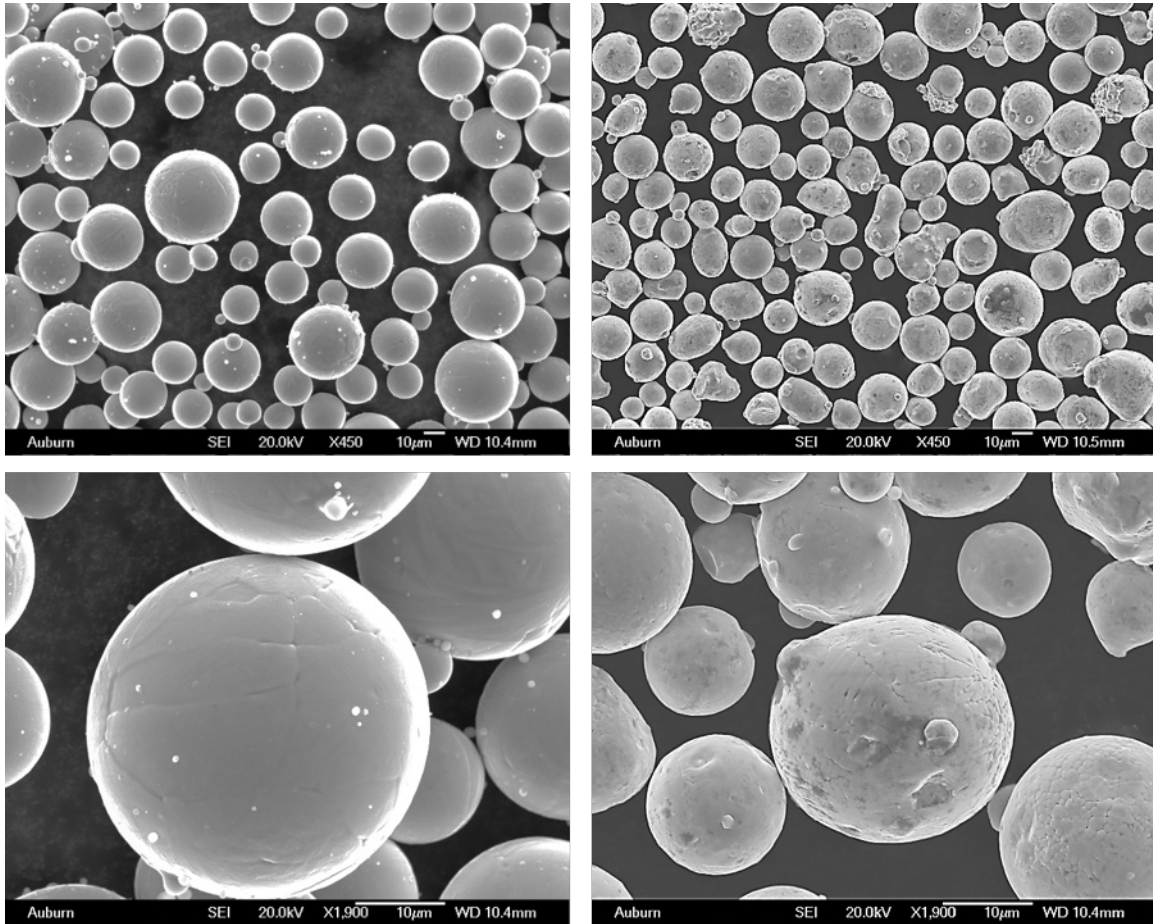
Figure 17: SEM images of virgin Ti6Al4V powder (left) and 316L powder (right).

2.3   Process Parameter Development

Process parameter studies are performed for both Ti6Al4V and 316L. As described in

Chapter 1.2.1, trial and error experiments are performed. To reduce time and material consumption,

work of other researchers [18, 19, 21, 61, 62] that use the same type of machine is reviewed and

summarized in Table 6 to narrow down the process window. Cubic shaped test samples of

10 mm x 10 mm x 10 mm are printed. A cross section of the samples is polished and OM is used

to take high-quality images. Because solid material appears white and pores show up black a

threshold is applied and the area of solid material is calculated as described by Thomas et al. [19]

and Debbroy et al. [1].

Table 6: Review of process parameters for Concept Laser MLab Cusing 100.

Ref.	Material	Laser Power	Scan Speed	Hatch Distance	Layer Thickness
[61]	316L	90 W	600 mm/s	84 μm	25 μm
[19]	316L	90 W	600 mm/s	84 μm	25 μm
[21]	Ti6Al4V	95 W	900 mm/s	n.a.	30 μm
[62]	Ti6Al4V	95W	900 mm/s	77 μm	25 μm
[18]	Ti6Al4V	75 W	600 mm/s	77 μm	25 μm

Even though the literature showed the same process parameters for optimal densities for 316L, a study on the process parameter is performed to gain an understanding of the effects of the hatching distance. For this, the laser power, scan speed, and layer thickness are kept constant at 90 W, 600 mm/s and 25 μm, respectively. The hatch distance of the samples is increased in intervals of 15 μm starting at 50 μm until 125 μm. Table 7 lists all process parameters and their corresponding volumetric energy density. A contour scan is performed as suggested by Pham et al. [61] with a reduced laser power of 60 W.

Table 7: Process parameters for density study on AM 316L stainless steel.

Sample Name	Laser Power	Scan Speed	Hatch Distance	Layer Thickness	Vol. Energy Density
S1	90 W	600 mm/s	50 μm	25 μm	120 J/mm^3
S2	90 W	600 mm/s	65 μm	25 μm	92 J/mm^3
S3	90 W	600 mm/s	80 μm.	25 μm	75 J/mm^3
S4	90 W	600 mm/s	95 μm	25 μm	63 J/mm^3
S5	90 W	600 mm/s	110 μm	25 μm	55 J/mm^3
S6	90 W	600 mm/s	110 μm	25 μm	48 J/mm^3

The parameter study for Ti6Al4V takes a different approach with a wider variability, as the literature [18, 21, 62] gives suggestions for two different laser powers, 95 W and 75 W. Instead of keeping all other variables but one constant, this parameter study keeps the volumetric energy density constant at roughly 44 J/mm^3 in four samples at 95 W laser power and 65 J/mm^3 in five

samples at 75 W laser power. Additional samples are printed using slightly higher and lower energy densities to explore the parameter space even further. The complete spectrum of all printed Ti6Al4V samples can be seen in Table 8.

Table 8: Process parameters for density study on AM Ti6Al4V.

Sample Name	Laser Power	Scan Speed	Hatch Distance	Layer Thickness	Vol. Energy Density
T1	95 W	900 mm/s	77 μm	25 μm	54.83 J/mm^3
T2	95 W	900 mm/s	95 μm	25 μm	44.44 J/mm^3
T3	95 W	800 mm/s	107 μm	25 μm	44.39 J/mm^3
T4	95 W	700 mm/s	125 μm	25 μm	43.43 J/mm^3
T5	95 W	1000 mm/s	84 μm	25 μm	45.24 J/mm^3
T6	95 W	800 mm/s	120 μm	25 μm	39.58 J/mm^3
T7	95 W	900 mm/s	120 μm	25 μm	35.19 J/mm^3
T8	75 W	600 mm/s	77 μm	25 μm	64.94 J/mm^3
T9	75 W	700 mm/s	65 μm	25 μm	65.93 J/mm^3
T10	75 W	800 mm/s	55 μm	25 μm	68.18 J/mm^3
T11	75 W	500 mm/s	90 μm	25 μm	66.67 J/mm^3
T12	75 W	400 mm/s	110 μm	25 μm	68.18 J/mm^3
T13	75 W	600 mm/s	55 μm	25 μm	90.91 J/mm^3
T14	75 W	600 mm/s	120 μm	25 μm	41.67 J/mm^3
T15	75 W	700 mm/s	95 μm	25 μm	45.11 J/mm^3

To improve the surface roughness, a parameter study with different contour scans is performed on Ti6Al4V samples. The contour scan can improve the surface roughness of an AM part by fusing together the rough ends of the volume hatching, thus establishing a solid melt pool along the interface between powder bed and part [63]. However, the final roughness of the part is also dependent on parameters used for the contour scan [63].

The samples have a rhombohedron shape with a 5 mm x 5 mm square base and a height of 5 mm. The rhombohedron has 60° flanks that allow for the investigation of the upskin and a downskin as shown in Figure 18. The contour scan's laser power is changed from 55 W to 95 W in 15 W

intervals and the scan velocity is changed from 400 mm/s to 1000 mm/s in 200 mm/s steps. A 500 μm x 500 μm section on the side, upskin, and downskin are measured using a Nanovea ST400 Profilometer and the arithmetic mean height of the area is given as the surface roughness. To compare the samples to each other, the average roughness of upskin, downskin and side is calculated.
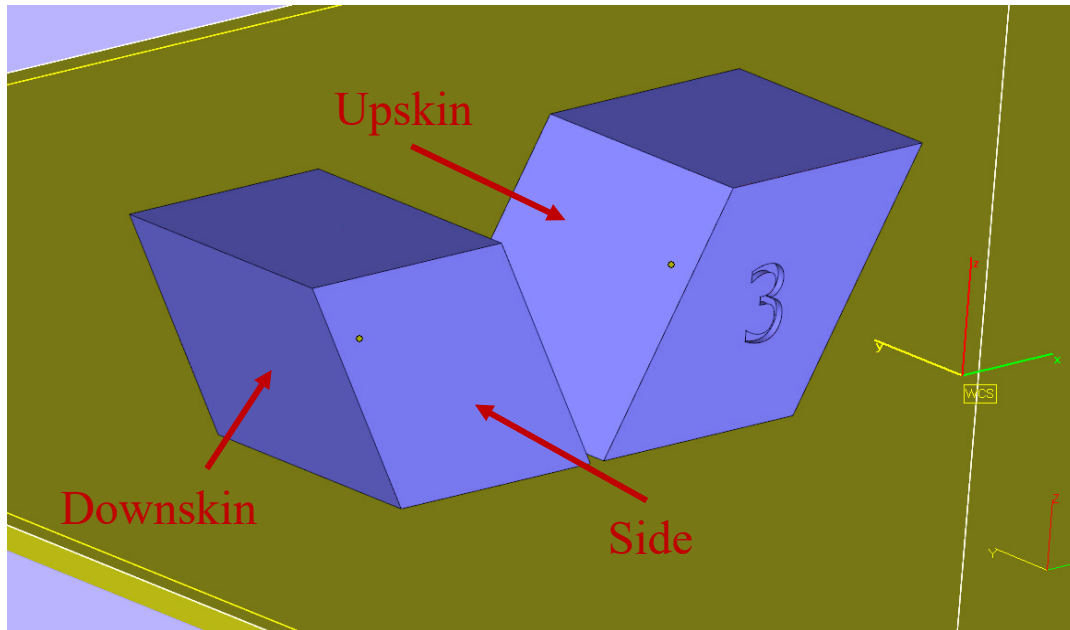
Figure 18: Rhomohedron shaped surface study specimen showing the location of the upskin, downskin, and the side.

2.4 Heat Treatment

All samples were heat treated. Chapter 1.3.2 describes the significant strengthening effects of Ti6Al4V due to heat treatment because of its phase change during cooling. Therefore, a variety of heat treatments are chosen based on literature [15, 37-39]. The following heat treatments are performed for Ti6Al4V: stress relieving at 595 °C for 2 and 4 hours with subsequent air cooling, mill anneal at 750 °C for 2 hours with air cooling. These heat treatments preserve the microstructure and will reduce the amount of residual stress [14, 37, 38]. β-anneal at 1050 °C for

2 hours with subsequent water quench, air cooling and furnace cooling (FC) according to Galarraga et al. [15, 39], who reported a variation in hardness for this heat treatment.

Due to its weak response to heat treatment as described in Chapter 1.3.1, only two types of heat treatment are performed: stress relief at 650 °C for 2 hours with succeeding air cooling and annealing at 1121 °C for 1 hour with succeeding water quench as suggested by [60, 64, 65].

2.5 Microstructure and Hardness

All samples are cut and polished parallel to the build direction. The images are always taken so that the lower end of the part is at the bottom of the image. The microstructure is revealed using Adler's etchant (PACE technology) for 316L stainless steel samples and Kroll's reagent (PACE technology) for Ti6Al4V titanium samples. The analysis is performed on an Olympus BX51 optical microscope with a DP73 camera for image acquisition. The microstructural phases are further verified using XRD.

Hardness is defined as the resistance of a material against indentation [66] and therefore a good qualifier for the working principle of the locking system under investigation. The Vickers microhardness is recorded using a LECO DM-400 Hardness Tester with a 1000 g load for 30 seconds. The average hardness is calculated for each samples using 15 measurements taken at random locations.

2.6 Locking System and Build Preparation

The PAX locking system is chosen because of its ability to insert screws in various insertion angles, giving the surgeon options for screw insertion and its simple geometry and lack of threads, which allows it to be manufactured additively without post-processing. The exact reference model is 3. mm Locking screws and a corresponding 3.5 mm reconstruction plate. A focus is set on testing the screw system for different orientations during the build. This allows the locking screw system

to be implemented in patient-specific metallic orthopedic implants, which is one of the key advantages of AM. Dobbe et al. [41] already used a patient-specific implant with a locking system. However, they acknowledged, that cutting threats into the implants in a post-processing step was costly, thus implementing a locking system with less post-processing required can decrease manufacturing cost and make patient-specific implants more affordable.

A Pinnacle X-Ray Solutions Benchmark 225/60 system is used to reverse engineer the geometry of the PAX system. The XCT has a micro-focus tube installed that allows for the capture of a reconstruction image with a voxel resolution of less than 2 µm [67]. The scan can be seen in Figure 19 (b). After reconstruction of the part a three-hole section is extracted from the voxel-based file as marked in red in Figure 19 (b) and converted into a Standard Tessellation Language (.stl)-file. The .stl-file is then transferred into Materialize Magics, a software that allows for the placement of the build files on the build plates and the generation of support structures which is displayed in Figure 19 (c). Four specimen is printed in three different orientations each (H: Horizontal, parallel to the build plate; D: Diagonal, at 45 ° to the build plate; V: Vertical, perpendicular to the build plate) in order to account for printing errors occurring during manufacturing, i.e. due to large overhangs. The vertical samples have minimal support to reduce the negative effect of overhanging sections. After the build job preparation, a Concept Laser post processor slices the build file and converts them into a machine-readable file which can be sent to the Concept Laser MLab Cusing 100R. The final build job is shown in Figure 19 (d).
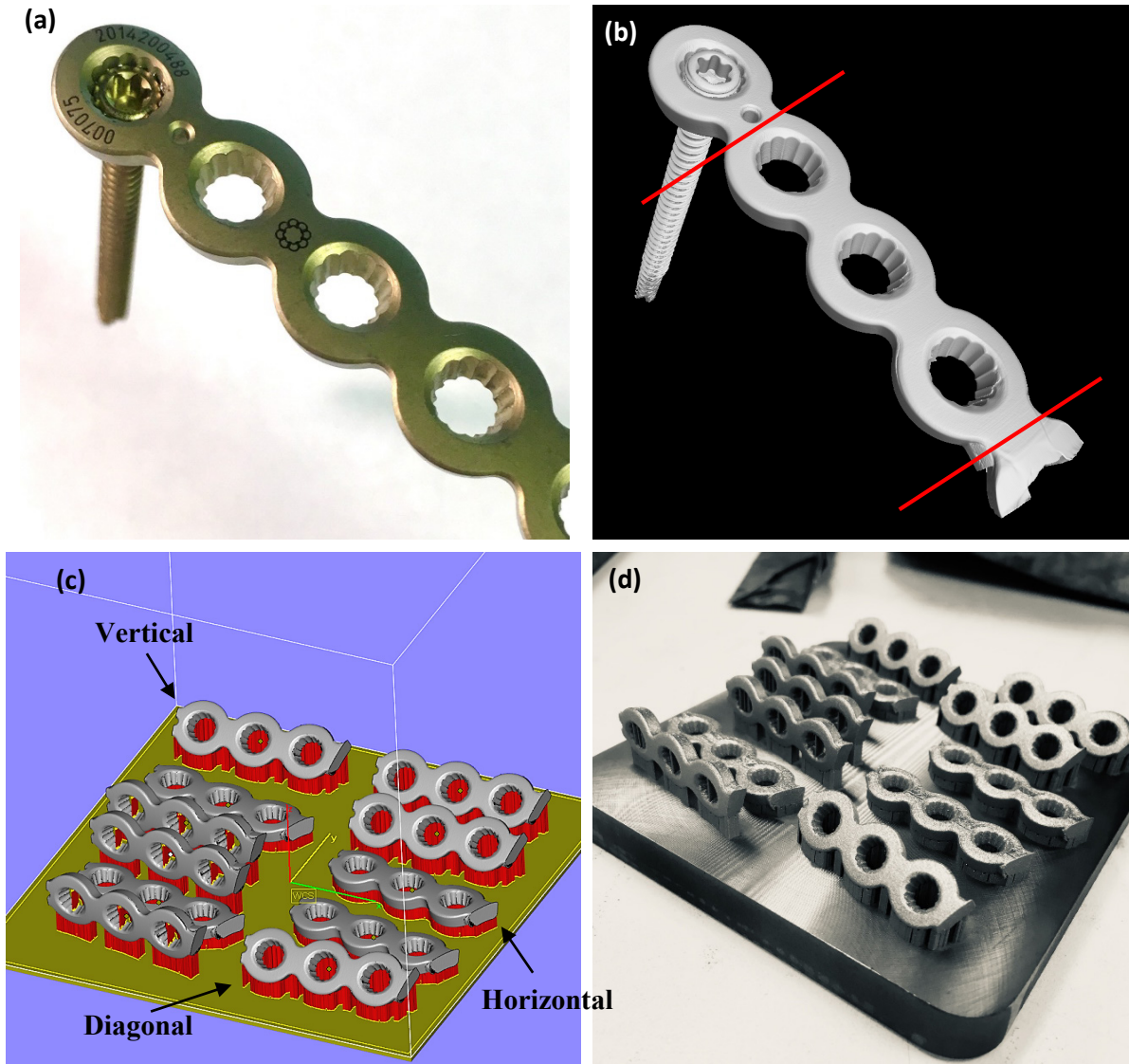
Figure 19: Reverse Engineering the PAX locking system: (a) Image of the original part; (b) XCT-Scan of the section of interest. The red lines mark where the sample is cut in order to receive 3 hole test specimen; (c) Build job preparation including positioning and orientation of multiple test specimen and support generation; (d) Final printed test specimen in the as-printed state attached to the build plate.

2.7   Testing of the Locking System

The push-out force is chosen as a measure of strength for the additively manufactured locking system. In order to keep the results comparable, the screws are inserted into the screw hole by the

same person (RF). For straight insertion into the hole, a hole with a diameter of 3.5 mm is drilled into an aluminum block. The hole of the test specimen is placed concentrically on top of the hole and is locked into place using clamping tongs. A high-accuracy dial torque-measuring wrench by Precision Instruments is used to torque the screws until a final torque of 2.5 Nm is reached as seen in Figure 20 (a).

Figure 20: Insertion of the screw using a fixture for angle control and a torque measuring screwdriver.

The displacement of the screw due to insertion is measured using a KEYENCE VHX-6000 Digital Microscope. A complete image with height information is taken as shown in Figure 21 (a) and (b). Due to its rounded shape, the lowest and the highest points of the plate are chosen as significant points. The red line in Figure 21 (a) marks, where the height profile at the lowest point of the plate is taken. The resulting height profiles before and after are shown in Figure 21 (c) and (d), respectively. The highest points of the screw head and the peaks of the plate are chosen as reference

points. The vertical distance between the midpoints of two significant points of the head and the

plate is measured and the displacement is calculated.
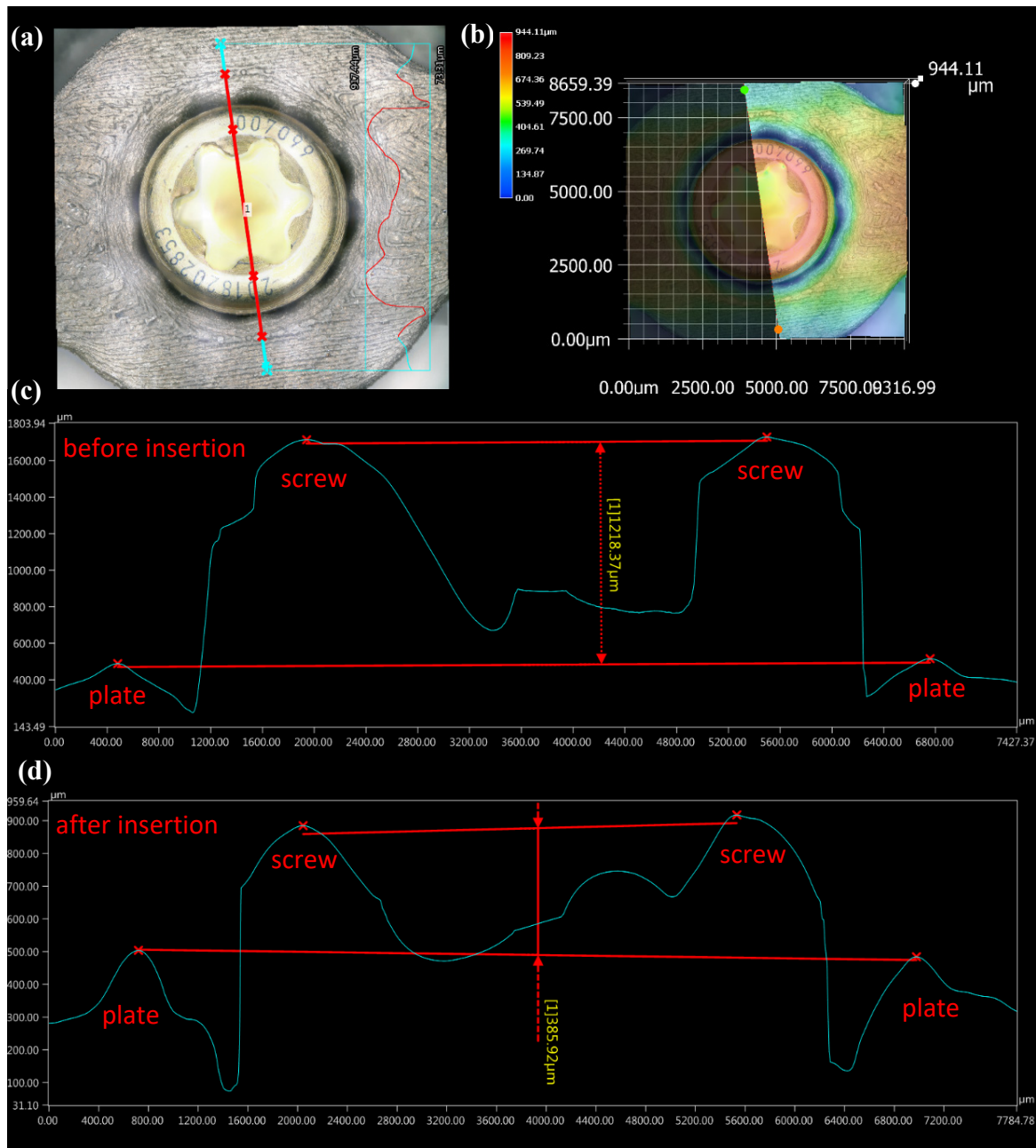
Figure 21: Measurement of the height profile for the displacement during insertion: (a) image of the screw and plate with location of height profile marked in red; (b) 3D-data of the height of plate and screw, hight is marked in colors; measurement of the height difference between plate and screw head before (c) and after (d) insertion.

Figure 20 (b) shows the testing rig for the measurement of the push-out force. An MTS QTest 100

Tensile Tester with a 100 kN load cell in compression mode is used. A fixture as shown in Figure

22 (a) is made using AM to accommodate three holes of the locking plate. The area where the plate

is placed is rounded and has two small nubs to reduce the amount of play. The hole in the middle

has a wide opening to allow the screw to pass through without interference. Figure 22 (b) shows

the complete assembly installed in the compression rig, where it is compressed at a speed of 1.27

mm/min. The load over displacement curves are recorded at 10 Hz.
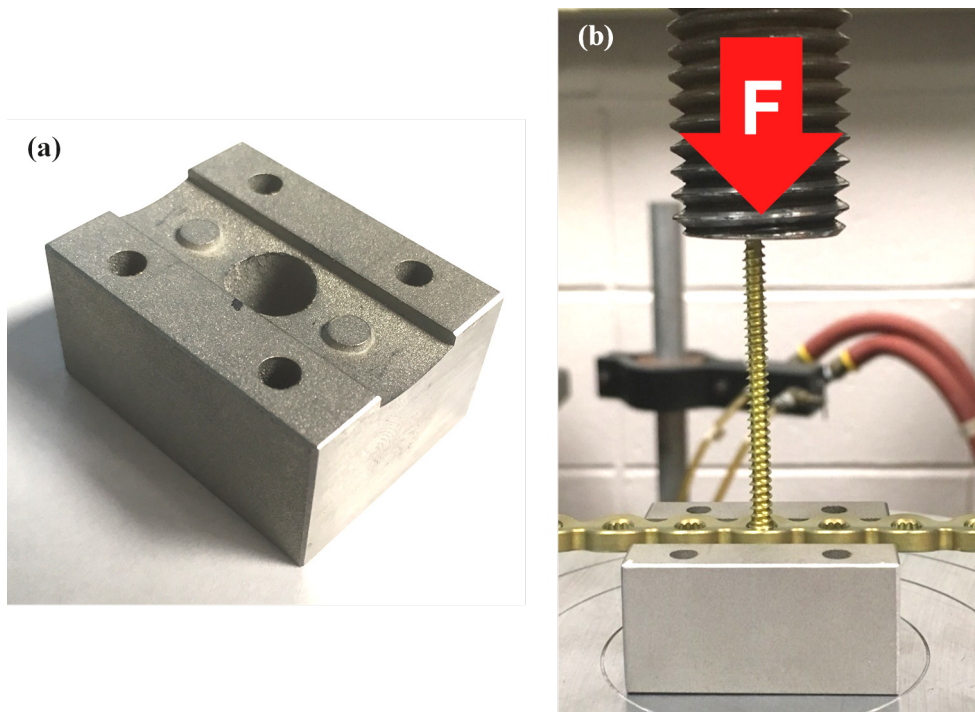
Figure 22: (a) Test stage to accommodate a specimen. (b) Testing rig in compression for

measuring the force needed to push out the screw from the implant. A force (F) is applied

vertically on the screw.

Chapter 3:   Results and Discussion

The following chapter discusses the results found in the experiments conducted in this chapter. The analysis starts with the determination of processing parameters that allow the manufacturing of high-density near-net-shape parts using AM. The parts are then heat treated in order to find mechanical properties that are close to the PAX reference. The samples are tested and their strength is evaluated.

3.1   Density, Defects, Surface Roughness

Figure 23 shows an example of cross section of three 316L samples produced with different hatching distances. Figure 23 (a) shows major signs of irregularly shaped pores caused by LoF. The many small pores in Figure 23 (c) are a sign of too much energy input leading to keyholes. Figure 23 (b) is a cross-section of a near full density part. Cross sections like this are desirable because they don't have stress concentrators which can lead to cracks a described in Chapter 1.2.3. The results for the density studies for Ti6Al4V at 95 W and 75 W laser power and 316L at 90 W laser power can be seen in Figure 24 and Figure 25, respectively. Three regions are identified that are subject to the same types of defects. Regions marked (a) experienced LoF porosity and regions marked with (c) were subject to porosity due to the keyhole effect as described in Chapter 1.2.3. The best parameters are found to be in the regions marked (b). Examples for cross sections for those regions can be seen in Figure 23(a), (b) and (c). Because of the high densities of 99.82±0.02 % of sample T1 and 99.9±0.04 % of sample S3, their parameter sets are chosen for the fabrication of any part hereafter.
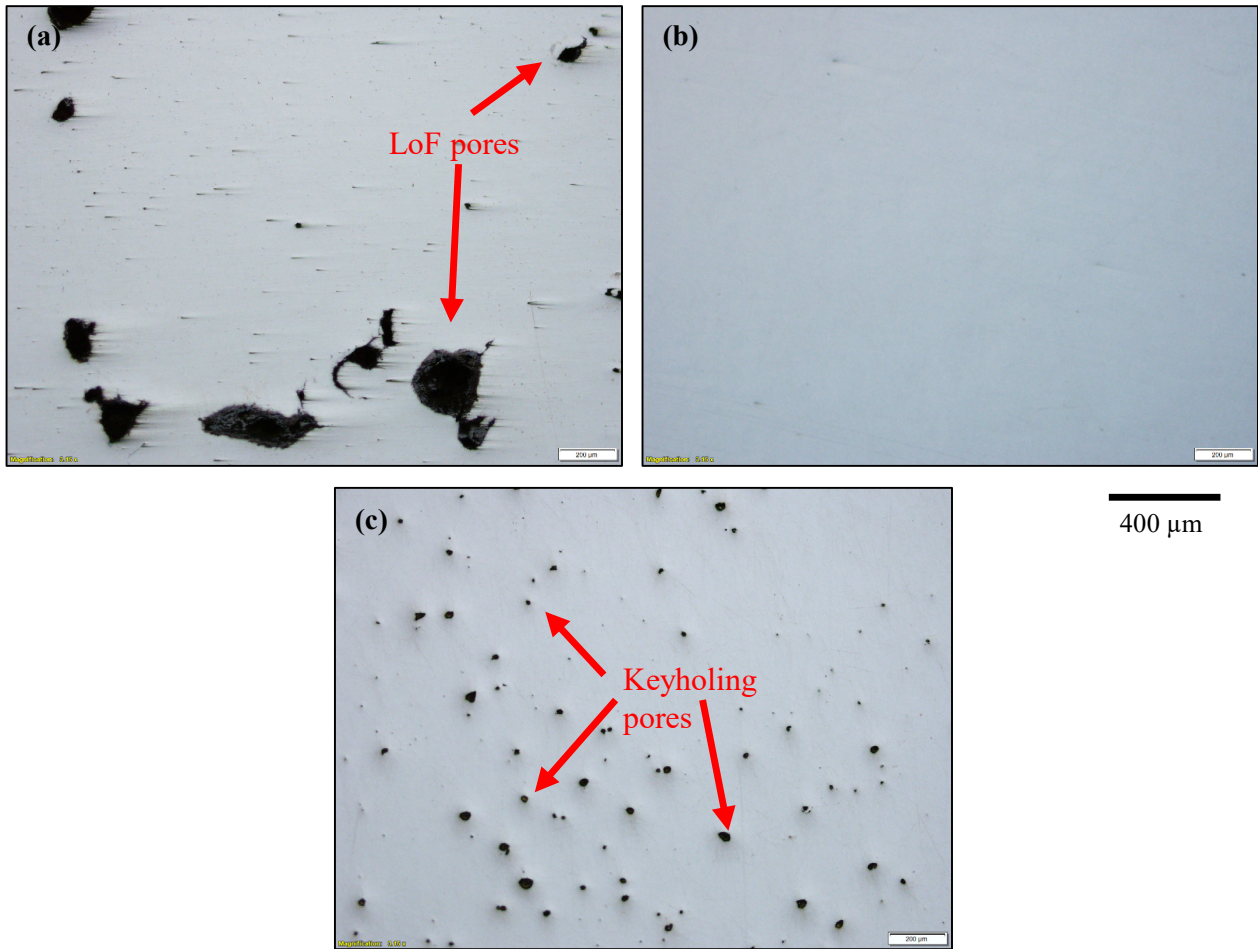
Figure 23: Typical cross sections found in the parameter study of 316L: (a) major LoF defects at high hatching space; (b) little porosity; (c) major defects cause by the keyhole effect.
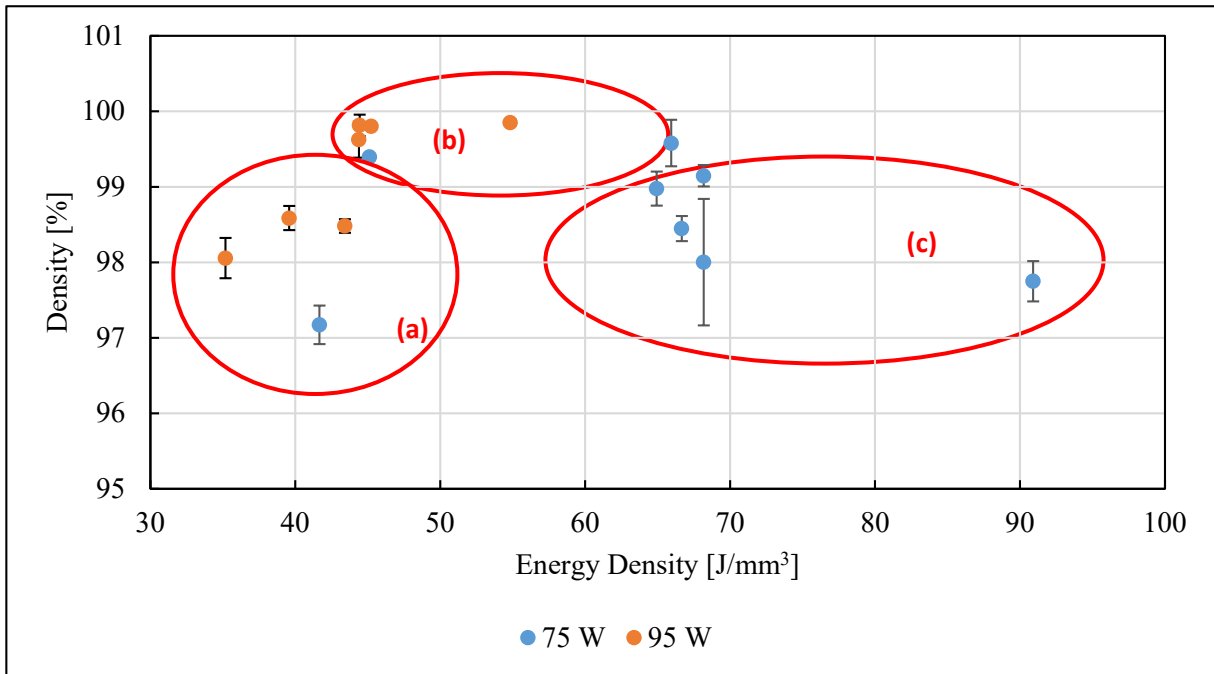
Figure 24: Density study for as printed AM Ti6Al4V for different energy densities at two laser powers: (a) Region with many LoF defects; (b) region with very good densities; (c) region with a tendency towards keyhole porosity. Colors represent the Laser Power
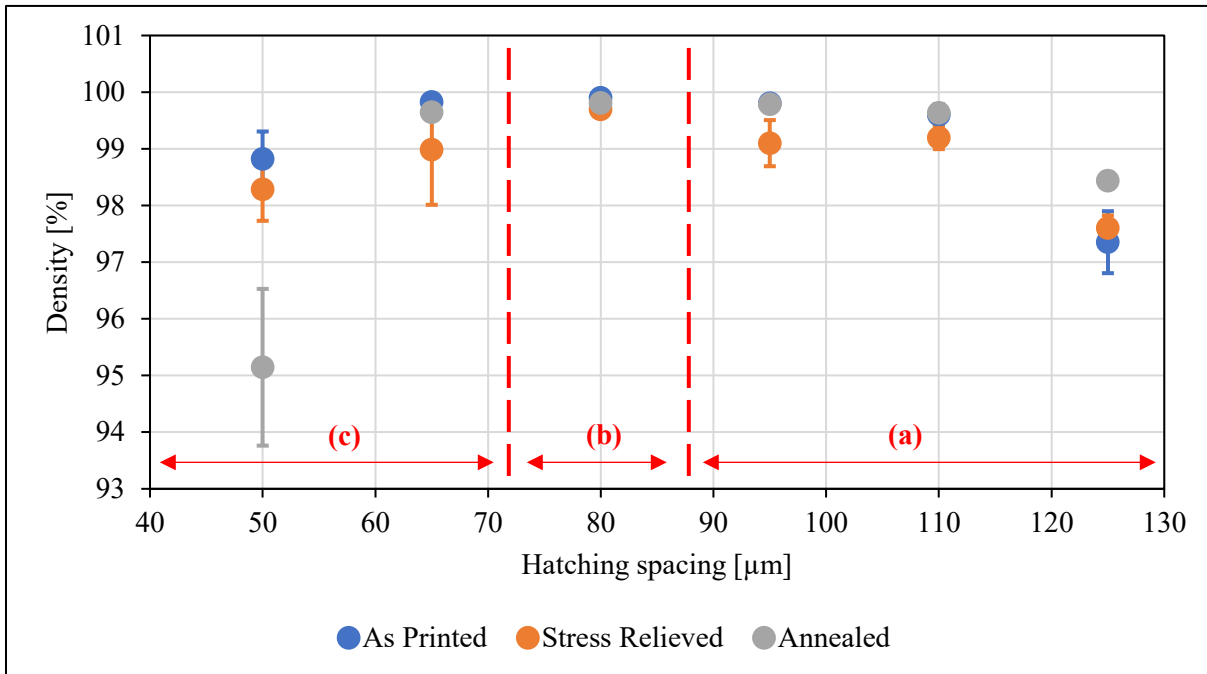
Figure 25: Density of AM 316L samples at differing hatching distance with a laser power of 90 W and a scan speed of 600 mm/s. (a) Region with a higher concentration of LoF defects; (b) region with very good densities; (c) region with a tendency towards keyhole porosity.

Figure 26 shows the average surface roughness of the upskin, downskin, and side of the rhombohedron shaped roughness specimen made from Ti6Al4V. A trend towards increased surface roughness can be observed when the scan velocity is increased. The highest averaged surface roughness is measured at the lowest laser power of 55 W and high velocity. The lowest averaged surface roughness is S_a=10.89 μm. The parameters are a single contour scan with 85 W and a speed of 600 mm/s. This parameter set is used to produce any further Ti6Al4V specimen.
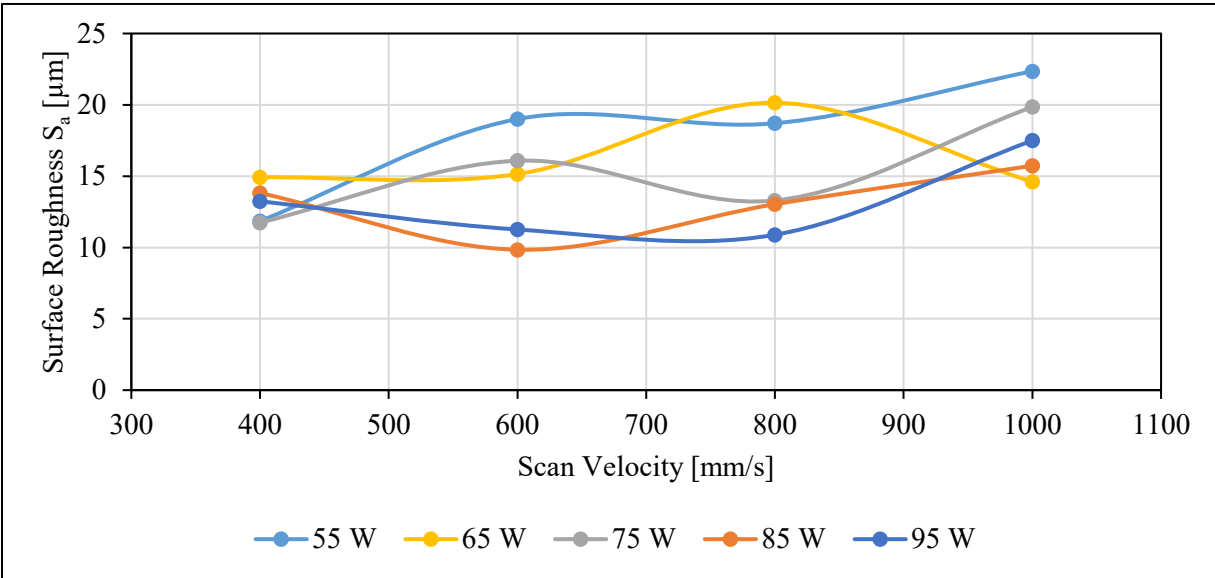
Figure 26: Averaged arithmetic surface roughness S_a of AM Ti6Al4V samples with different parameters for the contour scan. The different colored lines represent Laser Power.

3.2   Microstructure

The cross-section of the as printed Ti6Al4V sample in Figure 27 (a) reveals elongated grains growing in the build direction over several hundred µm. These grains are prior epitaxially grown β-grains originating from the remelting of the subsequent layers. Their growth direction is dependent on the local heat transfer conditions. The β-phase transforms into a very fine acicular martensitic phase, or α', due to the high cooling rates experienced during L-PBF. One can clearly see the needle-shaped grains formed during this transition. XRD in Figure 28 shows only α/α' peaks and no β-peaks.

Figure 27 (b) and (c) show samples at two different sub-transus temperatures for the reduction of residual stress which originates from the volume reduction during cooling. No significant difference to the as printed sample can be seen. However, the XRD results for the mill annealed sample show a slight β-peak, suggesting that the α' phase has decomposed to α and β.

50

Super-transus heat treatment was conducted for the samples in Figure 27 (d), (e) and (f) meaning that the α' phase from the as printed samples was completely transformed into β-phase. An indication for this is the grain growth that is visible in all three samples. The sample with the highest cooling rate in Figure 27 (d) shows very thin lamellar α' martensite. The air-cooled sample in Figure 27 (e) shows α-Widmanstätten microstructure inside the grains. The final sample in Figure 27 (f) shows very lamellar α and β grain. α is the white phase while β is the black phase sitting in the grain boundaries. Because of this samples showed the lowest hardness as described in Chapter 3.3, it XRD was used to verify the presence of both α and β phases.

Figure 29 shows the microstructures of as printed, stress relieved and annealed AM 316L specimen observed under OM. The as printed and stress relieved cross sections are shown in Figure 29 (a) and (b), respectively, show the melt pool boundaries (red arrows), proving that the powder particles melted and solidified. The melt pools overlap, showing that the melt laser tracks were able to fuse the individual tracks together. Furthermore, it can be seen that the melt pools have a greater depth than the layer thickness, proving that the laser melts more than just the current layer during exposure. Grains grow across the melt pools in the build direction following the heat gradient (green arrows). During annealing the melt pool boundaries completely dissolve, leaving behind only the grains as seen in Figure 29 (c). The red arrows point out the appearance of twinning boundaries. Furthermore, very small precipitates can be observed as shown in Figure 29 (d).

The XRD diffractograms in Figure 30 lead to the assumption that 316L did not experience a phase change. All peaks starting from the powder and the as printed samples, until the heat treated samples after stress relieve and annealing show only the fcc-austenitic phase.
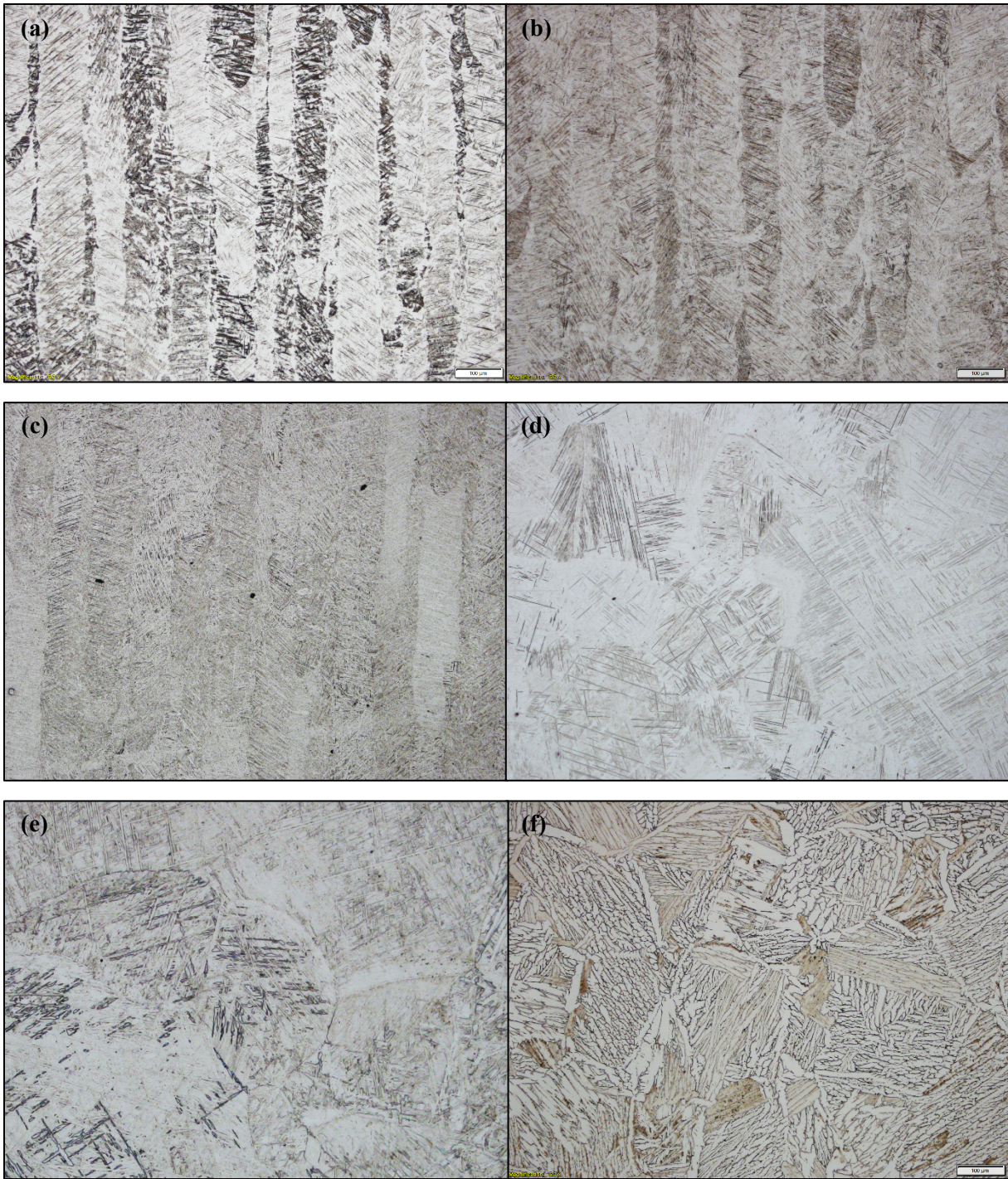
Figure 27: Microstructure of AM Ti6Al4V: (a) as printed; (b) stress relieved at 595 °C for 2 hours, air cooled; (c) mill annealed at 750 °C for 2 hours, air cooled; β-annealed at 1050 °C for 1 hour, water quenched (d), air-cooled (e) and furnace cooled (f).
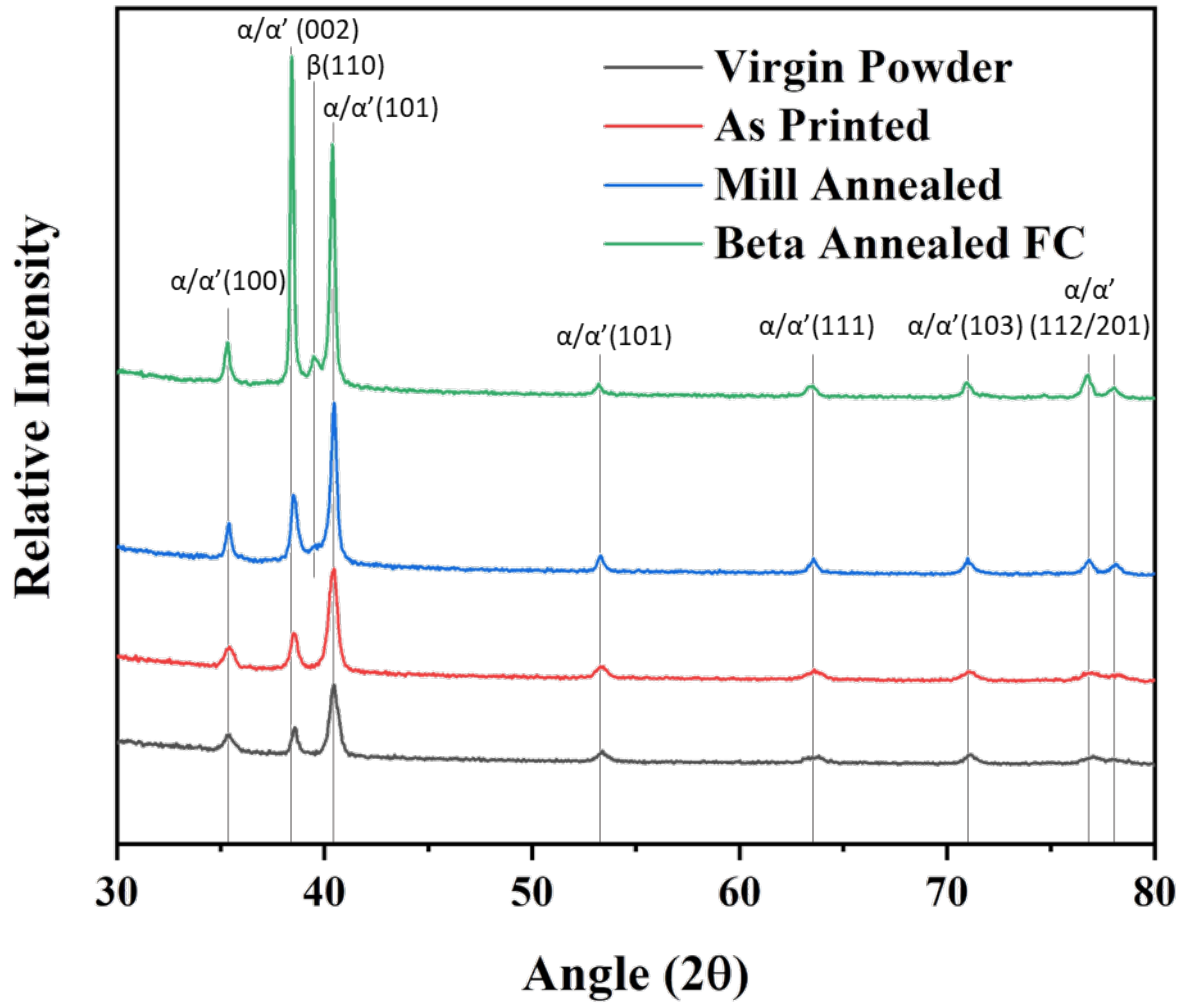
Figure 28: XRD-diffractogram for Ti6Al4V virgin powder, as printed, mill annealed and β-annealed furnace cooled.
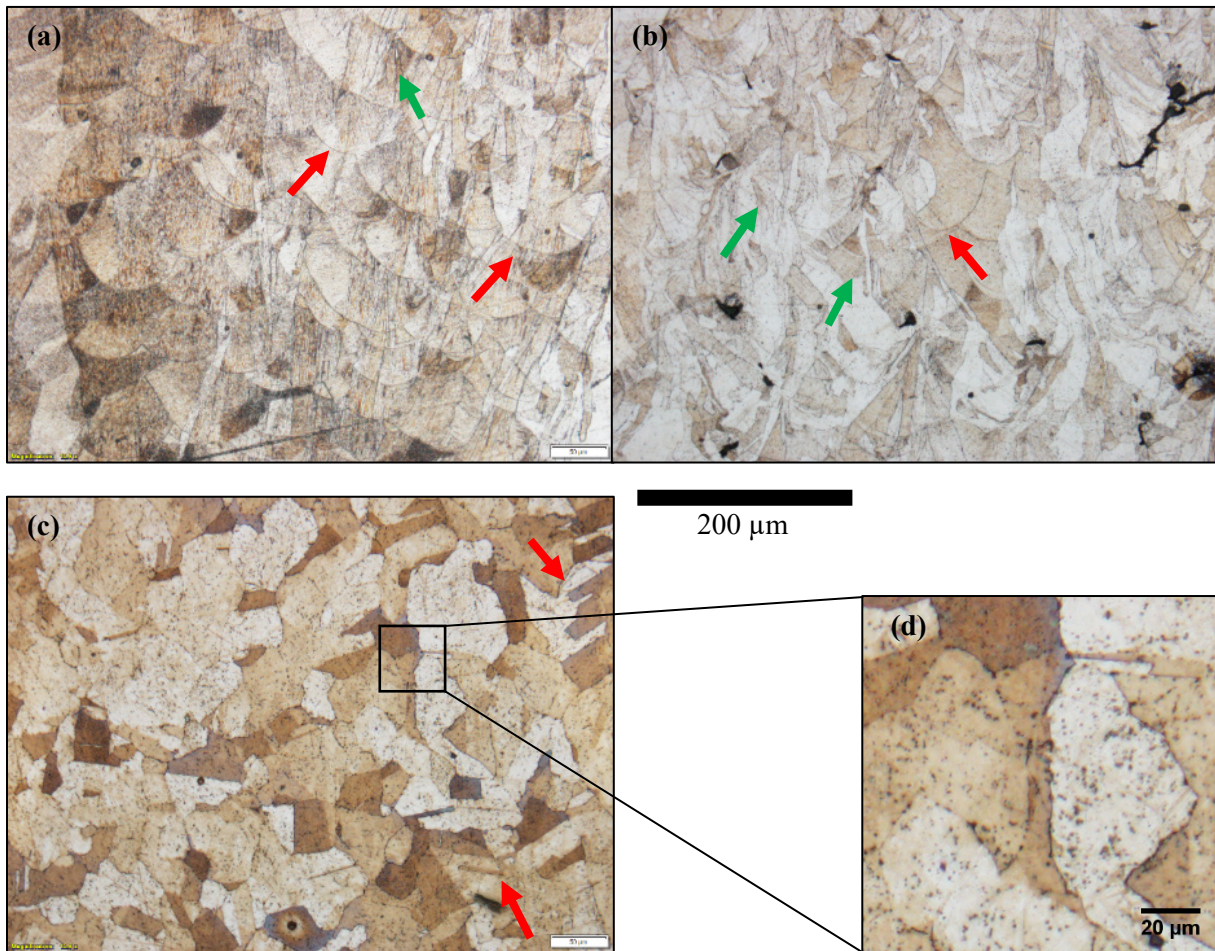
Figure 29: Microstructural evolution of AM 316L stainless steel: (a) as printed and (b) stress relieved, where red arrows mark melt pool boundaries and green arrows mark grains growing into build direction; (c) annealed, the red arrows indicate the position of twinning boundaries; (d) higher magnification image of the annealed samples showing the occurrence of very small precipitates (black).
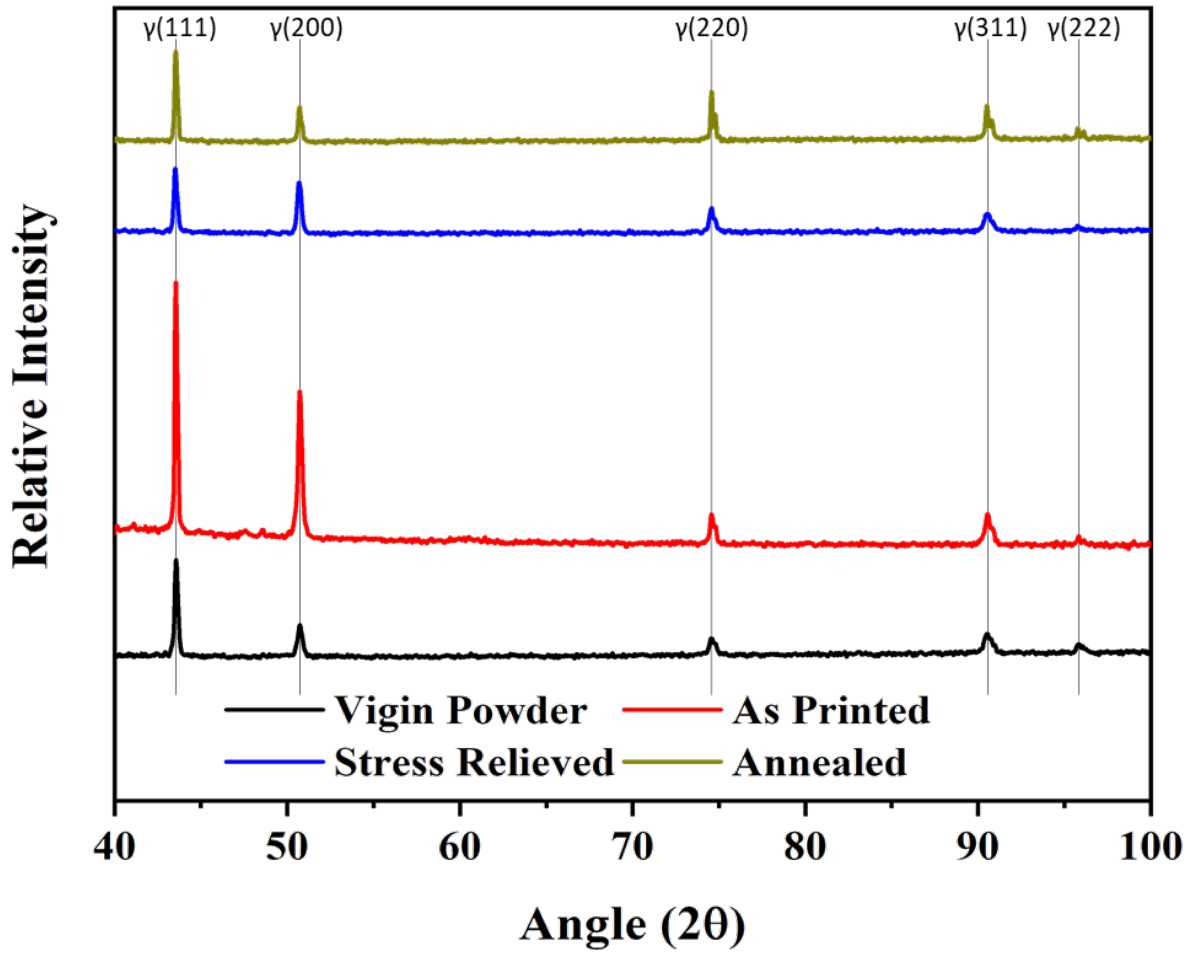
Figure 30: XRD diffractogram of 316L virgin powder, As Printed, Stress Relieved and Annealed.

3.3   Hardness

The Vickers microhardness is determined for all materials in use. It is found that the hardness of the screw of the PAX system is 300±5.8 Hardness Vickers (HV) and therefore roughly 50 % harder than its locking plate with only 205±9.8 HV. This difference is the reason for the screw threads to be able to cut into the hole, establishing a cold weld that locks the screw into place.
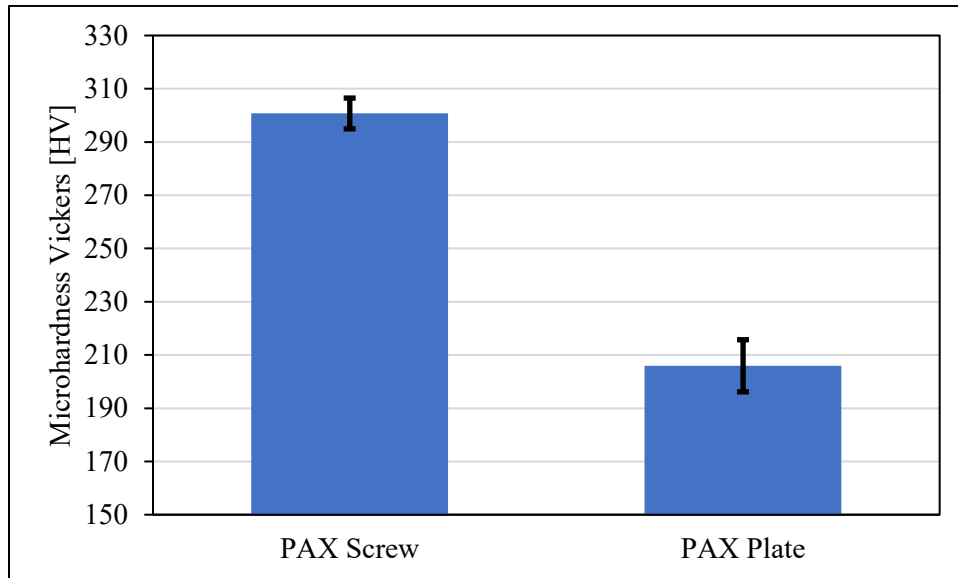
Figure 31: Microhardness (Vickers, 1000g, 30 s) of the PAX screw and plate.

Ti6Al4V is the best material when it comes to medical applications [35], but it already has a high hardness of 360±6.7 HV as seen in Figure 32. Therefore, the heat treatments described in Chapter 2.4 are conducted with the goal of lowering the hardness and therefore making the insertion of the PAX screw easier for additively manufactured patient-specific implants. The results of the Vickers hardness measurements for AM Ti6Al4V can be seen in Figure 32. The stress relief at 595 °C does not have the desired effect and increases the hardness to 390±5.7 HV and 386.8±5 HV for 2 hours and 4 hours in the furnace, respectively. Mill annealing the sample lowers the hardness of AM Ti6Al4V to 347±5.5 HV. β-annealing with succeeding furnace cooling has the biggest effect and results in a decreased hardness of 315±22.4 HV. However, β-annealing with air cooling leads to a hardness of 339±18.5 HV and water quenching increases the hardness of the Ti6Al4V sample to 358±11.4 HV.

Using different types of heat treatment allowed for a reduction in Vickers hardness. However, comparing the hardness values of the heat treated AM Ti6Al4V samples to the hardness values of the PAX plate still shows a significant discrepancy of at least 110 Vickers. The minimum hardness

of Ti6Al4V after β-annealing and subsequent furnace cool is harder than the PAX screw, leading to the conclusion that utilizing Ti6Al4V for this type of locking system may not be the right material choice. Even though these considerations exist, the insertion of a PAX screw into one of the Ti6Al4V samples is carried out and the results are presented in Chapter 3.4.2 to verify this assumption.
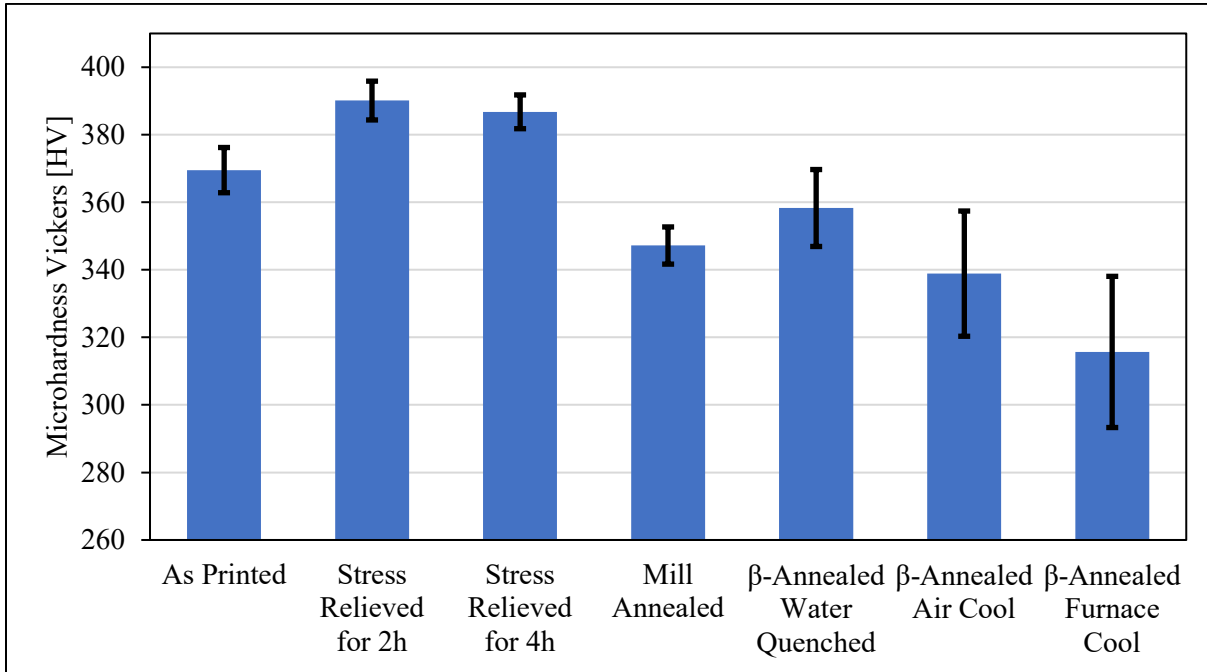
Figure 32: Microhardness (Vickers, 1000g, 30s) of AM Ti6Al4V for different heat treatments.

Because of the high hardness of AM Ti6Al4V, the feasibility of AM 316L stainless steel as a locking plate material is also investigated. Common heat treatments as described in Chapter 2.4 are conducted and the Vickers hardness is measured in parallel ($\parallel$) and perpendicular ($\perp$) direction to the build plate and illustrated in Figure 33. The hardness for as printed 316L is $\perp$ 228.7±7.5 HV and $\parallel$ 212.9±11.1 HV. After stress relieve the $\perp$-hardness is about the same at $\perp$ 227.8±7.5 HV but the $\parallel$-hardness increased to $\parallel$ 235.9±5.8 HV. A hardness decrease to

$\perp$ 186±8.1 HV and $\parallel$ 193.7±5.5 HV is observed after annealing the sample, giving also an indication of a reduction of the anisotropy of the printed parts.
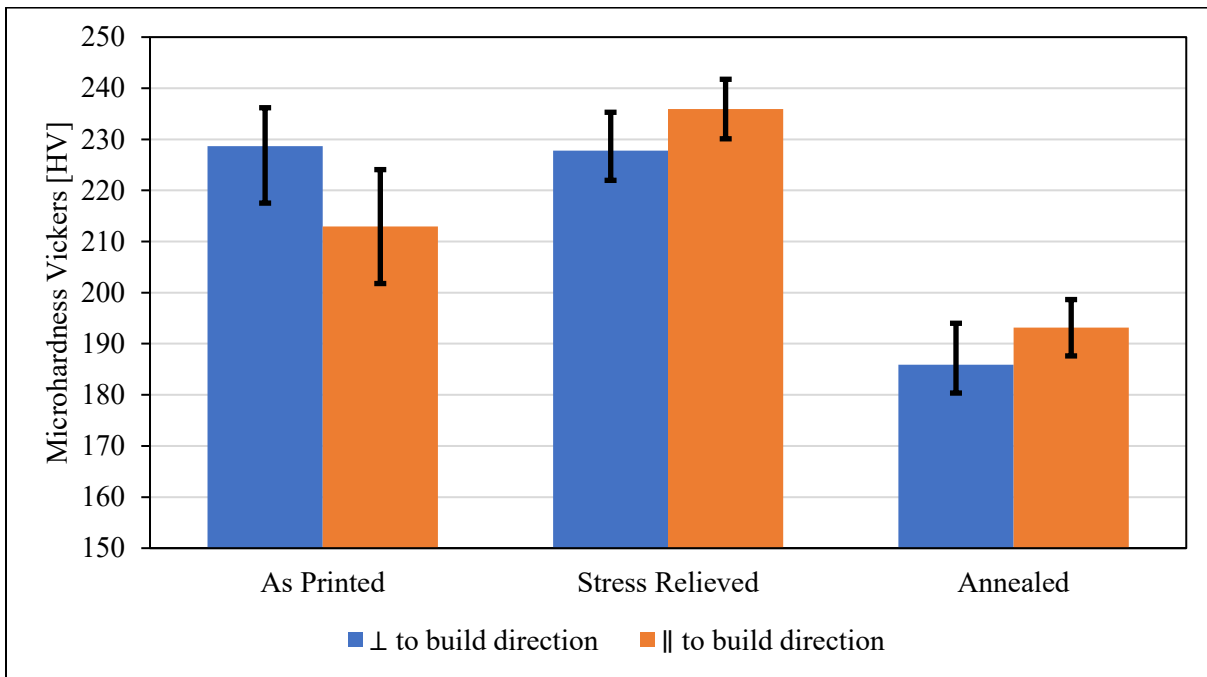
Figure 33: Microhardness (Vickers, 1000g, 30 s) of AM 316L for different heat treatments. Two different orientations were tested: parallel $\parallel$ and perpendicular $\perp$ to the build direction.

When the test results are compared to the as printed samples, the stress relieved does not show a significant change in hardness parallel to the build direction. Conversely, the $\perp$-hardness increased by 23 HV. As described in Chapter 3.2, no change in microstructure is observed for these two samples under OM and XRD. The hardness of the as printed and stress relieved samples are slightly higher than the hardness of the PAX locking plate. Annealing 316L at a higher temperature leads to grain growth within the material, which consumes dislocation pileups at grain boundaries and reduces residual stress [1]. The resulting hardness decreases significantly. The $\perp$-hardness of the annealed sample is about 20 HV and the $\parallel$-hardness is about 12 HV lower than the PAX plate. Because the as printed sample may inherit residual stress that can lead to a distortion

of the part when taken off the build plate [14], only the stress relieved and annealed AM 316L is chosen for the production of the locking system specimen.

3.4   The strength of the AM Locking Systems

The PAX locking system is the reference system and should be seen as the standard to which the printed samples are compared to because it is a commercially available system that is successfully being using during surgery. Therefore, the push-out strengths of the original PAX locking system and the reverse-engineered AM locking systems are presented in this section. The test results of the printed locking plates are revised and suggestions on how and why the AM locking system differs from the PAX locking system are given.
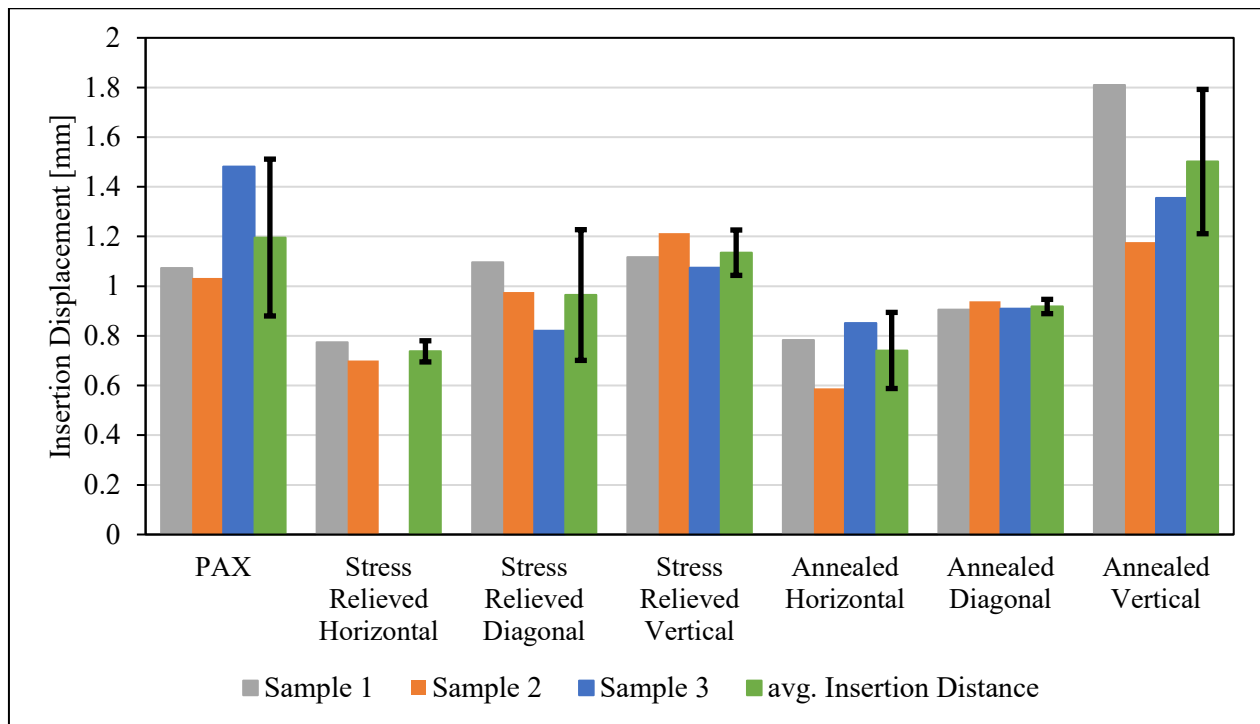
Figure 34: Insertion distance for the PAX and 316L locking plate systems.

3.4.1 PAX Locking System

The screw displacement during insertion is measured as described in Chapter 2.7 and found to be 1.19±0.31 mm as shown in Figure 34. Figure 35 shows the load-extension curves for three locking systems of the original PAX system. The average push-out force required is 1482±53 N. The average extension until failure is 0.49±0.02 mm.
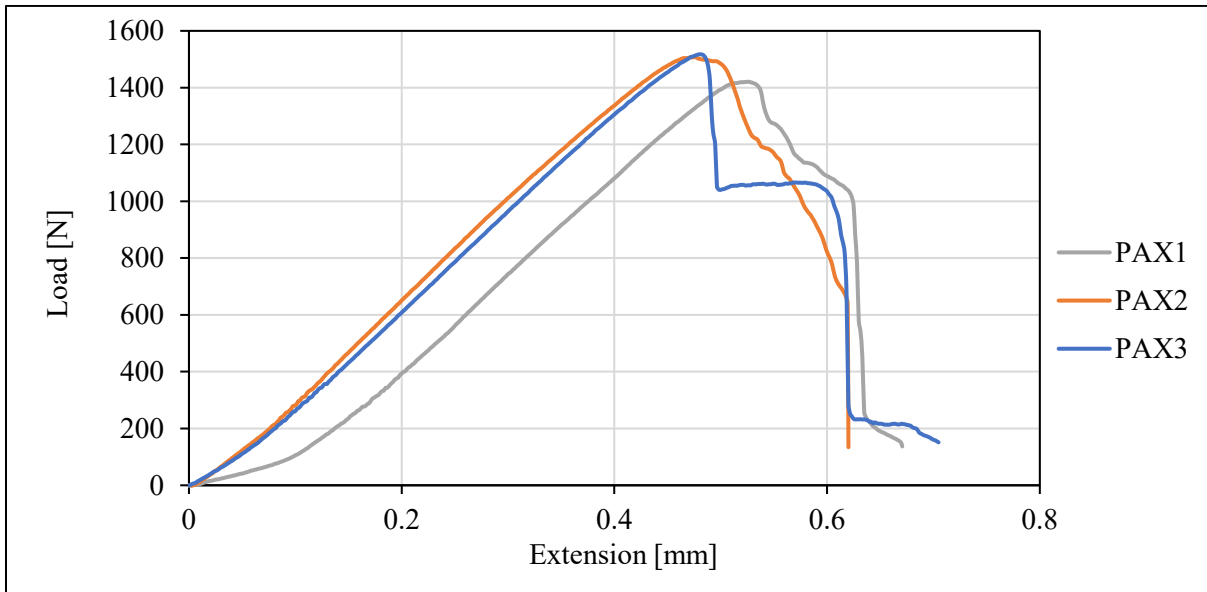
Figure 35: Load-Extension curve for the pull-out test of the PAX locking system.

After failure, the screw heads show little grooves along the head threads where it was in contact with the fins of the screw hole as displayed in Figure 36 (a). However, these grooves are only present on the lower end of the threaded head and do not extend the full length of the threads. The hole has shearing marks on the lower end of the fins. It can clearly be seen where the threads of the screw cut into the material as these marks are slightly deeper than the marks left from the shearing of the screw threads as displayed in Figure 36 (b). Just like the screws, the shearing marks are only present at the lower end of the screw holes, suggesting that the angle of the cone is larger in the plate than it is at the screw head. This is also the reason why the screw can be mounted at multiple angles.
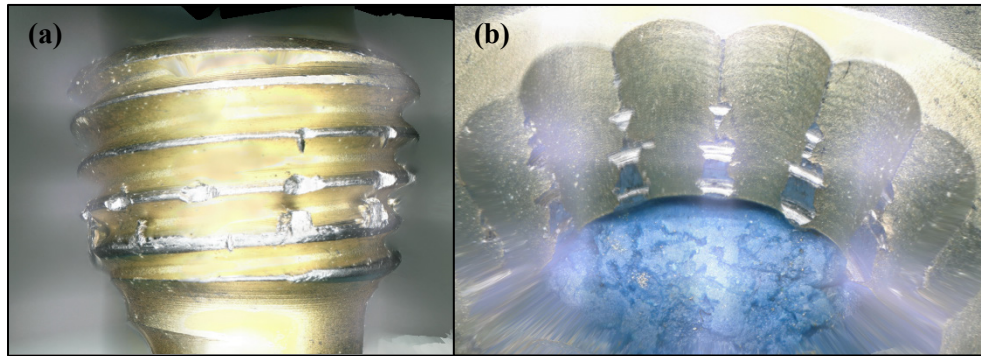
Figure 36: (a) Screw head after insertion into the PAX locking plate showing minor deformation on the thread tips and straight rip outs from where the screw was in contact with the locking plate; (b) PAX locking plate after testing showing cuts from screw insertion and shear from push-out.

3.4.2   AM Ti6Al4V Locking System

A first try of locking the screws into the AM Ti6Al4V locking plate is conducted on the softer β-annealed FC specimen. Upon insertion, the operator noticed the lack of resistance experienced with the PAX locking system. The reason for the lack of resistance is that the threads of the screw are not able to cut into the locking plate and flattened onto the shank of the screw head as seen in Figure 37 (a). The fins of the screw hole in Figure 37 (b), on the other hand, do not show signs of major damage, as there is only little rub off from the oxide formed during heat treatment. The results of the hardness measurements in Chapter 3.3 for the PAX screw and the β-annealed FC Ti6Al4V revealed a higher hardness for the Ti6Al4V specimen. Therefore, the reason why the Ti6Al4V system does not work is a mismatch of the hardness of screw and plate. For further investigations, it is suggested to use a locking plate with a significantly lower hardness than the self-threading screws, i.e. 316L.
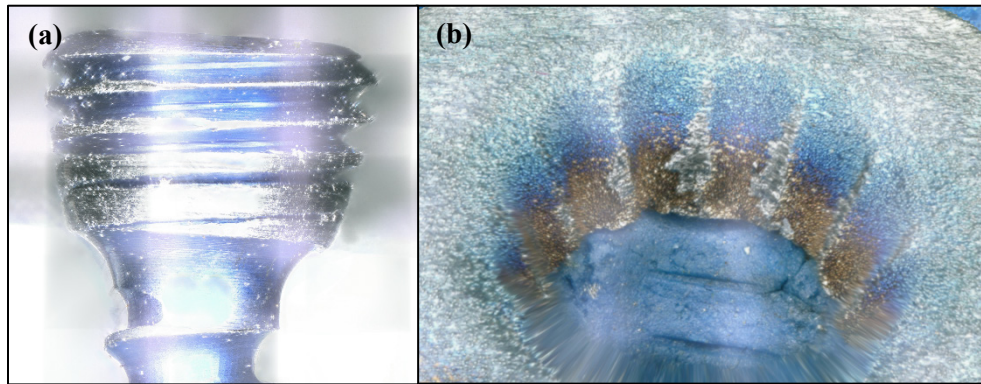
Figure 37: (a) Screw after insertion into the Ti6Al4V locking hole showing major signs of deformation on the threads; (b) locking hole showing minor wear from the insertion of the screw.

3.4.3   AM 316L Locking System

All but one screw are successfully inserted into the stress relieved and the annealed AM 316L samples at varying build orientations successfully. Figure 34 summarizes all insertion distances. The average of the failure push-out force and extension is summarized in Table 9. Figure 39 and Figure 40 show all load to failure vs. extension graphs. The graphs show a constant increase in load until failure, where the load sharply drops. The curves for stress relieved diagonal, annealed horizontal and annealed diagonal have a constant slope until roughly 400 N. At this point the slop becomes steeper until fracture, showing the different plastic and elastic behaviors of the two materials.

Table 9: Push-out Force and Extension at failure for AM 316L locking plates.

	Push-out Force [N]	Extension [mm]
Stress Relieved Horizontal	796±107	0.384±0.005
Stress Relieved Diagonal	1053±126	0.525±0.041
Stress Relieved Vertical	1263±28	0.467±0.039
Annealed Horizontal	1344±73	0.698±0.040
Annealed Diagonal	1247±89	0.608±0.065
Annealed Vertical	1325±132	0.485±0.107

The damage on screw and fins of the locking plate for the horizontal and diagonal samples look similar. An example is shown in Figure 38 (a) and (b). The screw hole shows deeper cuts where the threads touched the fins of the locking hole. Shear marks are present coming off of those marks running to the direction of compression. The top of the locking hole has no damage. Overall, the wear signs look similar to the ones seen in the PAX locking system. The screws, however, lost some of their sharpness on the lower threads and some of the anodizing has come off. There are marks on the threads of the screw head where the fins were in contact. The threads closer to the end of the head do not show any signs of wear.

Sample "Stress Relieved Diagonal 2" is only inserted into the locking system with a maximum torque of 1.7 Nm because the operator noticed a reduction in torque necessary while screwing the screw into the locking plate and stopped the insertion prematurely. Figure 38 (c) and (d) show the failed screw and locking hole. The threads closer to the shank of the screw show a flattening similar to the one observed in screw inserted into the AM Ti6Al4V specimen. In contrast to the screw from Chapter 3.4.2 however, the fins inside the screw hole show cutting marks from the screw as well as shearing. This sample will not be taken into account for further analysis.

However, it has to be mentioned that even though support structures are printed inside the holes to prevent overheating of the area, all of the vertically printed locking plates have sintered on powder and overheating marks on the top side of the hole as seen in Figure 38 (e) and (f). The unwanted material does not seem to be of concern, as similar signs of wear as on the horizontal and diagonal samples is present with the difference of having a wider surface area that is in contact with the screw. Therefore, the cutting and shearing marks appear on a wider area of the sample and not only on the fins of the locking hole.
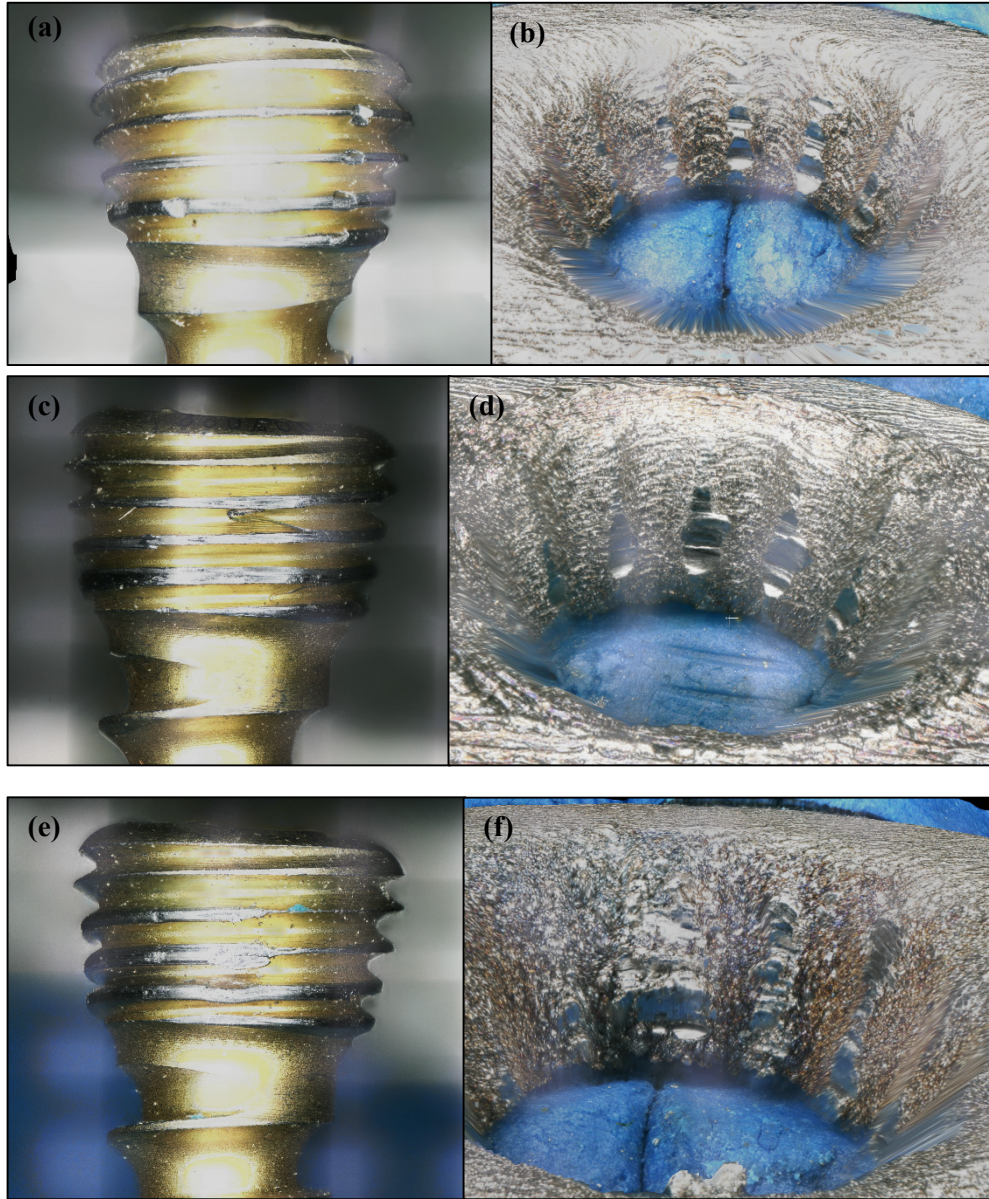
Figure 38: (a) Screw head after insertion in a diagonal 316L locking plate showing a little bit of wear at the thread tips and tear out where the fins of the locking hole were connecting. (b) deep thread cut-ins from screw insertion and tear off wear from the failure of a 316L locking plate. Failed screw (c) and a locking hole (d) after unsuccessful insertion of the screw and push out. This sample failed prematurely. Screw head (e) and a locking hole (f) after insertion and push-out of a vertically printed sample. Pay attention to the big tear away in (e) caused by the roughness of the overheated area.
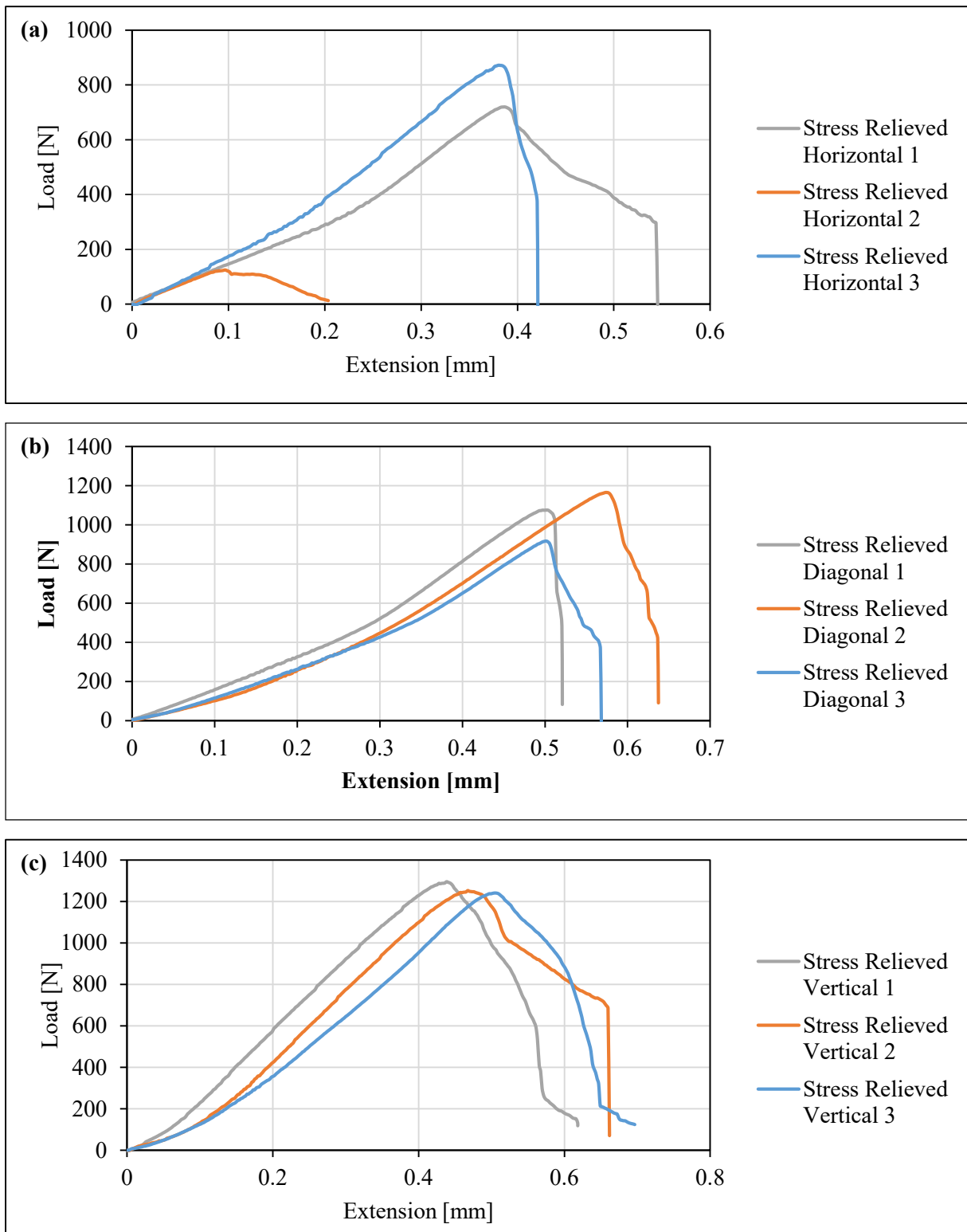
Figure 39: Load-Extension curves AM 316L locking systems after stress relieving printed in (a) horizontal, (b) diagonal and (c) vertical orientation.
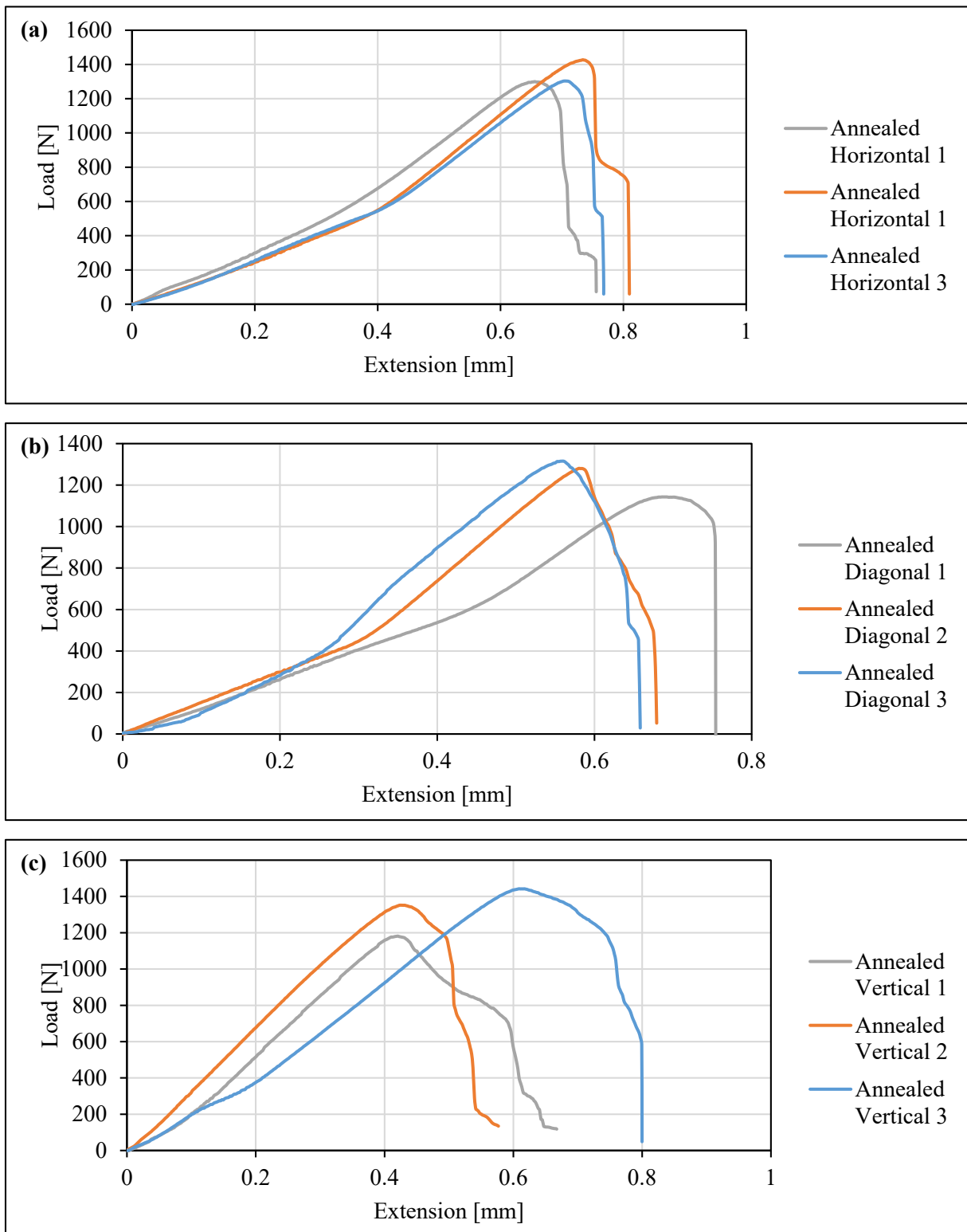
Figure 40: Load-Extension curves AM 316L locking systems after annealing printed in (a) horizontal, (b) diagonal and (c) vertical orientation.

Figure 41 puts the peak load to failure and the extension to failure into context. It can be seen that annealing the additively manufacture locking system has a few advantages over only stress relieving. The lowest strength with the lowest extension to failure is observed for the stress relieved horizontal specimen. Annealing these shows the greatest improvement in strength and extension. The diagonal samples also improved their strength and ductility during annealing, however not to the extent of the horizontal specimen. The vertical specimen have roughly the same strength and extension to failure. The overall strongest locking plate with the least amount of spread is the PAX system.
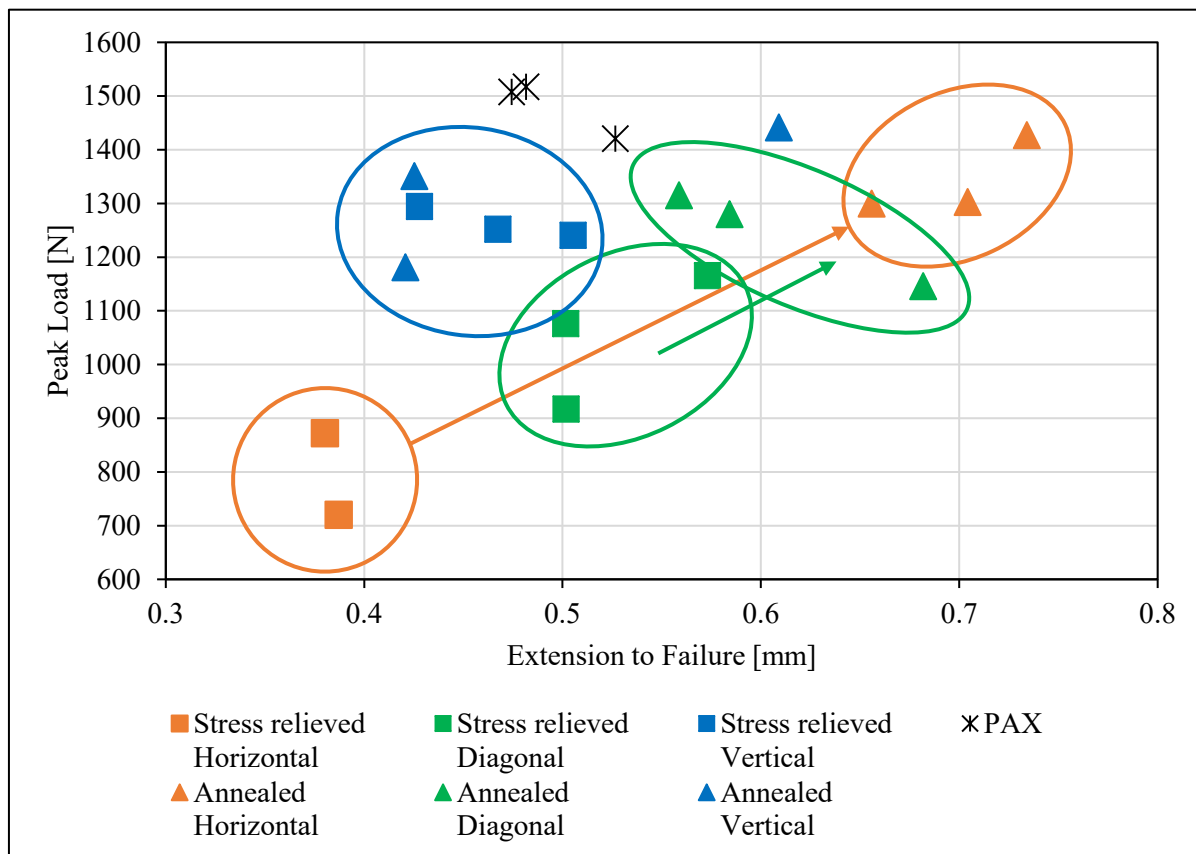
Figure 41: Averaged extension to failure and peak load of all tested 316L specimen. Orientations are colored in one color while the heat treatment can be distinguished by its shape. The PAX system is displayed as black stars.

Two distinctive features can be observed from the comparison between the samples. First, the annealing reduced the negative influence of the build orientation, making the peak load to failure of the AM locking plates more uniform throughout their different orientations. It is assumed that the growth of grains in the microstructure reduced the anisotropy of the material. An indication for this is also the reduction of the gap between the hardness measurements parallel and perpendicular to the build direction. Secondly, annealing allows for a higher extension to failure, making the locking system more flexible and stronger due to its ability to absorb more energy before fracture. However, anisotropy can be found in the extension to failure, where the vertical specimen would fail earlier than the diagonal or horizontal specimen.

To investigate the influence of the hardness on the strength of the locking systems, Figure 42 is created. It shows the peak load to failure vs. extension to failure, where the hardness of the specimen is taken into account. The mean from the horizontal and the vertical has been taken as the hardness for the diagonal samples. Here, a shift from lower peak load and extension towards higher load tolerance and extension becomes even more apparent, thus leading to the assumption that a decrease in hardness is beneficial for the performance of the locking system. A further improvement of the system may be achieved by selecting a material with low hardness but high strength.
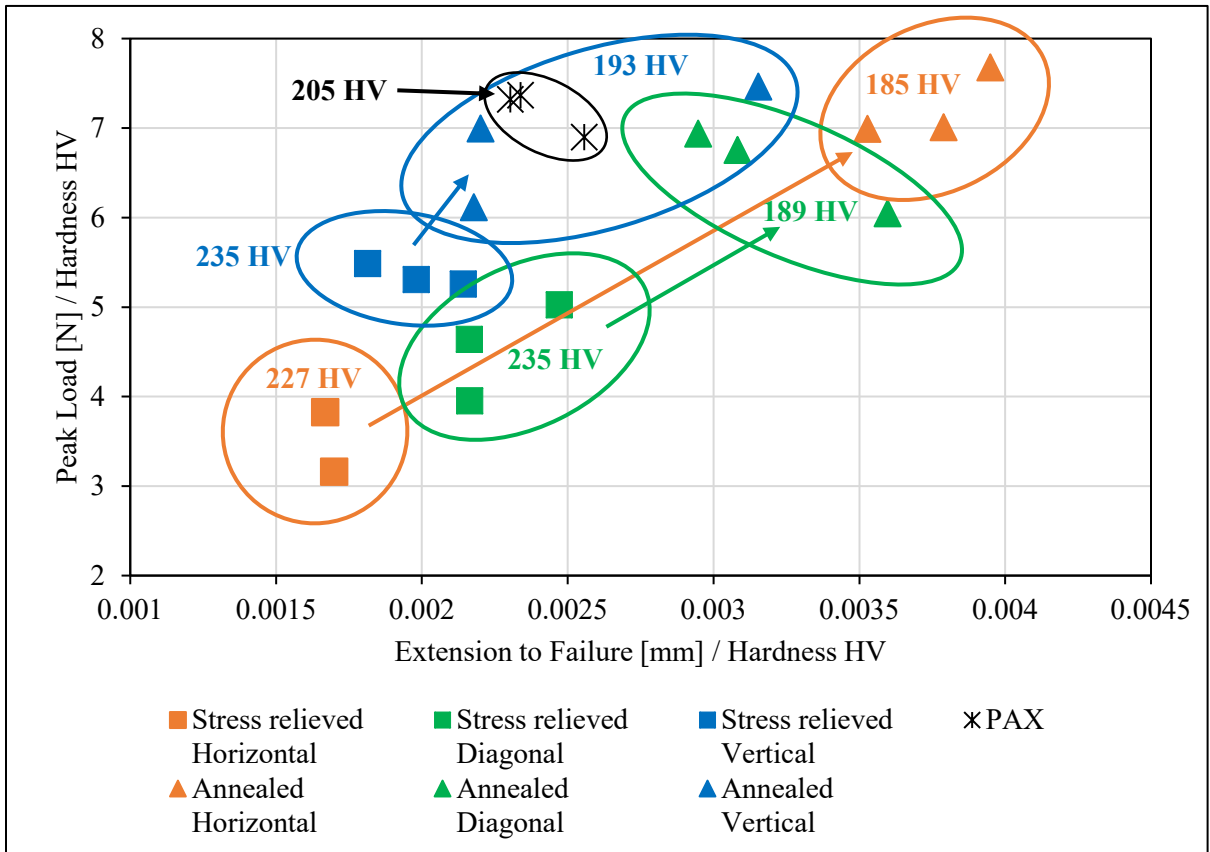
Figure 42: Averaged extension to failure and peak loads independent of the hardness of all tested 316L specimen. The hardness of each specimen set is marked accordingly. Part orientations are displayed in one color while the heat treatment can be distinguished by the shape. The PAX system is displayed as black stars.

Chapter 4:   Conclusion

In this work, AM was successfully utilized for the creation of a locking system for orthopedic implants. Locking systems can reduce the risk of bone porosis during bone healing because they don't harm the cardiovascular system of the bone. The PAX advanced locking system was chosen because of its simple geometric design and ability to insert screws at different angles during surgery.

A parameter study for Ti6Al4V titanium and 316L stainless steel was performed to ensure the manufacture of high-density parts with good surface finishes. Different types of heat treatment were conducted to receive microstructure and mechanical properties that would the system to work. XCT was used to receive a digital file of the locking system and print specimen in Ti6Al4V and 316L. The specimen was heat treated at relevant temperatures. The Ti6Al4V locking plate did not work because its high hardness did not allow the threads of the screw to cut into the material. However, it was found that screw could be inserted into the 316L locking plates without the need of post-processing after the heat treatment.

The screws were pushed out of the plate by applying a linear load concentrically on the screw until the fracture occurs. The load vs. extension curves were recorded and it was found that annealing offered higher and more consistent strength because of its lower hardness that allowed the screws to be inserted with less damage to the threads. Furthermore, the stress relieved samples showed a lower strength in the horizontal and diagonal position. After annealing, the samples did not show a dependency on build orientation anymore. It is assumed that this behavior is made possible by the lack of anisotropy in the annealed samples.

In summary, it was shown, that it is possible to manufacture the PAX locking system additively. However, annealing is necessary for the system to inherit enough strength all build orientations. This allows for the implementation of locking screws into patient-specific implants without the need for expensive and time-consuming machining.

Chapter 5:   References

[1]   T. DebRoy *et al.*, "Additive manufacturing of metallic components – Process, structure and properties," *Progress in Materials Science,* vol. 92, pp. 112-224, 2018/03/01/ 2018.

[2]   W. Gao *et al.*, "The status, challenges, and future of additive manufacturing in engineering," *Computer-Aided Design,* vol. 69, pp. 65-89, 2015.

[3]   R. Poprawe, C. Hinke, W. Meiners, J. Schrage, S. Bremen, and S. Merkt, "SLM production systems: recent developments in process development, machine concepts and component design," in *Advances in Production Technology*: Springer, 2015, pp. 49-65.

[4]   S. M. Thompson, L. Bian, N. Shamsaei, and A. J. A. M. Yadollahi, "An overview of Direct Laser Deposition for additive manufacturing; Part I: Transport phenomena, modeling and diagnostics," *Additive Manufacturing,* vol. 8, pp. 36-62, 2015.

[5]   W. E. Frazier, "Metal Additive Manufacturing: A Review," *Journal of Materials Engineering and Performance,* vol. 23, no. 6, pp. 1917-1928, 2014/06/01 2014.

[6]   K. Karunakaran, A. Bernard, S. Suryakumar, L. Dembinski, and G. J. R. P. J. Taillandier, "Rapid manufacturing of metallic objects," *Rapid Prototyping Journal,* vol. 18, no. 4, pp. 264-280, 2012.

[7]   S. Moylan, J. Slotwinski, A. Cooke, K. Jurrens, and M. A. Donmez, "Proposal for a standardized test artifact for additive manufacturing machines and processes," in *Proceedings of the 2012 annual international solid freeform fabrication symposium*, 2012: Austin, TX, pp. 6-8.

[8]   S. Moylan, J. Slotwinski, A. Cooke, K. Jurrens, M. A. J. J. o. r. o. t. N. I. o. S. Donmez, and Technology, "An Additive Manufacturing Test Artifact," *Journal of Research of the National Institute of Standards and Technology,* vol. 119, p. 429, 2014.

[9]   R. E. Blose, B. H. Walker, R. M. Walker, and S. H. Froes, "New opportunities to use cold spray process for applying additive features to titanium alloys," *Metal Powder Report,* vol. 61, no. 9, pp. 30-37, 2006/10/01/ 2006.

[10]   M. Cotteleer and J. J. D. R. Joyce, "3D opportunity: Additive manufacturing paths to performance, innovation, and growth," *Deloitte Review,* vol. 14, pp. 5-19, 2014.

[11]   *Standard terminology for additive manufacturing technologies*, ASTM International 2013; F2792-12a.

[12]   W. Meiners, *Direktes Selektives Laser Sintern einkomponentiger metallischer Werkstoffe.* Aachen: Shaker Verlag GmbH, 1999.

[13]   T. D. Ngo, A. Kashani, G. Imbalzano, K. T. Q. Nguyen, and D. Hui, "Additive manufacturing (3D printing): A review of materials, methods, applications and challenges," *Composites Part B: Engineering,* vol. 143, pp. 172-196, 2018/06/15/ 2018.

[14]   F. A. List, S. Pannala, R. R. Dehoff, and S. S. Babu, "The metallurgy and processing science of metal additive manufacturing AU - Sames, W. J," *International Materials Reviews,* vol. 61, no. 5, pp. 315-360, 2016/07/03 2016.

[15]   H. Galarraga, R. J. Warren, D. A. Lados, R. R. Dehoff, M. M. Kirka, and P. Nandwana, "Effects of heat treatments on microstructure and properties of Ti-6Al-4V ELI alloy fabricated by electron beam melting (EBM)," *Materials Science and Engineering: A,* vol. 685, pp. 417-428, 2017/02/08/ 2017.

[16]   A. Mostafaei, E. L. Stevens, E. T. Hughes, S. D. Biery, C. Hilla, and M. Chmielus, "Powder bed binder jet printed alloy 625: Densification, microstructure and mechanical properties," *Materials & Design,* vol. 108, pp. 126-135, 2016/10/15/ 2016.

[17]   W. J. Sames, F. A. List, S. Pannala, R. R. Dehoff, and S. S. Babu, "The metallurgy and processing science of metal additive manufacturing," *International Materials Reviews,* vol. 61, no. 5, pp. 315-360, 2016/07/03 2016.

[18]   S. Pal, G. Lojen, V. Kokol, and I. Drstvensek, "Evolution of metallurgical properties of Ti-6Al-4V alloy fabricated in different energy densities in the Selective Laser Melting technique," *Journal of Manufacturing Processes,* vol. 35, pp. 538-546, 2018/10/01/ 2018.

[19]   T. Simson, A. Emmel, A. Dwars, and J. Böhm, "Residual stress measurements on AISI 316L samples manufactured by selective laser melting," *Additive Manufacturing,* vol. 17, pp. 183-189, 2017/10/01/ 2017.

[20]   W. Xu *et al.*, "Additive manufacturing of strong and ductile Ti–6Al–4V by selective laser melting via in situ martensite decomposition," *Acta Materialia,* vol. 85, pp. 74-84, 2015/02/15/ 2015.

[21]   M. Wang *et al.*, "Fabrication and characterization of selective laser melting printed Ti–6Al–4V alloys subjected to heat treatment for customized implants design," *Progress in Natural Science: Materials International,* vol. 26, no. 6, pp. 671-677, 2016/12/01/ 2016.

[22]   H. Qi, M. Azer, and A. Ritter, "Studies of Standard Heat Treatment Effects on Microstructure and Mechanical Properties of Laser Net Shape Manufactured INCONEL 718," *Metallurgical and Materials Transactions A,* vol. 40, no. 10, pp. 2410-2422, 2009/10/01 2009.

[23] T. Mukherjee, J. Zuback, A. De, and T. J. S. r. DebRoy, "Printability of alloys for additive manufacturing," vol. 6, p. 19717, 2016.

[24] E. O. Olakanmi, R. F. Cochrane, and K. W. Dalgarno, "Densification mechanism and microstructural evolution in selective laser sintering of Al–12Si powders," *Journal of Materials Processing Technology,* vol. 211, no. 1, pp. 113-121, 2011/01/01/ 2011.

[25] W. E. King *et al.*, "Observation of keyhole-mode laser melting in laser powder-bed fusion additive manufacturing," *Journal of Materials Processing Technology,* vol. 214, no. 12, pp. 2915-2925, 2014/12/01/ 2014.

[26] K. Darvish, Z. W. Chen, and T. Pasang, "Reducing lack of fusion during selective laser melting of CoCrMo alloy: Effect of laser power on geometrical features of tracks," *Materials & Design,* vol. 112, pp. 357-366, 2016/12/15/ 2016.

[27] M. Svensson, U. Ackelid, and A. Ab, "Titanium alloys manufactured with electron beam melting mechanical and chemical properties," in *Proceedings of the materials and processes for medical devices conference*, 2010: ASM International, pp. 189-194.

[28] D. Bäuerle, *Laser processing and chemistry*. Springer Science & Business Media, 2013.

[29] K. Mumtaz and N. Hopkinson, "Top surface and side roughness of Inconel 625 parts processed using selective laser melting," vol. 15, no. 2, pp. 96-103, 2009.

[30] S. L. Sing, J. An, W. Y. Yeong, and F. E. Wiria, "Laser and electron-beam powder-bed additive manufacturing of metallic implants: A review on processes, materials and designs," *Journal of Orthopaedic Research,* vol. 34, no. 3, pp. 369-385, 2016.

[31] A. Yadollahi, N. Shamsaei, S. M. Thompson, and D. W. Seely, "Effects of process time interval and heat treatment on the mechanical and microstructural properties of direct laser

deposited 316L stainless steel," *Materials Science and Engineering: A,* vol. 644, pp. 171-183, 2015/09/17/ 2015.

[32] H. D. Carlton, A. Haboub, G. F. Gallegos, D. Y. Parkinson, and A. A. MacDowell, "Damage evolution and failure mechanisms in additively manufactured stainless steel," *Materials Science and Engineering: A,* vol. 651, pp. 406-414, 2016/01/10/ 2016.

[33] F. Cverna, *Worldwide guide to equivalent nonferrous metals and alloys*. ASM International, 2001.

[34] D. Kianersi, A. Mostafaei, and A. A. Amadeh, "Resistance spot welding joints of AISI 316L austenitic stainless steel sheets: Phase transformations, mechanical properties and microstructure characterizations," *Materials & Design,* vol. 61, pp. 251-263, 2014.

[35] J. Cordero, L. Munuera, and M. Folgueira, "Influence of metal implants on infection. An experimental study in rabbits," *The Journal of bone and joint surgery. British volume,* vol. 76, no. 5, pp. 717-720, 1994.

[36] F. Schmidt and R. Wood, "Heat treatment of titanium and titanium alloys," 1966.

[37] E. Sallica-Leva, R. Caram, A. L. Jardini, and J. B. Fogagnolo, "Ductility improvement due to martensite α′ decomposition in porous Ti–6Al–4V parts produced by selective laser melting for orthopedic implants," *Journal of the Mechanical Behavior of Biomedical Materials,* vol. 54, pp. 149-158, 2016/02/01/ 2016.

[38] M. J. Donachie, *Titanium: a technical guide*. ASM international, 2000.

[39] J. Sieniawski, W. Ziaja, K. Kubiak, and M. Motyk, "Microstructure and Mechanical Properties of High Strength Two-Phase Titanium Alloys," in *Titanium Alloys - Advances in Properties Control*, 2013.

[40]   M. D. Barnhart and K. C. Maritato, *Locking Plates in Veterinary Orthopedics*. John Wiley & Sons, 2018.

[41]   J. G. G. Dobbe, J. C. Vroemen, S. D. Strackee, and G. J. Streekstra, "Patient-specific distal radius locking plate for fixation and accurate 3D positioning in corrective osteotomy," *Strategies in Trauma and Limb Reconstruction,* vol. 9, no. 3, pp. 179-183, 2014/11/01 2014.

[42]   K. C. Wong, S. M. Kumta, N. V. Geel, and J. Demol, "One-step reconstruction with a 3D-printed, biomechanically evaluated custom implant after complex pelvic tumor resection," *Computer Aided Surgery,* vol. 20, no. 1, pp. 14-23, 2015/01/02 2015.

[43]   H. Rotaru, R. Schumacher, S.-G. Kim, and C. Dinu, "Selective laser melted titanium implants: a new technique for the reconstruction of extensive zygomatic complex defects," *Maxillofacial Plastic and Reconstructive Surgery,* vol. 37, no. 1, p. 1, 2015/01/29 2015.

[44]   O. L. A. Harrysson, O. Cansizoglu, D. J. Marcellin-Little, D. R. Cormier, and H. A. West, "Direct metal fabrication of titanium implants with tailored materials and mechanical properties using electron beam melting technology," *Materials Science and Engineering: C,* vol. 28, no. 3, pp. 366-373, 2008/04/01/ 2008.

[45]   M. Di Prima, J. Coburn, D. Hwang, J. Kelly, A. Khairuzzaman, and L. J. D. p. i. m. Ricles, "Additively manufactured medical products–the FDA perspective," vol. 2, no. 1, p. 1, 2015.

[46]   R. J. Morrison *et al.*, "Regulatory considerations in the design and manufacturing of implantable 3D-printed medical devices," *Clinical and translational science,* vol. 8, no. 5, pp. 594-600, 2015.

[47]   S. Tepic, A. R. Remiger, K. Morikawa, M. Predieri, and S. M. Perren, "Strength recovery in fractured sheep tibia treated with a plate or an internal fixator: an experimental study with a two-year follow-up," *Journal of orthopaedic trauma,* vol. 11, no. 1, pp. 14-23, 1997.

[48] E. Gautier, B. A. Rahn, and S. M. Perren, "Vascular remodelling," *Injury,* vol. 26, pp. B11-B19, 1995/01/01/ 1995.

[49] O. Grundnes and O. Reikerås, "Blood flow and mechanical properties of healing bone," *Acta Orthopaedica Scandinavica,* vol. 63, no. 5, pp. 487-491, 1992/01/01 1992.

[50] B. Boudreau, J. Benamou, D. J. von Pfeil, R. P. Guillou, C. Beckett, and L. M. Déjardin, "Effect of screw insertion torque on mechanical properties of four locking systems," *Veterinary Surgery,* vol. 42, no. 5, pp. 535-543, 2013.

[51] A. B. Baroncelli, U. Reif, C. Bignardi, and B. Peirone, "Effect of screw insertion torque on push-out and cantilever bending properties of five different angle-stable systems," *Veterinary Surgery,* vol. 42, no. 3, pp. 308-315, 2013.

[52] T. G. Guerrero, K. Kalchofner, N. Scherrer, and P. Kircher, "The Advanced Locking Plate System (ALPS): A Retrospective Evaluation in 71 Small Animal Patients," *Veterinary Surgery,* vol. 43, no. 2, pp. 127-135, 2014/02/01 2014.

[53] DePuy Synthes. (2016, January 15, 2019, March 03). *LCP Locking Compression Plate* [Online]. Available: https://emea.depuysynthes.com/hcp/trauma/products/qs/lcp-locking-compression-plate.

[54] B. Bufkin, M. Barnhart, A. Kazanovicz, S. Naber, and S. Kennedy, "The effect of screw angulation and insertion torque on the push-out strength of polyaxial locking screws and the single cycle to failure in bending of polyaxial locking plates," *Veterinary and Comparative Orthopaedics and Traumatology,* vol. 26, no. 03, pp. 186-191, 2013.

[55] Orthomed. (2019, 03/27/2019). *SOP™ The original & best locking plate system using standard cortical screws* [Online]. Available: https://www.orthomed.co.uk/us/systems/sop-interlocking-plate-fracture-repair-system/.

[56]   C. Laser. (2018, 03/25/2019). *Mlab cusing R Metal laser melting system* [Online]. Available: https://www.concept-laser.de/en/products/machines.html.

[57]   S. P. Moylan, J. A. Slotwinski, A. Cooke, K. Jurrens, and M. A. Donmez, "Lessons learned in establishing the NIST metal additive manufacturing laboratory," *NIST Technical Note,* 2013.

[58]   B. Wysocki, P. Maj, R. Sitek, J. Buhagiar, K. J. Kurzydłowski, and W. Święszkowski, *Laser and Electron Beam Additive Manufacturing Methods of Fabricating Titanium Bone Implants*. 2017, p. 657.

[59]   J. Yan, Y. Zhou, R. Gu, X. Zhang, W.-M. Quach, and M. Yan, "A Comprehensive Study of Steel Powders (316L, H13, P20 and 18Ni300) for Their Selective Laser Melting Additive Manufacturing," *Metals,* vol. 9, no. 1, p. 86, 2019.

[60]   K. Saeidi, X. Gao, F. Lofaj, L. Kvetková, and Z. J. Shen, "Transformation of austenite to duplex austenite-ferrite assembly in annealed stainless steel 316L consolidated by laser melting," *Journal of Alloys and Compounds,* vol. 633, pp. 463-469, 2015.

[61]   M. S. Pham, B. Dovgyy, and P. A. Hooper, "Twinning induced plasticity in austenitic stainless steel 316L made by additive manufacturing," *Materials Science and Engineering: A,* vol. 704, pp. 102-111, 2017/09/17/ 2017.

[62]   S. Q. Wu *et al.*, "Microstructural evolution and microhardness of a selective-laser-melted Ti–6Al–4V alloy after post heat treatments," *Journal of Alloys and Compounds,* vol. 672, pp. 643-652, 2016/07/05/ 2016.

[63]   F. Calignano, D. Manfredi, E. Ambrosio, L. Iuliano, and P. Fino, "Influence of process parameters on surface roughness of aluminum parts produced by DMLS," *The International Journal of Advanced Manufacturing Technology,* vol. 67, no. 9-12, pp. 2743-2751, 2013.

[64] A. Riemer, S. Leuders, M. Thöne, H. A. Richard, T. Tröster, and T. Niendorf, "On the fatigue crack growth behavior in 316L stainless steel manufactured by selective laser melting," *Engineering Fracture Mechanics,* vol. 120, pp. 15-25, 2014/04/01/ 2014.

[65] M. Montero Sistiaga, S. Nardone, C. Hautfenne, and J. Van Humbeeck, "Effect of heat treatment of 316L stainless steel produced by selective laser melting (SLM)," in *Proceedings of the 27th Annual International Solid Freeform Fabrication Symposium-An Additive Manufacturing Conference*, 2016, pp. 558-565.

[66] D. Tabor, *The hardness of metals*. Oxford university press, 2000.

[67] P. X.-R. Solutions. (2019, 03/26/2019). *Benchmark 225/60* [Online]. Available: http://www.pxsinc.com/Systems/Benchmark22560.aspx.

Appendix A: Test Report for Ti6Al4V Titanium Powder provided by Concept Laser

CONCEPTLASER

Test Report

Lichtenfels, July 26, 2017

We hereby confirm that the metal powder CL 41Ti, batch no. UK81646, has been checked and approved by CL in terms of grain size and grain shape and chemical composition as specified below.

As part of this, the metal powder was subjected to analysis applying the relevant quality standards.

In this case the metal powder was subjected to the analysis in accordance with the valid quality standards. The material was analysed and checked by an external and independent testing laboratory for chemical analysis. The laboratory is certified with the test seal of the German Accreditation System.

Results from the following table are based on „ASTM F136 -02a".

Chem. Element	Target (Min.) in %	Result in %, Sample 1	Result in %, Sample 2	Target (Max.) in %
Al	5,50	6,33	6,21	6,50
C	0,0	0,011	0,010	0,08
Fe	0,0	0,170	0,180	0,25
H	0,0	0,0022	0,0024	0,012
N	0,0	0,002	0,002	0,05
O	0,0	0,091	0,088	0,13
Ti	Rest	Rest	Rest	Rest
V	3,5	3,98	3,95	4,50

Concept Laser GmbH

sgd. Sven Dilzer
Quality Department

QM powder

Prüfbericht

Auftragsnummer: 17-02476   **Dokumenten-Nr.:** 17-02476-a

Auftraggeber: CONCEPT Laser GmbH
An der Zeil 8
DE-96215 Lichtenfels

Bestellnr./Betreff: EB 14390

rl-Bearbeiter: Stefan Frieg   **Eingangsdatum:** 13.07.2017
Untersuchungsende: 25.07.2017

Probennummer: 17-02476-001
Probenbezeichnung: CL 41, Chg.: UK81646
Material: Pulver

Probennummer: 17-02476-002
Probenbezeichnung: CL 41, Chg.: UK81646
Material: Pulver

1   Einleitung und Problemstellung

Gegenstand der Untersuchungen sind die vom Auftraggeber zur Verfügung gestellten Proben mit den o.g. Bezeichnungen. Ziel der Untersuchungen ist die Bestimmung der chemischen Zusammensetzung und lichtmikroskopische Betrachtung der Proben sowie die Partikelgrößenanalyse und die Bestimmung der Korngrößenverteilung der Probe 17-02476-001.

2   Durchgeführte Untersuchungen

Die chemische Zusammensetzung der Proben wurde mittels Röntgenfluoreszenzanalyse (RFA), mittels Verbrennungsanalyse (Kohlenstoff) und mittels Trägergasheißextraktion (Sauerstoff, Stickstoff und Wasserstoff) bestimmt. Des Weiteren wurden von der Probe 17-02476-001 die Korngrößenverteilung mittels Siebanalyse und die Partikelgrößenanalyse mittels Laserbeugung untersucht. Zusätzlich wurde von der Probe der Trockenverlust gravimetrisch bestimmt. Anschließend wurden die Proben lichtmikroskopisch betrachtet.

Methode	Norm
Röntgenfluoreszenzanalyse (RFA)	Akkreditierte Hausmethode QMA R13A131:2012-06 (RFA-Borat-Aufschluss)
Verbrennungsanalyse	Akkreditiertes Verfahren nach ASTM E1941:2010-12
Trägergasheißextraktion (O,N)	Akkreditiertes Verfahren nach ASTM E1409:2013-10
Trägergasheißextraktion (H)	Akkreditiertes Verfahren nach ASTM E1447:2009-03
Partikelgrößenanalyse mittels Laserbeugung[1]	Hausmethode
Siebanalyse	Hausmethode
Trockenverlust (TV)	Akkreditierte Hausmethode QMA S13A162:2012-06
Lichtmikroskopie	Hausmethode

1) Die Bestimmung erfolgte durch einen gemäß DIN EN ISO/IEC 17025 akkreditierten Unterauftragnehmer.

3 Ergebnisse

3.1. Werkstoffanalyse

Die Ergebnisse der Werkstoffanalyse sind in den Tabellen 1 und 2 aufgeführt.

Tabelle 1: Ergebnisse der RFA, Verbrennungsanalyse, Trägergasheißextraktion und TV

Proben-Nr.	17-02476-001
Proben-Bezeichnung	CL 41, Chg.: UK81646

Prüfung	Einheit	Ergebnis
Ti	Mass.-%	Basis
Al	Mass.-%	6,33
Fe	Mass.-%	0,17
V	Mass.-%	3,98
C	Mass.-%	0,011
O	Mass.-%	0,091
N	Mass.-%	0,002
H	Mass.-%	0,0022
Trockenverlust 105 °C	Mass.-%	<0,01

Tabelle 2: Ergebnisse der RFA, Verbrennungsanalyse, Trägergasheißextraktion

Proben-Nr.	17-02476-002
Proben-Bezeichnung	CL 41, Chg.: UK81646

Prüfung	Einheit	Ergebnis
Ti	Mass.-%	Basis
Al	Mass.-%	6,21
Fe	Mass.-%	0,18
V	Mass.-%	3,95
C	Mass.-%	0,010
O	Mass.-%	0,088
N	Mass.-%	0,002
H	Mass.-%	0,0024

3.2. Partikelanalyse mittels Laserbeugung

Die Korngrößenverteilung der Probe wurde in Doppelbestimmung mittels Laserbeugung ermittelt. Dispergiermedium war Wasser. Die Ergebnisse (Mittelwerte) sind in der folgenden Tabelle 3 sowie in den Diagramm 1 dargestellt.

Tabelle 3: Ergebnisse der Korngrößenverteilung der Probe „CL 41, Chg.: UK81646"

Proben-Nr.	17-02476-001
Bezeichnung	CL 41, Chg.: UK81646

Prüfung	Einheit	Ergebnis
Dv (10)	µm	22,675
Dv (50)	µm	33,295
Dv (90)	µm	48,476
Breite (90;10)		0,775
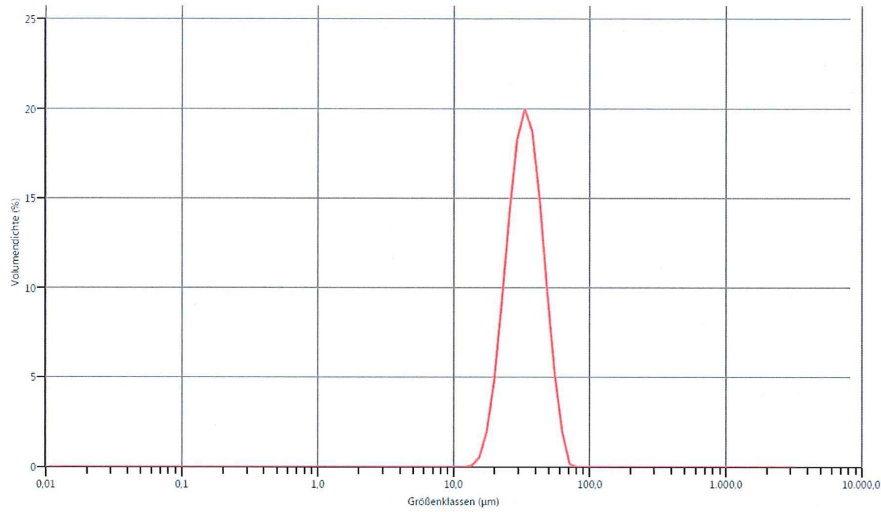
rev**ierlabor**
revierlabor GmbH • Westendhof 17 • 45143 Essen • Telefon: (0201) 87421-0 • Telefax: (0201) 87421-19
Eine nur auszugsweise Vervielfältigung des Prüfberichtes ist nur mit schriftlicher Zustimmung von revierlabor gestattet.

Dok. Nr.: 17-02476-a   Seite 2 von 6

84

Ergebnis									
Größe (µm)	% Volumen Über	Größe (µm)	% Volumen Über	Größe (µm)	% Volumen Über	Größe (µm)	% Volumen Über	Größe (µm)	% Volumen Über
0,010	100,00	0,166	100,00	2,750	100,00	45,613	13,88	756,449	0,00
0,011	100,00	0,188	100,00	3,125	100,00	51,823	5,75	859,450	0,00
0,013	100,00	0,214	100,00	3,550	100,00	58,880	1,56	976,475	0,00
0,015	100,00	0,243	100,00	4,034	100,00	66,897	0,01	1109,435	0,00
0,017	100,00	0,276	100,00	4,583	100,00	76,006	0,00	1260,499	0,00
0,019	100,00	0,314	100,00	5,207	100,00	86,355	0,00	1432,133	0,00
0,022	100,00	0,357	100,00	5,916	100,00	98,114	0,00	1627,136	0,00
0,024	100,00	0,405	100,00	6,722	100,00	111,473	0,00	1848,692	0,00
0,028	100,00	0,460	100,00	7,637	100,00	126,652	0,00	2100,416	0,00
0,032	100,00	0,523	100,00	8,677	100,00	143,897	0,00	2386,415	0,00
0,036	100,00	0,594	100,00	9,858	100,00	163,490	0,00	2711,357	0,00
0,041	100,00	0,675	100,00	11,201	100,00	185,752	0,00	3080,544	0,00
0,046	100,00	0,767	100,00	12,726	100,00	211,044	0,00	3500,000	0,00
0,053	100,00	0,872	100,00	14,458	99,96	239,780	0,00		
0,060	100,00	0,991	100,00	16,427	99,59	272,430	0,00		
0,068	100,00	1,125	100,00	18,664	98,04	309,525	0,00		
0,077	100,00	1,279	100,00	21,205	94,04	351,670	0,00		
0,088	100,00	1,453	100,00	24,092	86,34	399,555	0,00		
0,100	100,00	1,651	100,00	27,373	74,42	453,960	0,00		
0,113	100,00	1,875	100,00	31,100	59,02	515,772	0,00		
0,128	100,00	2,131	100,00	35,335	42,13	586,001	0,00		
0,146	100,00	2,421	100,00	40,146	26,35	665,793	0,00		

Diagramm 1: Ergebnisse der Korngrößenverteilung der Probe „CL 41, Chg.: UK81646"

3.3. Siebanalyse

Die Probe wurde über 100 µm-, 80 µm-, 63 µm-, 45 µm- ,32 µm- und 20 µm Siebe gesiebt.

Die Ergebnisse sind in der Tabelle 4 und in dem Diagramm 2 dargestellt.

re✓**ierlabor**
revierlabor GmbH • Westendhof 17 • 45143 Essen • Telefon: (0201) 87421-0 • Telefax: (0201) 87421-19
Eine nur auszugsweise Vervielfältigung des Prüfberichtes ist nur mit schriftlicher Zustimmung von revierlabor gestattet.

Dok. Nr.: 17-02476-a   Seite 3 von 6

85

Tabelle 4: Ergebnisse der Siebanalyse der Probe „CL 41, Chg.: UK81646"

Proben-Nr.		17-02476-001
Bezeichnung		CL 41, Chg.: UK81646
Korngröße	Einheit	Ergebnis
< 100 µm	%	100
< 80 µm	%	99,89
< 63 µm	%	99,76
< 45 µm	%	94,34
< 32 µm	%	41,73
< 20 µm	%	3,68

Korngrößenverteilung mit Siebanalyse
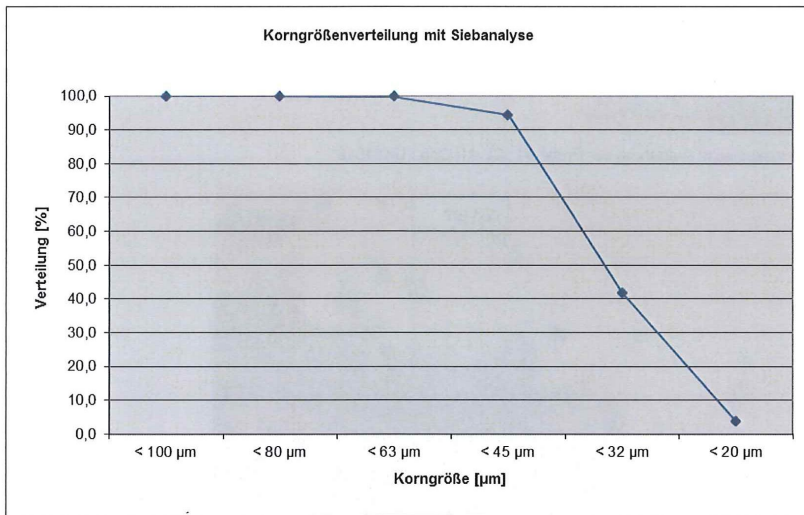
Diagramm 2: Ergebnisse der Siebanalyse der Probe „CL 41, Chg.: UK81646"

3.4. Lichtmikroskopie

Die Pulverproben wurden mittels Lichtmikroskop bei 80-facher Vergrößerung begutachtet (s. Bilder 1 – 4).

Die Proben zeigen rundliche Kornformen und Agglomeratbildung.
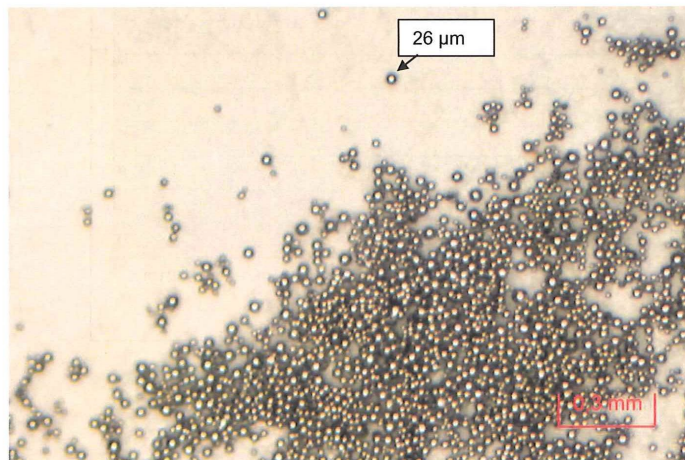
re✓ierlabor

revierlabor GmbH • Westendhof 17 • 45143 Essen • Telefon: (0201) 87421-0 • Telefax: (0201) 87421-19
Eine nur auszugsweise Vervielfältigung des Prüfberichtes ist nur mit schriftlicher Zustimmung von revierlabor gestattet.

Dok. Nr.: 17-02476-a   Seite 4 von 6

86

Bild 1: Lichtmikroskopische Aufnahme der Probe #1 „CL 41, Chg.: UK81646"

Bild 2: Lichtmikroskopische Aufnahme der Probe #1 „CL 41, Chg.: UK81646"

re✔**ierlabor**
revierlabor GmbH • Westendhof 17 • 45143 Essen • Telefon: (0201) 87421-0 • Telefax: (0201) 87421-19
Eine nur auszugsweise Vervielfältigung des Prüfberichtes ist nur mit schriftlicher Zustimmung von revierlabor gestattet.

Dok. Nr.: 17-02476-a   Seite 5 von 6

87
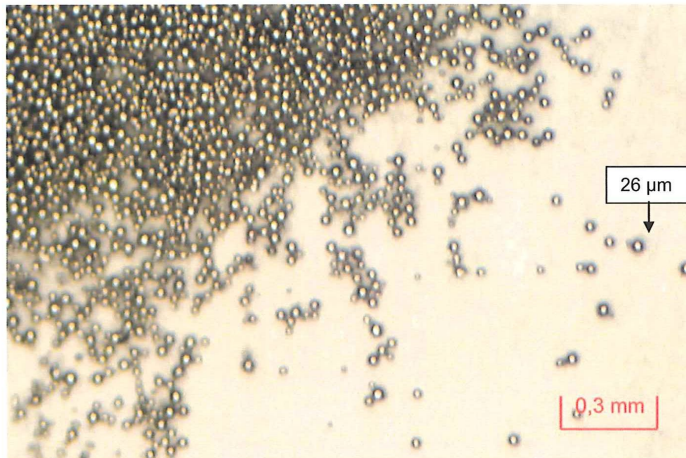
Bild 3: Lichtmikroskopische Aufnahme der Probe #2 „CL 41, Chg.: UK81646"
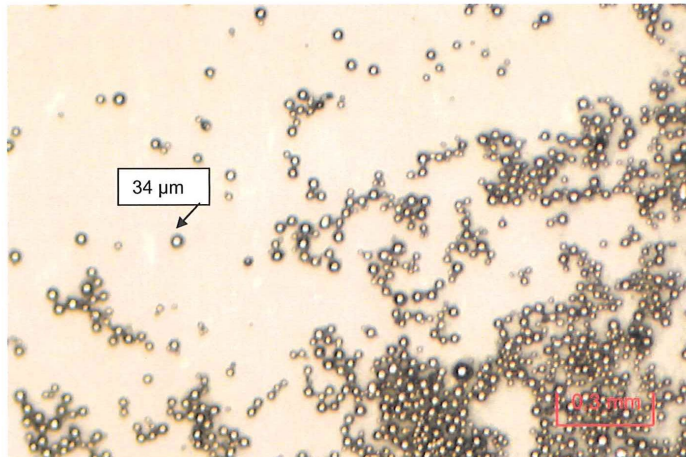
Bild 4: Lichtmikroskopische Aufnahme der Probe #2 „CL 41, Chg.: UK81646"

Essen, 25.07.2017

- N. Trumbach –

Stellv. Abteilungsleiterin Sonderuntersuchungen

Appendix B: Test Report for 316L Stainless Steel Powder provided by Concept Laser

CONCEPTLASER
a GE Additive company

Test Report

Lichtenfels, 18.12.2018

We hereby confirm that the metal powder CL20 ES, batch no. UK83619, has been checked and approved by Concept Laser GmbH in terms of grain size and grain shape and chemical composition as specified below.

As part of this, the metal powder was subjected to analysis applying the relevant quality standards.

In this case the metal powder was subjected to the analysis in accordance with the valid quality standards. The material was analysed and checked by an external and independent testing laboratory for chemical analysis. The laboratory is certified with the test seal of the German Accreditation System.

Results from the following table are according to "1.4404, X 2 CrNiMo 17 13 2 ".

Chem. Element	Target (Min.) in %	Min. in %*	Result in %, Sample 1	Result in %, Sample 2	Max. in %*	Target (Max.) in %
C	0,00	0,023	0,024	0,025	0,026	0,03
Cr	16,5	17,5	17,7	17,7	17,9	18,5
Fe	Rest	Rest	Rest	Rest	Rest	Rest
Mn	0,00	0,89	0,92	0,92	0,95	2,00
Mo	2,00	2,27	2,31	2,31	2,35	2,50
Ni	10,0	12,7	12,8	12,8	12,9	13,0
P	0,00	<0,045	<0,045	<0,045	<0,045	0,045
S	0,00	0,004	0,004	0,005	0,006	0,03
Si	0,00	0,72	0,75	0,79	0,82	1,00

*Measurement uncertainty is included

QM powder

Concept Laser GmbH

sgd. Sven Dilzer
Quality Department

Prüfbericht

Auftragsnummer:	**18-04068**		**Dokumenten-Nr.:**	**18-04068-a**

Auftraggeber:	CONCEPT Laser GmbH An der Zeil 8 DE-96215 Lichtenfels

Bestellnr./Betreff:	114004110

rl-Bearbeiter:	Stefan Frieg	Eingangsdatum: Untersuchungsende:	07.12.2018 18.12.2018

Probennummer: Probenbezeichnung: Material:	18-04068-001 Probe #1, CL 20, Chg.: UK83619 Pulver
Probennummer: Probenbezeichnung: Material:	18-04068-002 Probe #2, CL 20, Chg.: UK83619 Pulver

1 Einleitung und Problemstellung

Gegenstand der Untersuchungen sind die vom Auftraggeber zur Verfügung gestellten Proben mit den o.g. Bezeichnungen. Ziel der Untersuchungen ist die Bestimmung der chemischen Zusammensetzung, die mikroskopische Betrachtung, die Bestimmung der Korngrößenverteilung sowie die Partikelgrößenanalyse der Proben.

2 Durchgeführte Untersuchungen

Die chemische Zusammensetzung der Proben wurde mittels Röntgenfluoreszenzanalyse (RFA) und mittels Verbrennungsanalyse (Kohlenstoff und Schwefel) bestimmt. Des Weiteren wurde eine Bestimmung der Korngrößenverteilung mittels Laserbeugung sowie die Partikelgrößenanalyse mittels Siebanalyse an den Proben durchgeführt. Außerdem wurden die Proben digitalmikroskopisch betrachtet.

Methode	Norm
Röntgenfluoreszenzanalyse (RFA)	Akkreditierte Hausmethode QMA R13A131:2013-10 (RFA-Borat-Aufschluss)
Verbrennungsanalyse (C, S)	Akkreditiertes Verfahren nach ASTM E1019:2011-03
Korngrößenverteilung mittels Laserbeugung[1]	Hausmethode
Siebanalyse	Hausmethode in Anlehnung an ASTM B214:2016
Digitalmikroskopie	Hausmethode

> [1] Die Bestimmung erfolgte durch einen gemäß DIN EN ISO/IEC 17025 akkreditierten Unterauftragnehmer.

3 Ergebnisse

3.1. Werkstoffanalyse

Die Ergebnisse der Werkstoffanalyse sind in den Tabellen 1 und 2 aufgeführt.

revierlabor

revierlabor GmbH • Westendhof 17 • 45143 Essen • Telefon: (0201) 87421-0 • Telefax: (0201) 87421-19

Eine nur auszugsweise Vervielfältigung des Prüfberichtes ist nur mit schriftlicher Zustimmung von revierlabor gestattet.

Dok. Nr.: 18-04068-a   Seite 1 von 9

91

Tabelle 1: Ergebnisse der RFA und Verbrennungsanalyse

Proben-Nr.	18-04068-001
Proben-Bezeichnung	Probe #1, CL 20, Chg.: UK83619

Prüfung	Einheit	Ergebnis
Cr	Mass.-%	17,7
Fe	Mass.-%	Basis
Mn	Mass.-%	0,92
Mo	Mass.-%	2,31
Ni	Mass.-%	12,8
P	Mass.-%	<0,045
Si	Mass.-%	0,75
C	Mass.-%	0,024
S	Mass.-%	0,004

Tabelle 2: Ergebnisse der RFA und Verbrennungsanalyse

Proben-Nr.	18-04068-002
Proben-Bezeichnung	Probe #2, CL 20, Chg.: UK83619

| Prüfung	Einheit	Ergebnis
Cr	Mass.-%	17,7
Fe	Mass.-%	Basis
Mn	Mass.-%	0,92
Mo	Mass.-%	2,31
Ni	Mass.-%	12,8
P	Mass.-%	<0,045
Si	Mass.-%	0,79
C	Mass.-%	0,025
S	Mass.-%	0,005

3.2. Korngrößenverteilung mittels Laserbeugung

Die Korngrößenverteilung der Proben wurde in Doppelbestimmung mittels Laserbeugung ermittelt. Dispergiermedium war Wasser. Die Ergebnisse (Mittelwerte) sind in den folgenden Tabellen 3 und 4 sowie in den Diagrammen 1 und 2 dargestellt.

Tabelle 3: Ergebnisse der Korngrößenverteilung der „Probe #1, CL 20, Chg.: UK83619"

| Proben-Nr.		18-04068-001
Bezeichnung		Probe #1, CL 20, Chg.: UK83619
Prüfung	Einheit	Ergebnis
Dv (10)	µm	18,018
Dv (50)	µm	28,860
Dv (90)	µm	46,297
Breite (90;10)		0,980
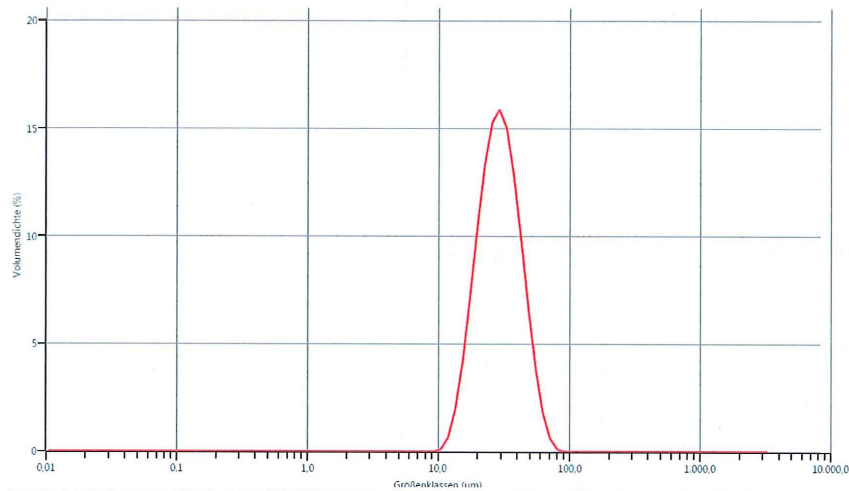
Ergebnis

Größe (µm)	% Volumen Über	Größe (µm)	% Volumen Über	Größe (µm)	% Volumen Über	Größe (µm)	% Volumen Über	Größe (µm)	% Volumen Über
0,010	100,00	0,166	100,00	2,750	100,00	45,613	10,65	756,449	0,00
0,011	100,00	0,188	100,00	3,125	100,00	51,823	5,12	859,450	0,00
0,013	100,00	0,214	100,00	3,550	100,00	58,880	1,95	976,475	0,00
0,015	100,00	0,243	100,00	4,034	100,00	66,897	0,51	1109,435	0,00
0,017	100,00	0,276	100,00	4,583	100,00	76,006	0,06	1260,499	0,00
0,019	100,00	0,314	100,00	5,207	100,00	86,355	0,00	1432,133	0,00
0,022	100,00	0,357	100,00	5,916	100,00	98,114	0,00	1627,136	0,00
0,024	100,00	0,405	100,00	6,722	100,00	111,473	0,00	1848,692	0,00
0,028	100,00	0,460	100,00	7,637	100,00	126,652	0,00	2100,416	0,00
0,032	100,00	0,523	100,00	8,677	100,00	143,897	0,00	2386,415	0,00
0,036	100,00	0,594	100,00	9,858	100,00	163,490	0,00	2711,357	0,00
0,041	100,00	0,675	100,00	11,201	99,94	185,752	0,00	3080,544	0,00
0,046	100,00	0,767	100,00	12,726	99,45	211,044	0,00	3500,000	0,00
0,053	100,00	0,872	100,00	14,458	97,84	239,780	0,00		
0,060	100,00	0,991	100,00	16,427	94,35	272,430	0,00		
0,068	100,00	1,125	100,00	18,664	88,34	309,525	0,00		
0,077	100,00	1,279	100,00	21,205	79,59	351,670	0,00		
0,088	100,00	1,453	100,00	24,092	68,39	399,555	0,00		
0,100	100,00	1,651	100,00	27,373	55,53	453,960	0,00		
0,113	100,00	1,875	100,00	31,100	42,18	515,772	0,00		
0,128	100,00	2,131	100,00	35,335	29,60	586,001	0,00		
0,146	100,00	2,421	100,00	40,146	18,86	665,793	0,00		

Diagramm 1: Ergebnisse der Korngrößenverteilung der „Probe #1, CL 20, Chg.: UK83619"

93

Tabelle 4: Ergebnisse der Korngrößenverteilung der „Probe #2, CL 20, Chg.: UK83619"

Proben-Nr.		18-04068-002
Bezeichnung		Probe #2, CL 20, Chg.: UK83619
Prüfung	Einheit	Ergebnis
Dv (10)	µm	18,593
Dv (50)	µm	28,764
Dv (90)	µm	44,668
Breite (90;10)		0,907
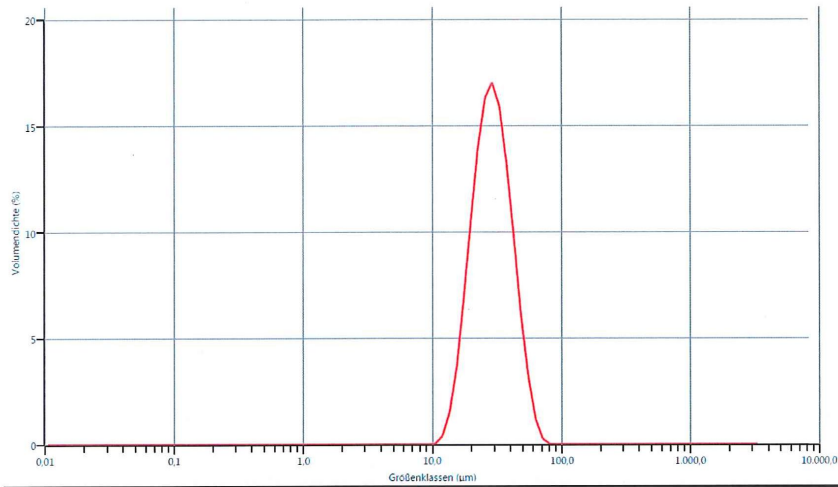
Größe (µm)	% Volumen Über	Größe (µm)	% Volumen Über	Größe (µm)	% Volumen Über	Größe (µm)	% Volumen Über	Größe (µm)	% Volumen Über
0,010	100,00	0,166	100,00	2,750	100,00	45,613	8,67	756,449	0,00
0,011	100,00	0,188	100,00	3,125	100,00	51,823	3,64	859,450	0,00
0,013	100,00	0,214	100,00	3,550	100,00	58,880	1,10	976,475	0,00
0,015	100,00	0,243	100,00	4,034	100,00	66,897	0,18	1109,435	0,00
0,017	100,00	0,276	100,00	4,583	100,00	76,006	0,00	1260,499	0,00
0,019	100,00	0,314	100,00	5,207	100,00	86,355	0,00	1432,133	0,00
0,022	100,00	0,357	100,00	5,916	100,00	98,114	0,00	1627,136	0,00
0,024	100,00	0,405	100,00	6,722	100,00	111,473	0,00	1848,692	0,00
0,028	100,00	0,460	100,00	7,637	100,00	126,652	0,00	2100,416	0,00
0,032	100,00	0,523	100,00	8,677	100,00	143,897	0,00	2386,415	0,00
0,036	100,00	0,594	100,00	9,858	100,00	163,490	0,00	2711,357	0,00
0,041	100,00	0,675	100,00	11,201	99,99	185,752	0,00	3080,544	0,00
0,046	100,00	0,767	100,00	12,726	99,72	211,044	0,00	3500,000	0,00
0,053	100,00	0,872	100,00	14,458	98,53	239,780	0,00		
0,060	100,00	0,991	100,00	16,427	95,52	272,430	0,00		
0,068	100,00	1,125	100,00	18,664	89,83	309,525	0,00		
0,077	100,00	1,279	100,00	21,205	81,02	351,670	0,00		
0,088	100,00	1,453	100,00	24,092	69,30	399,555	0,00		
0,100	100,00	1,651	100,00	27,373	55,56	453,960	0,00		
0,113	100,00	1,875	100,00	31,100	41,23	515,772	0,00		
0,128	100,00	2,131	100,00	35,335	27,86	586,001	0,00		
0,146	100,00	2,421	100,00	40,146	16,76	665,793	0,00		

Diagramm 2: Ergebnisse der Korngrößenverteilung der „Probe #2, CL 20, Chg.: UK83619"

3.3. Siebanalyse

Die Proben wurden über 100 µm-, 80 µm-, 63 µm-, 45 µm-, 32 µm- und 20 µm Siebe gesiebt.

Die Ergebnisse sind in den Tabellen 5 und 6 sowie in den Diagrammen 3 und 4 dargestellt.

Tabelle 5: Ergebnisse der Siebanalyse der „Probe #1, CL 20, Chg.: UK83619"

Proben-Nr.		18-04068-001
Bezeichnung		Probe #1, CL 20, Chg.: UK83619
Korngröße	Einheit	Ergebnis
< 100 µm	%	100,0
< 80 µm	%	100,0
< 63 µm	%	99,95
< 45 µm	%	99,00
< 32 µm	%	79,46
< 20 µm	%	31,55
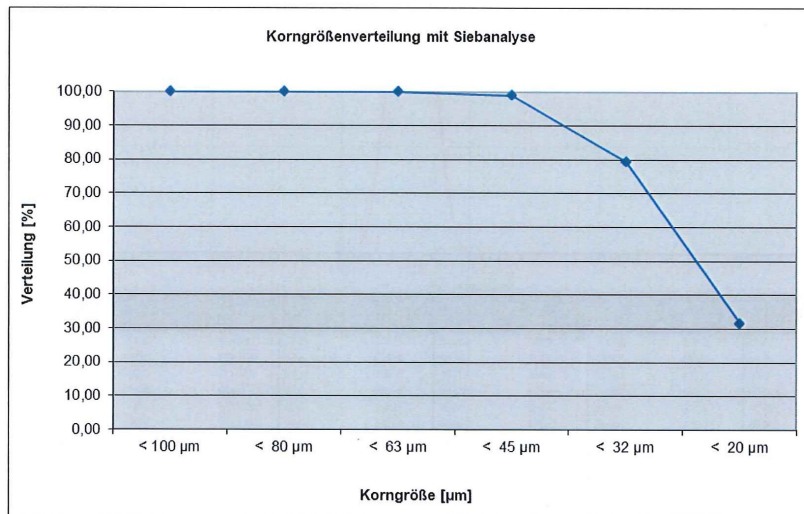
Diagramm 3: Ergebnisse der Siebanalyse der „Probe #1, CL 20, Chg.: UK83619"

revierlabor
revierlabor GmbH • Westendhof 17 • 45143 Essen • Telefon: (0201) 87421-0 • Telefax: (0201) 87421-19
Eine nur auszugsweise Vervielfältigung des Prüfberichtes ist nur mit schriftlicher Zustimmung von revierlabor gestattet.

Dok. Nr.: 18-04068-a   Seite 5 von 9

95

Tabelle 6: Ergebnisse der Siebanalyse der „Probe #2, CL 20, Chg.: UK83619"

| Proben-Nr.		18-04068-002
Bezeichnung		Probe #2, CL 20, Chg.: UK83619
Korngröße	Einheit	Ergebnis
< 100 µm	%	100,0
< 80 µm	%	100,0
< 63 µm	%	99,95
< 45 µm	%	98,82
< 32 µm	%	80,18
< 20 µm	%	33,22

Korngrößenverteilung mit Siebanalyse
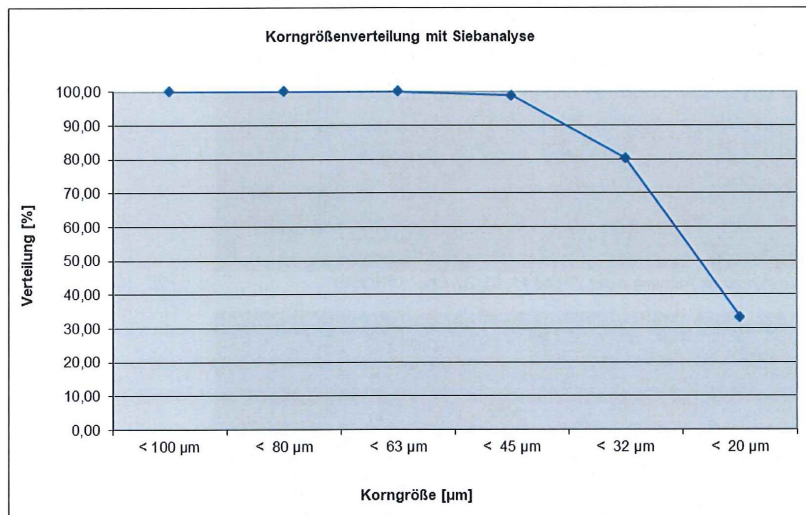
Diagramm 4: Ergebnisse der Siebanalyse der „Probe #2, CL 20, Chg.: UK83619"

3.4. Lichtmikroskopie

Die Pulverproben wurden mittels Digitalmikroskop bei 100-facher Vergrößerung begutachtet (s. Bilder 1 – 4).
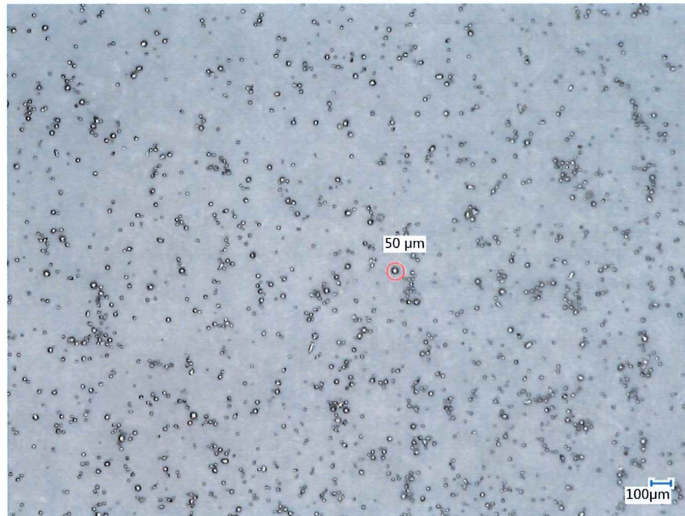
Bild 1: Lichtmikroskopische Aufnahme der „Probe #1, CL 20, Chg.: UK83619"
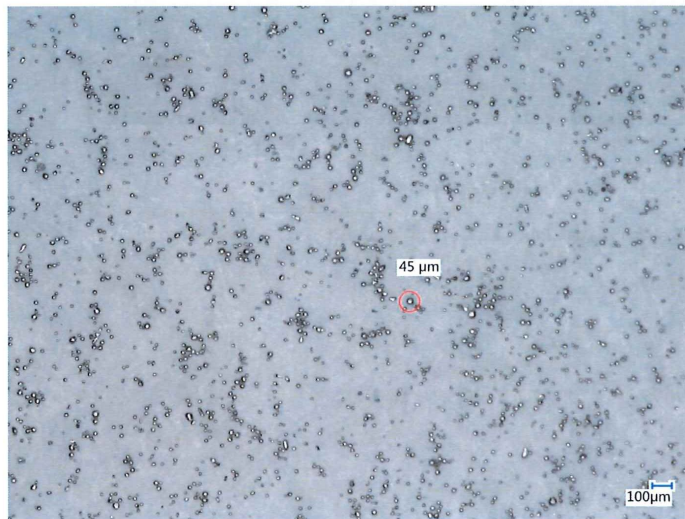
Bild 2: Lichtmikroskopische Aufnahme der „Probe #1, CL 20, Chg.: UK83619"

re✓**ierlabor**

revierlabor GmbH • Westendhof 17 • 45143 Essen • Telefon: (0201) 87421-0 • Telefax: (0201) 87421-19
Eine nur auszugsweise Vervielfältigung des Prüfberichtes ist nur mit schriftlicher Zustimmung von revierlabor gestattet.

Dok. Nr.: 18-04068-a   Seite 7 von 9

97

Bild 3: Lichtmikroskopische Aufnahme der „Probe #2, CL 20, Chg.: UK83619"
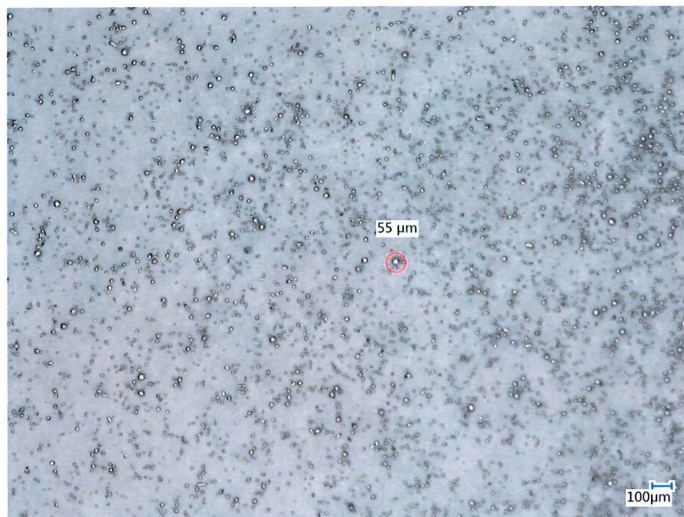
Bild 4: Lichtmikroskopische Aufnahme der „Probe #2, CL 20, Chg.: UK83619"

Essen, 18.12.2018

Trumbach

- N. Trumbach –

Stellv. Abteilungsleiterin Sonderuntersuchungen/Schadensfälle

ilac-MRA ((DAkkS
Deutsche
Akkreditierungsstelle
D-PL-18336-01-00

re✓**ierlabor**
revierlabor GmbH • Westendhof 17 • 45143 Essen • Telefon: (0201) 87421-0 • Telefax: (0201) 87421-19
Eine nur auszugsweise Vervielfältigung des Prüfberichtes ist nur mit schriftlicher Zustimmung von revierlabor gestattet.

Dok. Nr.: 18-04068-a   Seite 9 von 9

99